AEDC TR-94-6

Hypersonic Wind Tunnel Test Techniques

R. K. Matthews and R. W. Rhudy
Calspan Corporation/AEDC Operations

August 1994

Final Report for Period July 1992 — May 1993

ARNOLD ENGINEERING DEVELOPMENT CENTER
ARNOLD AIR FORCE BASE, TENNESSEE
AIR FORCE MATERIEL COMMAND
UNITED STATES AIR FORCE

NOTICES

When U. S. Government drawings, specifications, or other data are used for any purpose other than a definitely related Government procurement operation, the Government thereby incurs no responsibility nor any obligation whatsoever, and the fact that the Government may have formulated, furnished, or in any way supplied the said drawings, specifications, or other data, is not to be regarded by implication or otherwise, or in any manner licensing the holder or any other person or corporation, or conveying any rights or permission to manufacture, use, or sell any patented invention that may in any way be related thereto.

Qualified users may obtain copies of this report from the Defense Technical Information Center.

References to named commercial products in this report are not to be considered in any sense as an endorsement of the product by the United States Air Force or the Government.

This report has been reviewed by the Office of Public Affairs (PA) and is releasable to the National Technical Information Service (NTIS). At NTIS, it will be available to the general public, including foreign nations.

APPROVAL STATEMENT

This report has been reviewed and approved.

Dennis N Huprich

DENNIS N. HUPRICH, Major, USAF
Space and Missile Systems Test Division

Approved for publication:

FOR THE COMMANDER

Conrad M Ritchey

CONRAD M. RITCHEY, Lt Col, USAF
Space and Missile Systems Test Division

REPORT DOCUMENTATION PAGE

Form Approved
OMB No. 0704-0188

1 AGENCY USE ONLY (Leave blank)	2. REPORT DATE	3. REPORT TYPE AND DATES COVERED
	August 1994	Final -- July 1992 - May 1993

4. TITLE AND SUBTITLE
Hypersonic Wind Tunnel Test Techniques

5 FUNDING NUMBERS
JN - 0979

6 AUTHOR(S)
Matthews, R. K. and Rhudy, R. W., Calspan Corporation/AEDC Operations

7 PERFORMING ORGANIZATION NAME(S) AND ADDRESS(ES)
Arnold Engineering Development Center/DOF
Air Force Materiel Command
Arnold Air Force Base, TN 37389-4000

8. PERFORMING ORGANIZATION REPORT NUMBER
AEDC-TR-94-6

9 SPONSORING/MONITORING AGENCY NAMES(S) AND ADDRESS(ES)
Arnold Engineering Development Center/DOF
Air Force Materiel Command
Arnold Air Force Base, TN 37389-4000

10 SPONSORING/MONITORING AGENCY REPORT NUMBER

11 SUPPLEMENTARY NOTES
Available in Defense Technical Information Center (DTIC).

12a DISTRIBUTION/AVAILABILITY STATEMENT
Approved for public release; distribution is unlimited.

12b DISTRIBUTION CODE

13. ABSTRACT (Maximum 200 words)

This report describes the procedures used in the continuous flow hypersonic tunnels of the AEDC for static stability, pressure, heat transfer, materials/structures, boundary-layer transition, and electromagnetic wave testing. Particular emphasis is placed on heat-transfer techniques because of the importance of defining the thermal environment of hypersonic vehicles. An overview of the materials/structures test methodology used in the development of hypersonic vehicle components is presented. Unfortunately, the methodology to predict transition has eluded the aerodynamicist for over three decades, and there are still many unanswered questions. This report briefly touches on the many parameters that affect transition and provides numerous references for those who are interested in specializing in this topic. The methodology of using trip spheres is discussed, and illustrative data are presented. Electromagnetic wave testing represents a relatively new test technique that involves the union of several disciplines: aerothermodynamics, electromagnetics, materials/structures, and advanced diagnostics. The essence of this new technique deals with the transmission and possible distortion of electromagnetic waves (RF or IR) as they pass through the bow shock, flow field, and electromagnetic (EM) window of a missile flying at hypersonic speeds.

14. SUBJECT TERMS	15. NUMBER OF PAGES
electromagnetic waves, missile seeker system, hypersonic vehicles, boundary layer, boresight error, radomes	59
	16. PRICE CODE

17. SECURITY CLASSIFICATION OF REPORT	18. SECURITY CLASSIFICATION OF THIS PAGE	19. SECURITY CLASSIFICATION OF ABSTRACT	20. LIMITATION OF ABSTRACT
UNCLASSIFIED	UNCLASSIFIED	UNCLASSIFIED	SAME AS REPORT

FOREWORD

The hypersonic regime is the most severe of all flight regimes, and consequently demands smart utilization of ground testing and evaluation, flight testing, and computation/simulation methodologies. Because of this challenge, von Karman Institute (VKI) asked the Arnold Engineering Development Center (AEDC) to develop a comprehensive course to define the "Methodology of Hypersonic Testing." Seven American scientists and engineers, representing AEDC and the University of Tennessee Space Institute (UTSI), formulated this course from their background of over a century of combined experience in hypersonic testing.

The objective of the course was to present a comprehensive overview of the methods used in hypersonic testing and evaluation, and to explain the principles behind those test techniques. Topics covered include an introduction to hypersonic aerodynamics with descriptions of chemical and gas-dynamic phenomena associated with hypersonic flight; categories and application of various hypersonic ground test facilities; characterization of facility flow fields; measurement techniques (both intrusive and non-intrusive); hypersonic propulsion test principles and facilities; computational techniques and their integration into test programs; ground-test-to-flight data correlation methods; and test program planning. The Lecture Series begins at the introductory level and progressively increases in depth, culminating in a focus on special test and evaluation issues in hypersonics such as boundary-layer transition, shock interactions, electromagnetic wave testing, and propulsion integration test techniques.

To obtain a complete set of notes from this course write to:

Lecture Series Secretary
von Karman Institute
Charrissie de Waterloo, 72
B-16409 Rhode-Saint-Genese (Belgium)

The information contained in this report is a subset of the work described above.

CONTENTS

TEST AND EVALUATION METHODS

by
R. K. MATTHEWS and R. W. RHUDY
Senior Staff Engineers
Calspan Corporation/AEDC Operations
Arnold Engineering Development Center

ABSTRACT

Test facility selection is generally the first step toward planning a wind tunnel test, either through availability, simulation, or test technique requirements. The operating characteristics of the chosen facility will immediately restrict the choice of test techniques because of the tunnel operating mode. Since the time response of the measurement technique must be compatible with the run time of the facility, some techniques are immediately ruled out for certain facilities. The aerodynamic and aerothermal test techniques used in conventional hypersonic tunnels are generally similar throughout the world, varying only in the sophistication of the facilitys' instrumentation and data acquisition systems. This section describes the procedures used in the continuous flow hypersonic tunnels of the AEDC for static stability, pressure, and heat transfer testing. Particular emphasis will be on heat transfer techniques because of the importance of defining the thermal environment of hypersonic vehicles and because the static stability and pressure techniques are very similar to those used in subsonic and supersonic facilities.

NOMENCLATURE

A_o	Intercept of $\dot{q}$ versus T_W for heat gage data
A_1	Slope of $\dot{q}$ versus T_W for heat gage data
b	Thin-skin wall thickness
c	Specific heat
C_x	Static stability coefficients: e.g. lift C_L, drag C_D, pitching moment C_m
C_P	Pressure coefficient
CSF	Heat gage calibration factor
$C(t_n)$	Coax gage calibration factor calculated at time t_n
E	Heat gage output, mv
F_A	Axial force
F_N	Normal force
F_Y	Side Force
h	Heat-transfer coefficient
k	Material conductivity
M	Mach number
$M_{1, 2, or x}$	Balance moment
p	Pressure
q	Dynamics pressure
$\dot{q}$	Heat flux
Re	Reynolds number
t	Time
T	Temperature
S	Reference area
S/R	Surface distance-to-nose radius ratio
W	Model weight
$\bar{x}, \bar{y}, \bar{z}$	Coordinates of model CG in balance axis system
α	Angle of attack
β	Angle of sideslip
ϱ	Density
ΔT	Temperature difference
ϕ	Roll angle

Subscripts

F	Flight
i	Initial (time = 0)
L	Model length
pc	Phase change

T	Tunnel
r	Recovery
w	Wall
∞	Free stream
o	Stilling chamber conditions

INTRODUCTION

One of the primary considerations in evaluating hypersonic facilities is the test techniques (or test methods) available in a given facility. A thorough understanding of test techniques is very important in planning a test program to address a precisely defined test objective. This section describes the aerodynamic and aerothermal test techniques that are in general use. The aerodynamic methodology includes force balance measurements and surface pressure measurements. Flow-field and other aerodynamic techniques are discussed in later sections. Aerothermal methodology includes thermal mapping, discrete gage techniques and gage calibration. In general, each specific test technique is described in terms of (a) principle of operation, (b) apparatus, (c) data reduction and d) illustrative data.

STATIC STABILITY TESTING

Static stability tests in a hypersonic wind tunnel are conducted in much the same manner and for the same reasons as in lower-speed wind tunnels. Typical tests are conducted to; verify that the performance of a particular design is accurate (parametric studies); verify theoretical codes (CFD); and/or prove that proposed modifications to existing flight hardware will, in fact, improve the performance. In general, compared to low speed facilities the tunnels and the test models are smaller and the test environment much more severe. These smaller models and the extreme environment (i.e., low static pressure and extremely high total pressure and temperature lead to special requirements not encountered in lower speed wind tunnels. It is much cheaper and safer to build small-scale vehicles and test in the wind tunnel ("Test before flight") than to build the real thing and have it fail ("Build it and see if it works"). The classical wind tunnel to flight correlation parameters are shown in Fig. 1. Once the need for a static stability wind tunnel test is determined and the test objectives clearly established, the choice of what facility to use can be made. This choice naturally will dictate many of the pretest requirements/activities, such as model scale, test techniques, etc. The following sections cover the relatively standard static stability test model, as shown in Fig. 2.

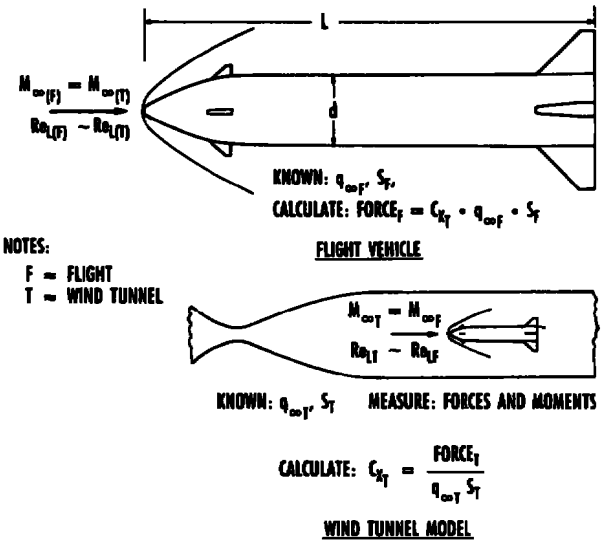

Figure 1. Wind tunnel/flight simulation.

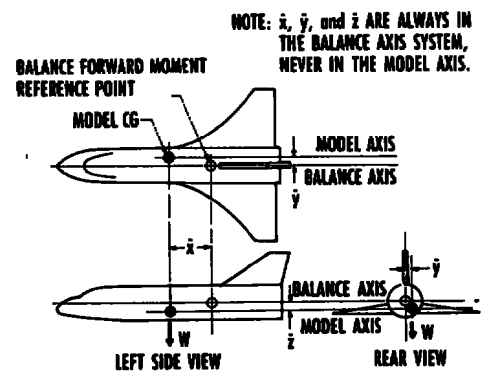

Figure 2. Model weight (tare) and center-of-gravity locations referenced to balance axis.

The procedures described are for tests in conventional, relatively long duration wind tunnels. Impulse type, short-duration testing requires other special procedures to compensate for such things as the inertia forces from model vibrations.[1]

Apparatus

In general, static stability data in a hypersonic wind tunnel are obtained by use of a strain gage balance, usually mounted internal to the test model. Special circumstances may dictate deviations such as

extremely small models which require that the balance be mounted external to the model with the use of a windshield, but these are so diverse that they need to be addressed on a case-by-case basis and will not be covered here. Also, at times, requirements arise for force/moment measurements to be made on control surfaces or other individual parts of a vehicle; however, the techniques used and fabrication/calibration requirements are nearly identical to those described below for the "main" balance.

Strain gage balances are constructed by machining a thin section (called a flexure) in the balance and bonding a strain gage to the surface. As loads are applied, either by calibration or through the test article, the elongation/compression of the flexure and thereby the strain gage causes an electromotive force (EMF) to be produced by the gage. This EMF can then be amplified and electronically processed in conjunction with the balance calibration to calculate the applied load. Machining several flexures into a single balance at the proper locations and in the proper plane with respect to the balance centerline creates the capability to resolve all six components, i.e., normal, side and axial force and pitching, yawing, and rolling moments. The flexures and gages can be arranged to measure two moments which are then resolved into a force and a moment (e.g. F_N and M_X) or two forces which can be summed to obtain the total force and, by using the balance geometry, resolved to a moment. These two types of balances and their measurement resolutions are illustrated in Fig. 3. The hypersonic wind tunnels at AEDC normally use moment-type balances. A schematic showing the normal arrangement of the flexures and gages for this type balance is given in Fig. 4. As stated earlier, speciality balances measure from 1 to 6 components either force-type or moment-type or a combination; however, the principle of operation, i.e., flexures and strain gages, is the same. Balances are designed and fabricated for specific maximum loads. Obviously, the load range of a particular balance is determined by the size of the flexures and the overall strength of the balance.

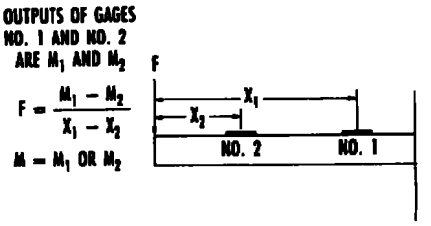

a. Moment balance

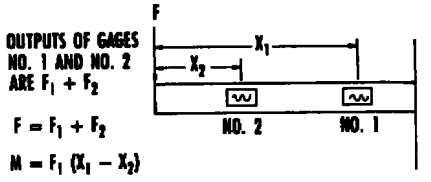

b. Force balance

Figure 3. Force type and moment type balances.

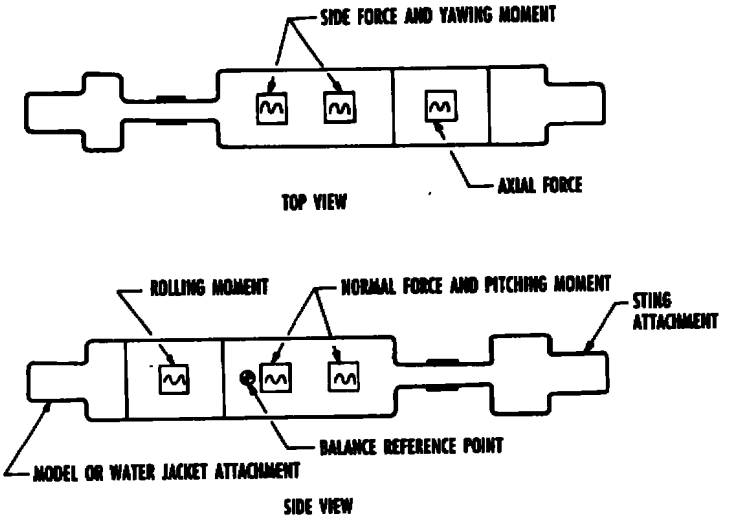

Figure 4. Moment type internal balance.

Balance Calibration

Once a balance has been designed and fabricated, it must be calibrated to determine the electrical output (EMF) from the strain gages for a given applied load. There are probably as many different techniques of calibrating a balance as there are test facilities. For these notes, the procedures used to calibrate the balances used in the AEDC hypersonic tunnels will be covered. Other techniques are very similar, and the end result differs only by the desired precision of the test data.

Balances are designed so that the flexures are aligned to measure a single component, i.e., strictly F_N, F_A or F_Y. However, it is impossible to machine the balance and install the strain gages so that they are perfectly aligned. Therefore, because of this misalignment a pure normal force will produce some output from the side force and other gages; conversely a pure side force will produce some output from the normal force and other gages; etc. These secondary outputs are called interactions, and must be accounted for with the calibration.

The calibration of a balance consists of applying loads and combinations of loads (i.e., pure F_N, $F_N + F_A$, $F_N + F_Y$, etc.) in increments up to the rated capacity of the balance and at several locations along the entire length of the balance. The electrical outputs from the strain gages are measured, amplified, and loaded into a very complex computer program. This program takes into account such things, in addition to the applied load and its location, as the weight of the calibration equipment, balance deflections, balance roll angle, etc. After the entire set of calibration loads has been applied, the program calculates the balance constants to be used to resolve the forces and moments sensed by the balance during a wind tunnel test. These constants, along with the other information shown in Fig. 5 are loaded into the test data reduction computer. A balance calibration is quite complicated and time consuming, typically requiring 4 to 5 days; however, a single calibration will normally be used for several tests. As a check, however, prior to each test a simplified version of the calibration loading is applied to the balance. The measured balance outputs are reduced to forces and moments using the previously calculated balance constants in a "Balance Loading Program" (BLP) and compared to the known applied loads. Since the maximum applied loads are chosen equal to the expected maximums during the test, this comparison gives an insight into the test data precision. If the comparison of applied loads to calculated loads is outside established precision bounds for the particular balance, the balance is recalibrated.

As shown in Fig. 6, a large number of balances are available for use in the AEDC hypersonic wind tunnels. These balances vary in design and cover a wide range of load-carrying capabilities. For the highest quality data, a balance should be selected that has maximum rated load capability close to the maximum expected test loads. Also shown at the top of Fig. 6 is the water jacket which covers the balances when used in the hypersonic wind tunnels. Since the output of the balance is highly temperature sensitive, it must be kept cool (near room temperature) during data taking. This can be accomplished by either getting the data very quickly or by use of the water jacket which shields the balance from both radiative and conductive heating.

Model Fabrication

The choice of the facility to be used to satisfy the test objective will dictate the size of the model that can be tested. The model scale must be large enough to maintain the fidelity of the full-scale configura-

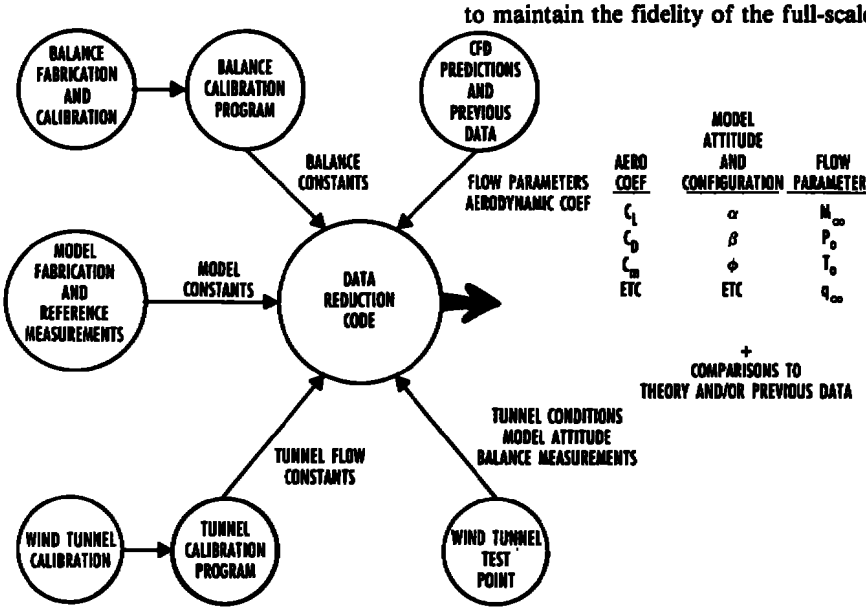

Figure 5. Static stability test overview.

* GENERAL PURPOSE 6-COMPONENT BALANCES (24 AVAILABLE)
  - NOMINAL BALANCE SIZES: LENGTH, IN. 5.1 TO 13.8 (13-35 cm) DIAMETER, IN. 0.6 TO 2.1 (15-53 cm)
  - NORMAL FORCE RANGES, LB: 20 TO 1,500
  - SIDE FORCE RANGES, LB: 20 TO 700
  - AXIAL FORCE RANGES, LB: 4 to 300
* SPECIAL PURPOSE BALANCES (12 AVAILABLE)
  - TYPES AVAILABLE: * MASS ADDITION (3 TO 6 COMPONENT) * MAGNUS FORCE AND MOMENTS

Figure 6. AEDC tunnels A/B/C balances.

tion; otherwise, the wind tunnel data will not accurately predict the flight performance of the vehicle. Model weight must be kept low so that it is only a small percentage of the balance full-scale capability. However, because of the high-temperature environment, models for hypersonic force testing are usually fabricated from stainless steel. After the model is completed, the reference areas, lengths, weight, and c.g. location must be accurately measured for input to the data reduction program. These model dimensions and weights must be obtained for every configuration to be tested. The test data precision/imprecision is a direct function of how accurately these measurements are obtained and how they replicate the full-scale vehicle contours. The model is then assembled with the balance, water jacket, and balance sting, and the relative location of the model c.g. with respect to the balance center is determined (see Fig. 7). It is now ready to be installed in the wind tunnel.

Testing Methods

Wind tunnel force data are generally obtained in one of two methods, either point-pause or continuous sweep. Each of these methods has it advantages and disadvantages. In the point-pause method, data are obtained by positioning the model at a discrete angle of attack and angle of sideslip, usually waiting for the base pressure to stabilize, and recording the measurements electronically into the data reduction computer. This is repeated for each model attitude desired, usually in 2- or 3-deg increments over the entire range of angle of attack and/or 5-deg increments over the sideslip range. The advantages and disadvantages of this technique, are shown in Fig. 8.

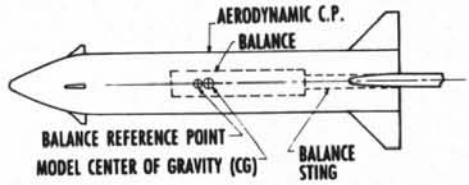

- STAINLESS STEEL MODEL - AS LIGHT AS POSSIBLE
- IDEALLY MODEL C. G. IN CENTER OF BALANCE (BETWEEN GAGES)
- BALANCE ALSO LOCATED AS CLOSE AS POSSIBLE TO THE AERODYNAMIC CENTER OF PRESSURE
- DATA PRECISION DEPENDENT ON ACCURATE MEASUREMENTS OF:
  - REFERENCE AREAS
  - REFERENCE LENGTHS
  - C.G. LOCATION WITH RESPECT TO BALANCE
  - MODEL COMPONENT WEIGHTS

Figure 7. Model-balance arrangement.

ADVANTAGES	DISADVANTAGES
1. GREATER DATA PRECISION	1. MUCH SLOWER THAN CONTINUOUS SWEEP—MORE COSTLY
2. BASE PRESSURE MEASUREMENTS AT EVERY MODEL ATTITUDE	2. ONLY ONE DATA POINT PER RUN IN IMPULSE TUNNEL
3. LESS LIKELY TO HAVE ABNORMAL HYSTERISIS EFFECTS	3. MODEL DISTORTION DUE TO NON-UNIFORM HEATING
4. USE PITCH AND ROLL MECHANISM TO SET PREDETERMINED α AND β	4. DATA NOT NECESSARILY AT SAME MODEL ALTITUDE FOR EACH CONFIGURATION
5. SIMPLE DATA REDUCTION	

Figure 8. Point-pause data taking technique.

In the continuous sweep method, high-speed data are taken as the model is pitched, rolled, or yawed through an angle range. Angle change rates vary from a few degrees a second to tens-of-degrees per second. The continuous data are "curve-fit" by a computer routine, and finite data points are tabulated at the desired angles. The data reduction program takes into account the same items as in the point-pause method, i.e., balance/sting deflections, model weight, etc. The advantages and disadvantages of the continuous sweep data method are shown in Fig. 9.

During both the point-pause and the continuous sweep tests, data are usually repeated for a pitch

ADVANTAGES	DISADVANTAGES
1. LESS TUNNEL TIME/COST	1. LESS ACCURATE DATA
2 OBTAIN ENTIRE PITCH RANGE DURING ONE RUN IN IMPULSE TUNNEL	2. BASE PRESSURE MEASUREMENTS AT START AND END ONLY
3. DATA TABULATED AT SAME MODEL ATTITUDE	3. MORE LIKELY TO ENCOUNTER ABNORMAL HYSTERISIS EFFECTS
4 MUCH LESS MODEL DISTORTION DUE TO DIFFERENTIAL HEATING	4. DATA REDUCTION REQUIRES MORE COMPUTER STORAGE AND TIME

Figure 9. Continuous sweep data taking technique.

series, but with the model rolled 180 deg. By comparing these data to the zero roll data, an evaluation of the effects of nonuniform (M_∞ variations, flow angularity, etc.) tunnel flow can be made and corrections programmed into the data reduction. Great care must be taken to interpret these data correctly and to not make erroneous adjustments to the data.

Additional Test Methods

The preceding section addressed the standard six-component force tests with base pressures. Very often, additional measurements (Fig. 10) are required in order to fulfill the test objective. Quite often, vehicles have control surfaces for which the loads at various deflections are required in order to ensure the structural integrity of the component, its attachment, and the control system. These loads are measured with a small balance ("fin balance"), usually three components, mounted internally to the model. Great care must be taken during wind tunnel installation of these models to ensure that the electrical leads to the fin balances, which must "jumper" the main balance, do not restrict the main balance deflections and therefore cause erroneous readings. These balances are fabricated and instrumented very similar to the main balance and require the same type calibration and data reduction. They normally measure a normal force, hinge moment, and the root bending moment.

Another fairly common and yet non-standard model for hypersonic wind tunnel test requires the simulation of engines which require ram air. To truly simulate the flight vehicle, the wind tunnel model must be built with a "flow through" duct. The internal part of these "engine simulators" cannot be fabricated to truly reproduce the drag/thrust of the full-scale vehicle; therefore, corrections to the measured wind tunnel drag must be made. The data for these corrections is provided by one of several means, depending on the desired precision. The highest quality final drag data require measurements which will allow calculations of the mass flow through the duct over the full range of test conditions and pressure measurements from which velocity can be calculated. These measurements can be obtained by separate test runs using mass meters and a set of well-designed pressure probes, or during the standard point-pause force test runs using pressure probes and several simplifying assumptions.

- FIN/CONTROL SURFACE BALANCES
  - USUALLY MEASURE A FORCE AND TWO MOMENTS (NORMAL FORCE, HINGE MOMENT AND ROOT BENDING MOMENT)
  - CALIBRATION AND DATA REDUCTION VERY SIMILAR TO STANDARD BALANCE
  - WHEN USED WITH MAIN BALANCE-CARE MUST BE EXERCIZED TO INSURE THAT FIN BALANCE LEADS DO NOT INTERFERE WITH MAIN BALANCE OUTPUT
- FLOW-THROUGH DUCT/ENGINE SIMULATORS
  - TOTAL AXIAL-FORCE MUST BE ADJUSTED FOR DUCT DRAG
  - DUCT DRAG CALCULATED BY MEASURING MASS FLOW AND VELOCITY–MOMENTUM DEFECT
- CAPTIVE TRAJECTORY SYSTEM (CTS)
  - USED FOR STORE SEPARATION TESTS
  - GRID MODE/TRAJECTORY MODE

Figure 10. Special test requirements.

The AEDC Captive Trajectory System (CTS) is shown in Fig. 11. CTS tests usually have a parent vehicle mounted on a six-component balance supported on the tunnel standard pitch mechanism and an additional model of an "external store," (missile or bomb) mounted on a balance connected to the CTS. The CTS is a mechanism which can produce six degrees of freedom independent of the main model support. The attitude and position of the CTS model relative to the parent vehicle can either be preprogrammed points in the CTS computer (grid mode) or determined by the forces and moments sensed by the CTS balance (trajectory mode). This is a highly complex type test and requires a large amount of pretest set-up. However, once it is operational, a large amount of data can be obtained in a relatively short amount of wind tunnel time. The AEDC/CTS is the only such system known in the world to operate at hypersonic speeds. The space shuttle solid rocket booster separation was tested at M = 4 in Tunnel A, and separation of the external tank (E/T) from the orbiter was tested in Tunnel B at Mach 8.

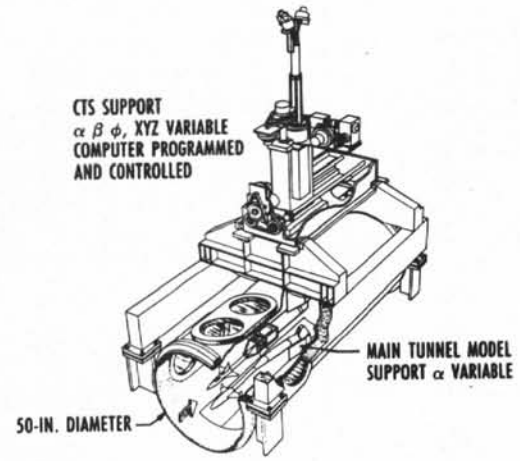

a. Tunnel B installation sketch

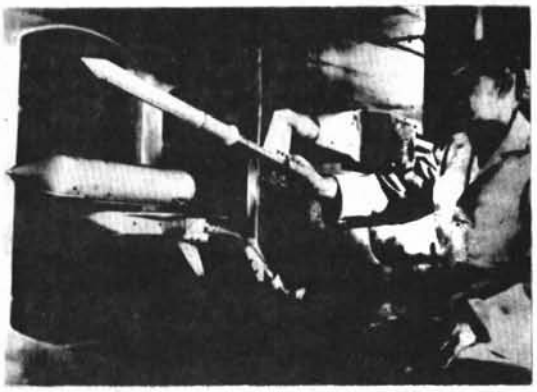

b. Test of shuttle booster rocket separation in tunnel A.

Figure 11. AEDC captive trajectory system.

Data Reduction

The data reduction program for point-pause type data is quite complicated, and yet much simpler than that for the continuous sweep type. At each desired model attitude (data point), the electrical outputs from the balance, model attitude sensors, base pressure transducers, wind tunnel pressure and temperature instrumentation, and other inputs are amplified, converted to digital form, and fed to the data reduction computer. These data are combined with the previously input balance calibration and wind tunnel calibration data. The tunnel calibration data are used to calculate the test conditions. Model positioning readouts, are combined with the force/moment data from the balance to calculate the aerodynamic coefficients and model attitude. These data can then be used to resolve the coefficients into any axis system (body, wind, pitch, etc.) desired. Total drag is made up of skin friction, base drag, and wave drag. Since the skin friction is generally a small part of the total drag, no adjustments are made for any difference between the wind tunnel value and flight value. This is not, however, the case with base axial force. Because of sting effects in the wind tunnel, the base pressure may be very different from the flight value. Therefore, an adjustment to the axial force measured by the balance $(C_{A_T})_T$ is made. As noted in Fig. 12, the wind tunnel base axial force $(C_{A_B})_T$, as calculated from the measured base pressure is subtracted from the $(C_{A_T})_T$ to obtain the forebody axial force (C_{A_F}) which is the same for both wind tunnel and flight. The flight total axial force $(C_{A_T})_F$ is then derived by adding a predicted flight base drag $(C_{A_B})_F$ to the C_{A_F}. Other adjustments may be applied to the data to compensate for such things as wind tunnel flow angularity, model/balance misalignments, etc. In the special case of a model which has a simulated engine duct, an adjustment to the drag data, similar to the base drag adjustment, must also be made. There are several methods used to calculate the internal drag of the wind tunnel duct with varying degrees of accuracy. The most precise method is to measure the mass flow through the duct using a pre-calibrated mass flow-meter in addition to measurements (total and static pressures) from which velocity can be calculated, and then to adjust the total axial force by the momentum loss of the flow through the duct.

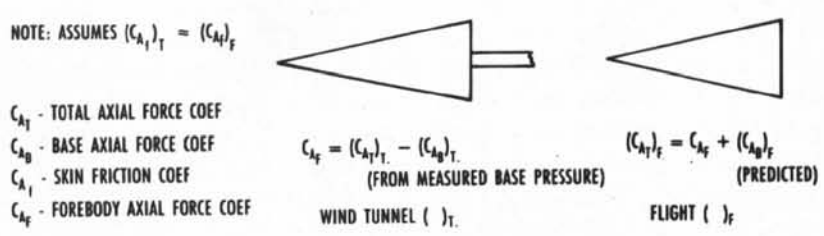

Figure 12. Axial force accounting.

The data reduction program for continuous sweep data is the same as for point-pause, except for the manner in which the data points to be tabulated are generated. As explained earlier, instead of data at finite model pitch/yaw positions, a continuous stream of data is generated over a pitch,

yaw, or roll sweep. These data are then fit with a computer-generated polynomial for each variable, and then the finite data points are generated at the desired model attitudes. These finite points are then operated on by the computer in the same way as for the point-pause data. If adjustments are to be made for base pressure, internal drag, or other items which require pressure measurement, separate test runs must be made in the point-pause mode to allow time for the pressure instrumentation to respond accurately. These data can also be curve fit and fed into the same adjustment routines as in the point-pause mode.

In addition to the calculations, adjustments, and/or corrections discussed above, the data reduction computer is quite often preprogrammed with theoretical predictions (CFD) and/or previously measured values of the wind tunnel model aerodynamic performance. Comparisons of these values to the measured values provide a quick-look indication of the data quality and, in the case of a parametric study helps determine the particular configuration that will provide the best flight results. The comparisons can save a large amount of wind tunnel time and thereby sizably reduce the overall cost of the program. The total data reduction flow is illustrated in Fig. 13, and typical stability data are shown in Fig. 14.

SURFACE PRESSURE TESTING

Surface pressure tests in hypersonic wind tunnels are primarily conducted in association with surface heat-transfer and/or flow-field probing measurements to provide inputs to or to validate a CFD code. Of current high interest are pressure tests defining the internal and external aerodynamics of scramjet propulsion systems.

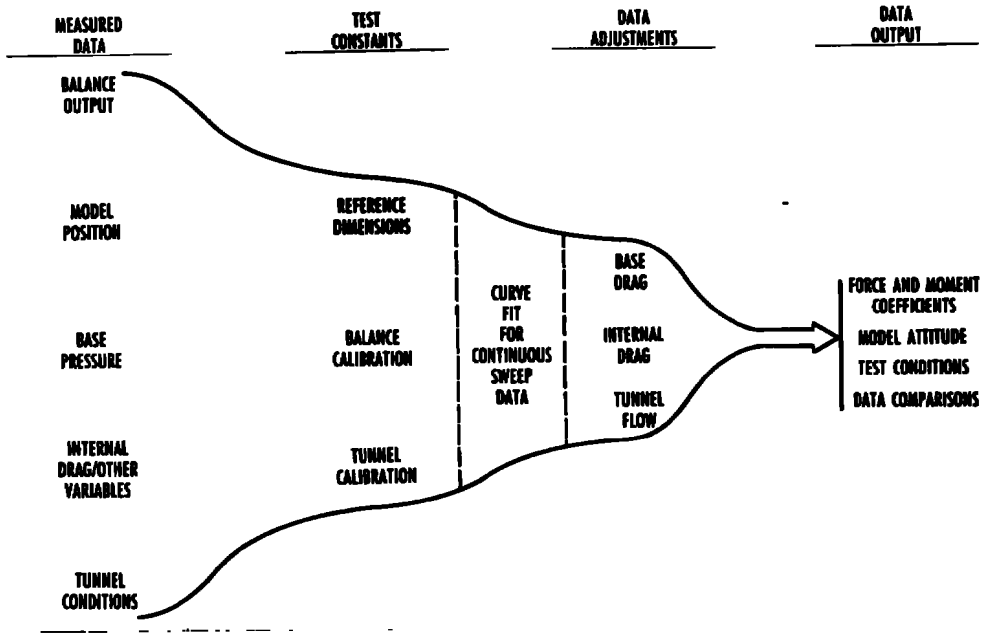

Figure 13. Data reduction.

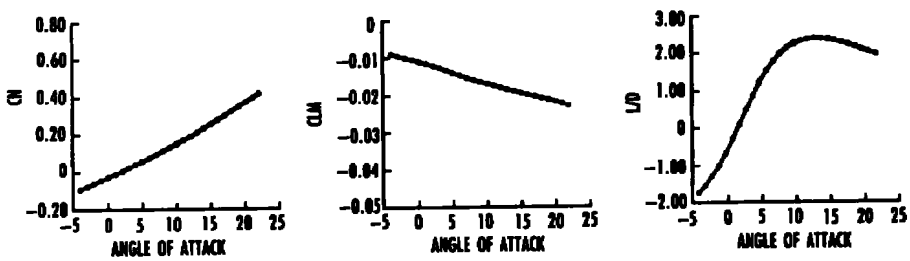

Figure 14. Example of on-line stability data.

Pressure Transducers

Static pressure levels on test models are generally very low in hypersonic flow. However, in cases of shock wave interaction and/or impingement, they can be orders of magnitude higher than the free-stream static pressure. For this reason, great care must be used in choosing the type of instrumentation to be used to obtain the best possible precision, and also to protect the measurement device from overload. In general, model surface pressures in hypersonic flow are measured with a pressure transducer similar to that shown schematicaly in Fig. 15a. This differential transducer senses the difference in pressure on the measuring side from that on the reference side. As seen by the schematic, a small difference in pressure will cause a deflection of the thin diaphragm, resulting in an electrical output from the attached strain gage. The deflection and, therefore, the output and maximum allowable pressure differential, is a function of how rigid (thick) the diaphragm is made. These transducers are manufactured in pressure ratings from a few hundredths of a psid to several thousand psid.

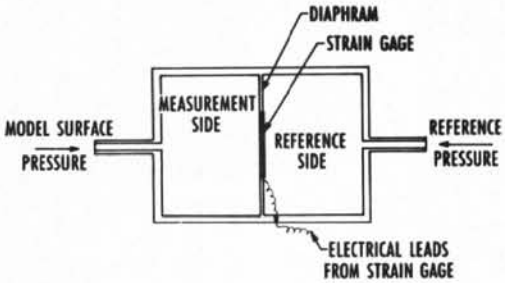

a. Pressure transducer schematic.

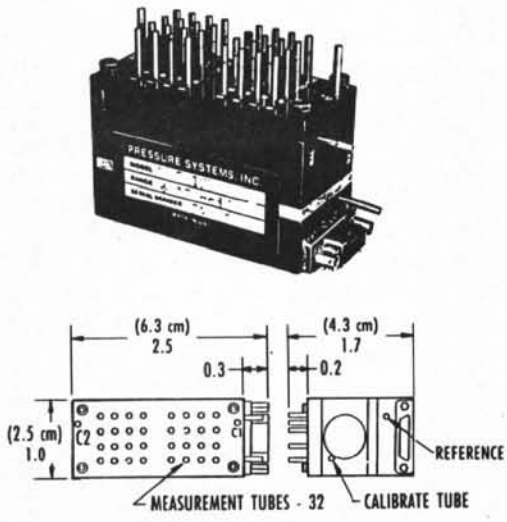

b. Electronically scanned pressure unit (ESP)

Figure 15. Pressure measurement device.

Since it is important to obtain data as quickly as possible because of the test environment and/or to reduce costs, the transducer should be located close to the point of measurement on the model to reduce the pressure stabilization time.

Miniaturization has allowed large numbers of individual transducers to be connected together into what is called an ESP (Electronically Scanned Pressure) unit. These units can usually be housed within the test model or mounted very close within the mounting hardware. They must, however, be cooled (usually with a water jacket) because the transducers are highly temperature sensitive. The advantages of these modules, in addition to their extremely small size and small volume of the overall system, is that they require only one reference line, one calibration line, and one set of electrical leads for all of the transducers instead of individual lines. The major disadvantage is that all surface pressures must be near the same value because all of the transducers within a unit have the same maximum pressure rating and, as stated, use a common reference pressure. They are, however, usually protected against a large overload. A typical unit capable of measuring up to 32 model pressures and manufactured by Pressure Systems Incorporated is shown in Fig. 15b.

Transducer Calibration

Pressure transducers must be calibrated, as in the case of the force balances, to determine the electrical output of the strain gage as a function of applied pressure differential across the diaphragm. Unlike the balance calibrations, however, the pressure transducers are usually calibrated at least once a day during use. These calibrations take only a few minutes because there is only one component and, therefore, no interactions. The calibration can be accomplished in one of several ways, depending on the type and magnitude of the rated pressure of the transducer. The most common method used for transducers rated up to atmospheric pressure is to reduce the pressure on the reference side of the diaphragm in increments by applying a known pressure less than atmosphere. The magnitude of the applied pressure is measured with accurate instrumentation (secondary standard) traceable to a primary standard. A secondary standard is a field measurement device traceable to a laboratory primary standard which is, in turn, traceable to the National Institute of Standards and Technology. Since most transducers are not linear through zero pressure differential, if values of the test pressure to

be measured are expected to be both above and below the value of the reference pressure to be used during the test, the applied calibration pressure should also cover both cases. Quite often, several individual transducers being used for a test are connected to a common reference, as is the case for the ESP units. In these cases, all transducers on a common reference can be calibrated at the same time.

If a transducer has a sealed vacuum on the reference side of the diaphragm (an "absolute" pressure transducer), or the maximum rated pressure is greater than atmospheric pressure, or it is an ESP unit of the type shown in Fig. 15, it must be calibrated from the measurement side of the diaphragm. This is accomplished by sealing off the tube going to the model surface and applying the reference pressure through a "T" as shown in Fig. 16. In the case of the ESP unit, this valve is internal to the unit; however, for other types of systems, the valving and calibration tubing must be added to the system and can become quite complicated to ensure there are no leaks anywhere in the system. The calibration pressure is applied and measured in the same manner as the reference side calibration.

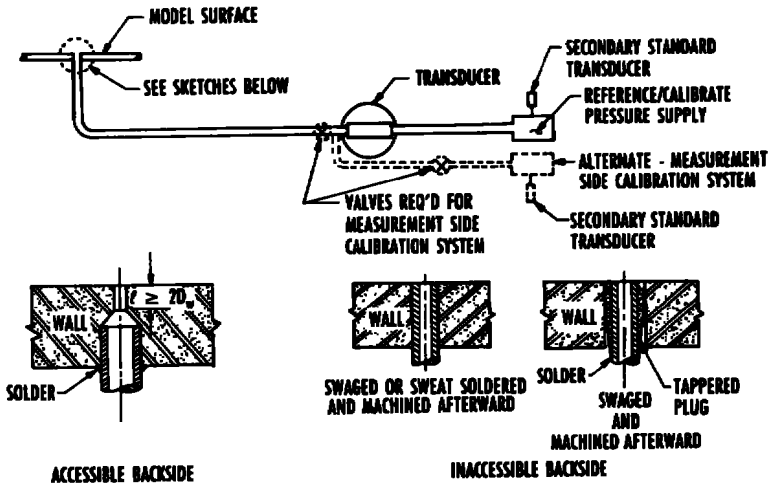

Figure 16. Pressure measurement and calibration schematic.

Model Fabrication

As in the case of the static stability model, the choice of test facility dictates the maximum size model. Weight is not a critical item in the pressure models; therefore, reinforcing and other fabrication techniques can be used to reduce the thermal distortion during testing. Pressure models for hypersonic testing are usually fabricated from stainless steel, with stainless steel tubing attached by one or more of the methods shown in Fig. 16. When the configuration is such that the backside or inside of the model is accessible, the type installation shown at the left is the most desirable. In this type installation, a small hole, usually less than 0.050 in. (1.3 mm) diam, is drilled through the model wall, a counterbore the size of the O.D. of the tube is drilled part way through from the backside, and the stainless steel tube is soldered in place. Either of the two right-hand installations can be used when there is not enough room or access to solder the tubes on the backside. Care must be used in installation and/or handling this type model, or leaks can develop around the tube or the tapered plug, resulting in measurement errors. Any of the three installations should be checked for leaks by applying a vacuum to the surface tap, sealing it off, and observing the test instrumentation over a few minutes to obtain a leak rate. The entire system must be clean and free from foreign material (such as oil), or the outgassing may appear to be a leak. The number of pressure taps on a model can be limited by available room for internal ESP units or for the tubes routed through the mounting hardware. As in the case of the force models, the scale of the pressure models and the fabrication process must be such as to maintain the fidelity of the full-scale configuration. The "as-built" location of the surface pressure taps is critical to obtaining data which will accurately predict the flight pressure loadings or which can be used to validate theoretical computer codes.

Testing Methods

Testing of surface pressure distribution models in hypersonic wind tunnels can be very time consuming and therefore more expensive than static stability testing. In the intermittent tunnels, usually data for only one model attitude per run can be obtained because of the time it takes for the pressure to stabilize. For the same reason, even in the continuous flow tunnels, it takes longer to get the pressure data over a pitch or yaw polar than even the "point-pause" type force data. Even when the model and pressure systems are optimized to reduce the required stabilization time, it still requires up to minutes per model attitude. Because of the expense in time/money, pressure tests

are usually designed for data points in wider increments than the normal force test; i.e., where data for a force test may obtained for $-15 < \alpha < +15$ in 2-deg increments, the pressure test would probably be 5-deg increments.

Data Reduction

Test data are combined with previously input calibration data (transducers and wind tunnel), and the data output parameters i.e., P, P/P_∞, C_p etc. are calculated. A data reduction technique called the pressure prediction routine can be used to reduce the amount of time required to obtain the pressure data for a given model attitude. To apply this technique, the output of the pressure transducer is recorded in uniform time increments (~1/sec) for a period of time (usually 30 sec) after the model has been set at the desired attitude. The results of these samplings are curve fit within the computer, and the results are extrapolated to the asymptotic value of the actual pressure. The technique, illustrated in Fig. 17, takes into account such things as pressure tube geometry, gas temperature, viscosity, system geometry, etc. As shown by the illustration, the actual equilibrium value of the pressure was predicted very accurately by using the input obtained during only 30 sec when it would have taken well over a minute for the system to stabilize to the final value. The wind tunnel test time/costs can be greatly reduced with very little sacrifice in accuracy by applying this technique.

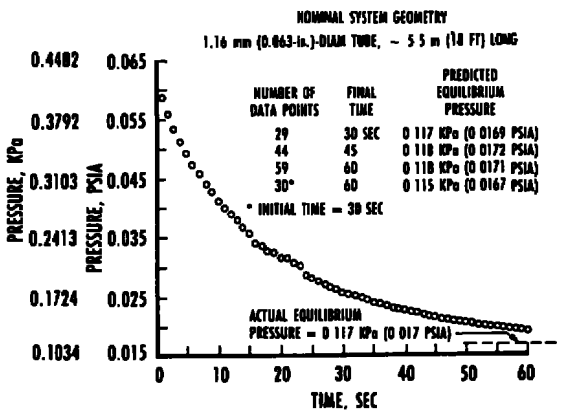

Figure 17. Typical pressure stabilization curve.

AEROTHERMAL METHODOLOGY

Fundamentals and Simulation Parameters

The requirements for developing hypersonic flight vehicles place increasing demands on ground test capabilities. Of particular concern is the requirement to demonstrate that flight components such as leading edges, cowl lips, and structural panels will survive the aerothermal flight environment. Specific components as shown in Fig. 18, can experience heating rates ranging from 200 to 2,000 Btu/ft^2-sec and surface temperatures from 1100-1940°C (2,000 to 3,500°F). Ground test of flight components have previously been performed at test facilities like those at NASA and AEDC. This section presents an overview of the materials/structures test methodology and the test techniques used in the development of hypersonic vehicle components.

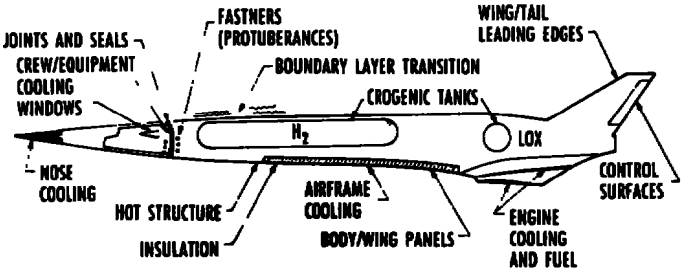

Figure 18. Typical aerothermal structures/materials issues.

A review of some fundamental heat-transfer concepts is presented in Fig. 19. The typical textbooks discuss the convective heating to a wall and relates the heat flux, $\dot{q}$, to a temperature difference, T_g-T_w. For aerodynamic heating the heat flux is also proportional to the temperature gradient at the wall, and the heat-transfer coefficient, h, is used to relate the heat flux, $\dot{q}$, and the temperature driving potential, T_r-T_w, where T_r is the recovery temperature. The experimentalist often uses the facility total temperature, T_o, in place of the more elusive recovery temperature T_r.

A common approach used to solve aerothermal issues is based on combining analysis with experimentation. It is imperative that analytical techniques be used to plan the test and to analyze the final data. The two fundamental steps in the development process are:

1. defining the flight thermal environment
2. demonstrating hardware survivability

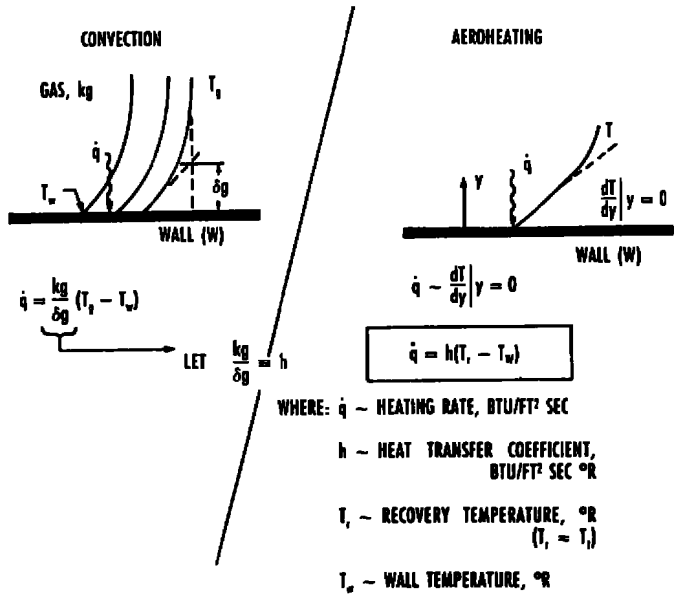

Figure 19. Basic aeroheating concepts.

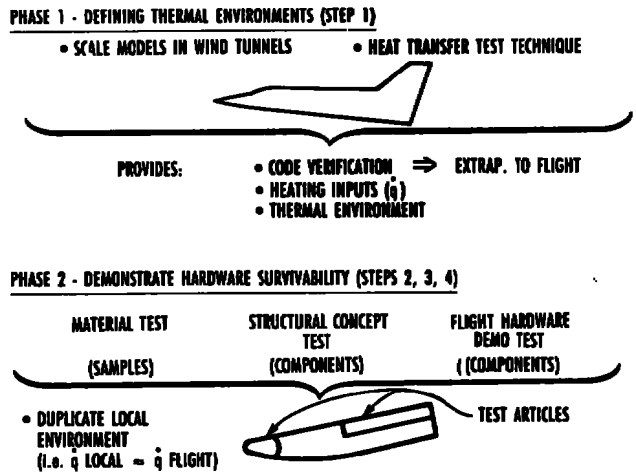

Figure 20. Methodology for aerothermal structures/materials development.

These two fundamental phases are illustrated in Fig. 20. In defining the thermal environment, the versatility of analytical tools is combined with the experimentally measured heating distributions. These data, obtained on scaled models in simulated flow environments, are used to verify the accuracy of the analytic tools. The important simulation parameters are Mach number and Reynolds number. However, it may not be necessary to match the Mach number because of the "Mach number independence principle." A commonly used procedure to define the thermal environment is to use the data obtained at Mach 8 or 10 to substantiate a code at precisely the same conditions as the experimental data. The code is then used to extrapolate the results to higher Mach numbers incorporating real-gas and viscous effects as required. This procedure is illustrated in Fig. 21, which includes the primary test facilities used to obtain heat-transfer data in the U.S. The AEDC Tunnels B and C are the national workhorse facilities in this category, and it has been estimated that 75 percent of existing hypersonic data defining thermal environments have been obtained in these tunnels.

The test techniques available to measure aero-heating are listed in Fig. 22, along with a reference which illustrates the use of the technique. Thermal mapping techniques provide a comprehensive look at the entire model and are often used to identify the location of high heating rates (e.g., shock interaction). However, the uncertainty of thermal mapping data is of the order of ± 15 percent, whereas the discrete measurement techniques can produce ± 6-percent data which are more reasonable for code validation tests. Additional details on heat-transfer measurement techniques may be found in Refs. 4, 7, and 10, and a brief overview of each technique is presented below.

Phase Change Paint Technique

The Phase Change Paint technique of measuring the heat transfer to a model surface was developed by Jones and Hunt.[11] This technique assumes that the model wall temperature re-

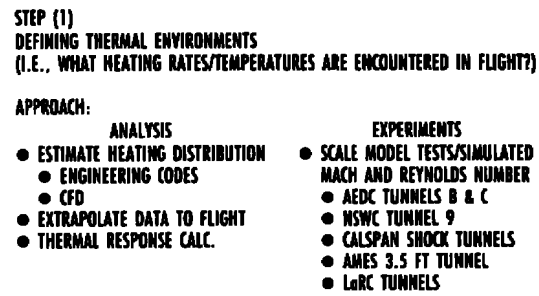

Figure 21. Development process, step 1.

	ADVANTAGES	DISADVANTAGES	REF.
THERMAL MAPPING			
• PHASE-CHANGE PAINT	VIVID ILLUSTRATION OF HOT SPOTS HIGH SPATIAL RESOLUTION	MUST REAPPLY PAINT, DATA PRESENTATION CAN BE CONFUSING	2
• IR SCANNING CAMERA	COMPUTER-GENERATED PLOTS AND COLOR MAPS, AND NONINTRUSIVE	SPATIAL RESOLUTION	3
• THERMOGRAPHIC PHOSPHOR	COMPLETE MODEL, GOOD SPATIAL RESOLUTION	MODEL PREPARATION AND DATA PRESENTATION	4,10
DISCRETE MEASUREMENTS			
• THIN-SKIN	HIGH QUALITY DATA, DENSE SPACING	EXPENSIVE MODEL FAB, CONDUCTION EFFECTS	5
• COAX GAGE	EASY TO INSTALL, CONTOURABLE, DURABLE	LOW OUTPUT, SHORT TEST TIMES	6
• SCHMIDT-BOELTER GAGE	HIGH OUTPUT, SLIGHTLY CONTOURABLE, VERY DURABLE	FAB AND CALIBRATION TIME REQUIRED	7
• GARDON GAGES (HI TEMP, LO TEMP)	YEARS OF EXPERIENCE, FAST RESPONSE	GAGE ATTRITION RATE, NOT CONTOURABLE	8
• THIN-FILM	DENSE SPACING, FAST RESPONSE, CAN BE USED ON SMALL RADII	RELATIVELY DIFFICULT INSTALLATION, MATERIAL CRACKING	9

Figure 22. Test techniques available for measurement of heat transfer.

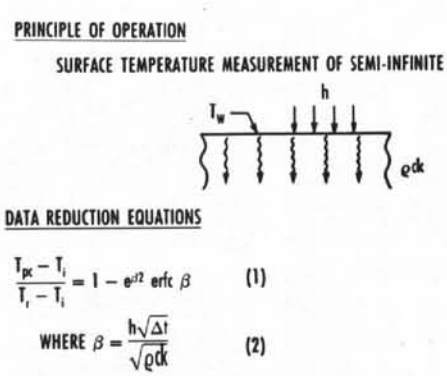

Figure 23. Phase change paint technique.

sponse is similar to that of a semi-infinite slab subjected to an instantaneous and constant heat-transfer coefficient (see Fig. 23). The surface wall temperature rise for a semi-infinite slab is given by the equations shown in this figure.

A specific value of the wall temperature (T_{pc}) is indicated by a phase change paint (Tempilaq®). These paints change from an opaque solid to a transparent liquid at a specified phase change temperature (T_{pc}). For known values of T_i, Tpc, t, and $\sqrt{\rho ck}$, the heat-transfer coefficient (h) can be calculated as a function of the time required for the phase change to occur by using

$$h = \frac{\beta \sqrt{\rho ck}}{\sqrt{\Delta t}} \qquad (3)$$

where β comes from the solution of Eq. (1) since the left-hand side is known.

Prior to each run, the model is cleaned and cooled with alcohol and then spray-painted with Tempilaq® . The model is installed on the model injection

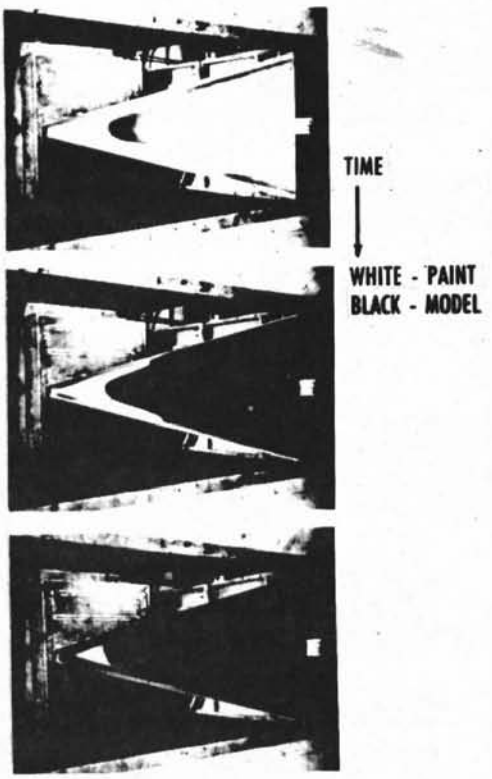

Figure 24. Typical examples of phase-change paint photographs.

mechanism at the desired test attitude, and the model initial temperature (Ti) is measured. The model is then injected into the airstream for approximately 25 sec, and during this time the model surface temperature rise produces isotherm melt lines. The progression of the melt lines is photographed with 70-mm sequenced cameras operating at one or two frames per second. Typical examples of phase change paint photographs obtained during a run are presented in Fig. 24, and an example of phase change

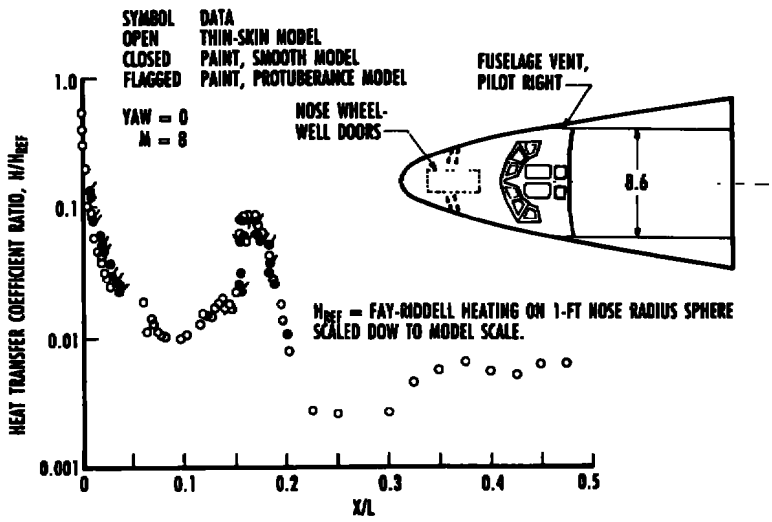

Figure 25. Leeward centerline heat-transfer distributions at $Re_{\infty_L} = 8.6 \times 10^6$, $\alpha = 30$ deg.

paint data compared to thin-skin data is presented in Fig. 25. This figure also illustrates a common technique used to extrapolate wind tunnel heating distributions to flight. The wind tunnel data are normalized by the Fay-Riddell stagnation point heating on a 1-ft-radius sphere scaled down to the model scale. To obtain heating rates in flight, the distribution is multiplied by the Fay-Riddell heating on a 1-ft nose radius sphere "flown along the flight trajectory." The basic assumption is that the distribution at M = 8 is unchanged from tunnel to flight.

A complete description of the phase change paint technique as applied to a particular test situation is presented in Ref. 2.

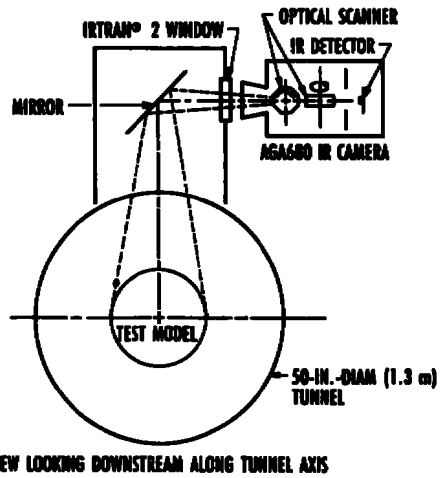

Figure 26. Sketch of typical IR camera installation.

Infrared Scanning

Thermal mapping techniques used in wind tunnel test applications generally involve the use of heat-sensitive model surface coatings. The major drawback to these methods has been the time required to obtain quantitative data from photographic test results.

With an infrared (IR) scanning camera system, heat-transfer coefficient data in the form of tabulations, plots, and surface maps are produced within minutes of test run completion.

A typical installation of the AGA Thermovision 680 scanning camera for an aerodynamic heating test is sketched in Fig. 26. The camera is positioned outside of the wind tunnel environment. The infrared radiation emitted by the test model within the field of view of the camera is collected by the system optics and focused on the camera detector. The signal generated by the detector is proportional to the detected infrared radiation. Two rotating prisms form an optical scanner which controls the position of the instantaneous field of view (IFOV) of the camera.

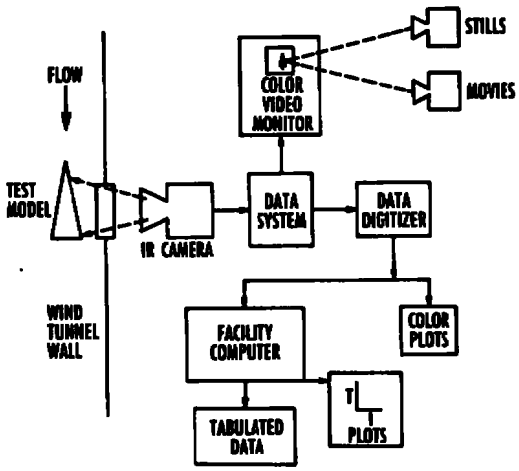

Figure 27. Infrared system schematic.

The complete infrared system in use at AEDC is schematically illustrated in Fig. 27. The system is composed of the test model, the AGA 680 camera, and a data system to collect, digitize, and convert the camera signal to the desired data output. For a typical

test, there are several modes of data output that can be selected to fulfill the test requirements. One type of data output is a tabulated output of model surface temperature or heat-transfer coefficient for each desired position within the total field of view. A capability of presenting the temperature map of the model surface in the form of a color plot is used, and a sample is presented in Fig. 28. Other forms of data presentation consist of both 70-mm photographs and 16-mm movies of the color video monitor.

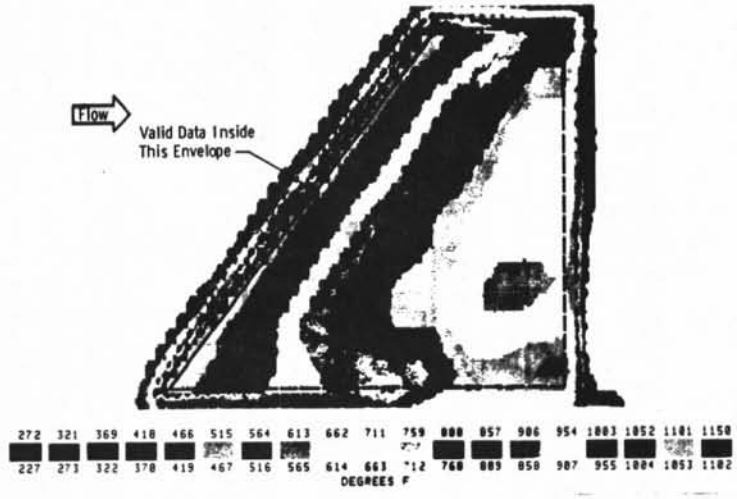

Figure 28. Illustration of IR thermal mapping data.

To aid in the understanding and interpretation of the data obtained with the IR scanning system requires the following: (1) a definition of some basic terminology associated with the IR system and the data, and (2) a review of basic IR system operational characteristics and limitations.

The total field of view of the camera at the wind tunnel centerline is a function of the lens selected for the camera and the distance from the camera focal point to the centerline. The desired total field of view is determined based on the size of the test model to be viewed and the spatial resolution (to be discussed later) that is desired. The total field of view is a rectangle as shown in Fig. 29a. One complete scan of this total field of view is defined as a frame of data. Each frame of data is composed of a matrix of 70 line scans, each containing 110 points, for the total of 7,700 discrete measurements. Each line/point combination identifies the location of the centerline of the IFOV of the camera as it scans the total field of view.

The IFOV of the camera is specified as the angle in milliradians subtended by the projected detector area in the object plane. Since the detector in the AGA 680 camera is circular in scope, a "spot diameter" is viewed in the object (test) plane (see Fig. 29a).

The ability of the IR system to track a temperature profile across a "worst case" step-heating gradient will be discussed to aid in the understanding of the data. Assume that the IR camera is scanning along the centerline of a target that is composed of a plate at a uniform temperature, T_C, that has a circular protuberance at an elevated uniform temperature of T_H as shown in Fig. 29b. For a system with perfect optics and electronics, the ability to track a step increase in temperature is a function of only the IFOV which determines the scanning spot diameter. If the camera had an infinitesimal IFOV, the temperature profile would be tracked exactly as shown in Fig. 29b. This case is of academic interest only, but represents what would be required to track a step change in temperature exactly.

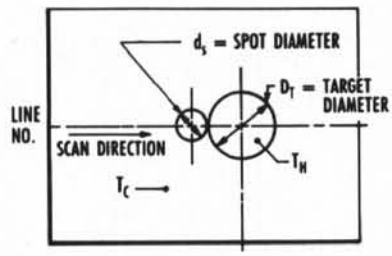

a. IR target

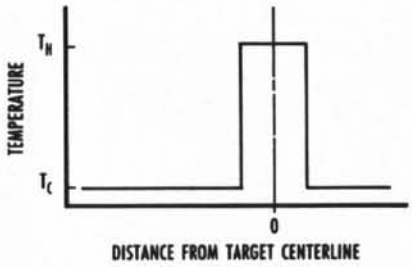

b. IFOV = infinitesimal

Figure 29. IR scanning of a step change in temperature.

Next, we will assume a practical spot diameter of 0.16 in. (4 mm) based on an 8-deg lens viewing the

target shown in Fig. 29 at a distance of 76 in. (1.9 mm) (typical). The nominal temperature profiles for various target diameters are presented in Fig. 30. This shows that the temperature profile is not tracked exactly. This is true because at each of the IR measurement points, the radiation is integrated over the spot area. When the diameter of the target is equal to the diameter of the scanning spot, the correct temperature would be recorded at only one scan position. For a target diameter smaller than the spot diameter, the IR system would never record the true temperature of the protuberance.

When the IR scan changes from viewing the background temperature to viewing a heated target, such as the edges of a flat target, the temperature in a region along the leading edge is invalid because of these same integrated effects. This region of invalid data is indicated on the color plot in Fig. 28.

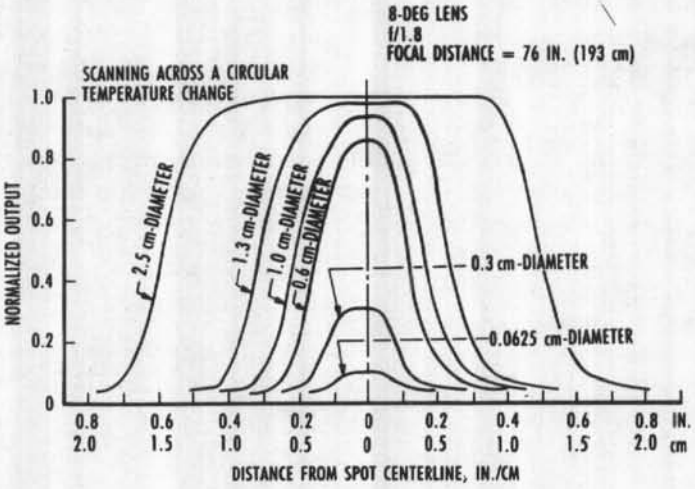

Figure 30. Determination of spatial resolution.

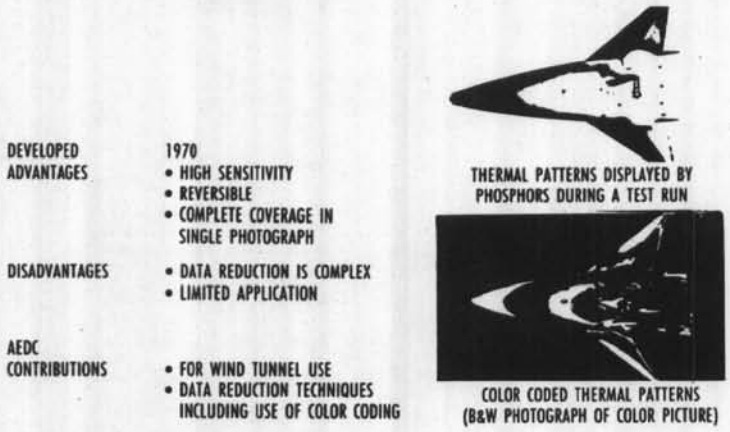

Figure 31. Thermal mapping (thermographic phosphors).

As a result of the limitation discussed above, the IR scanning technique of obtaining heat-transfer data has not been used in recent years at AEDC. However, a more complete description of the infrared system, the data reduction, testing techniques, and presentation of sample test results can be found in Ref. 3.

Thermographic Phosphor Paint

Thermographic phosphors paints are sensitive to temperature and, as the model surface temperature increases, their luminosity decreases. The luminosity of these paints is typically excited by UV or laser light and, as the temperature patterns develop, they are photographed (see Fig. 31) or recorded with a video camera. As recently as 1990, K. W. Nutt[10] presented a comprehensive discussion of the thermographic phosphor technique. The reader is referred to those notes for this specific thermal mapping technique. Thermographic phosphor paints have been used both in wind tunnel testing and in turbine engine tests. In the wind tunnel, these paints are applied to models to measure surface temperature patterns which can be used to infer heating rates. In turbine engine tests, the phosphor paints have been applied to turbine blades to infer temperature. Temperature measurement with thermographic phosphors is practical from about 100 to 900°F (38-482°C).

Discrete Measurement Techniques

Thin-Skin

The thin-skin technique (see Fig. 32) has been used for many years and remains one of the most accurate and reliable methods available.[5] Thermocouple installation is a key concern in this technique, and experience indicates that the method illustrated in Fig. 33 produces quality data. The reduction of thin-skin temperature data to coefficient form normally involves only the calorimeter heat balance for the thin skin as shown in Equations 4 and 5.

$$\dot{q}_{in} = \dot{q}_{stored\ in\ skin}$$

$$\dot{q} = \varrho bc\ dT_w/dt \tag{4}$$

$$h = \frac{\dot{q}}{T_r - T_w} = \frac{\varrho bc\ dT_w/dt}{T_r - T_w} \tag{5}$$

Thermal radiation and heat conduction effects on the thin-skin element are neglected in the data reduction, and the skin temperature response is assumed to be due to convective heating only. It can be shown that for constant T_r, the following relationship is true:

$$\frac{d}{dt}\left(\ln\left[\frac{T_r - T_i}{T_r - T_w}\right]\right) = \frac{dT_w/dt}{T_r - T_w} \tag{6}$$

Substituting Eq. (6) in Eq. (5) and rearranging terms yields:

$$\frac{h}{\varrho bc} = \frac{d}{dt}\left(\ln\left[\frac{T_r - T_i}{T_r - T_w}\right]\right) \tag{7}$$

PRINCIPLE OF OPERATION

CALORIMETRY (HEAT IN = HEAT STORED IN SKIN)
i.e. CONDUCTION = 0
RADIATION = 0

DATA REDUCTION EQUATIONS

$\dot{q} = \varrho bc \frac{dT_w}{dt}$

$h = \frac{\dot{q}}{T_r - T_w}$

$\dot{q}$ ~ Btu/FT² SEC
h ~ Btu/FT² SEC °F
ϱ ~ MATERIAL DENSITY
b ~ SKIN THICKNESS
c ~ MATERIAL SPECIFIC HEAT

Figure 32. Thin-skin technique.

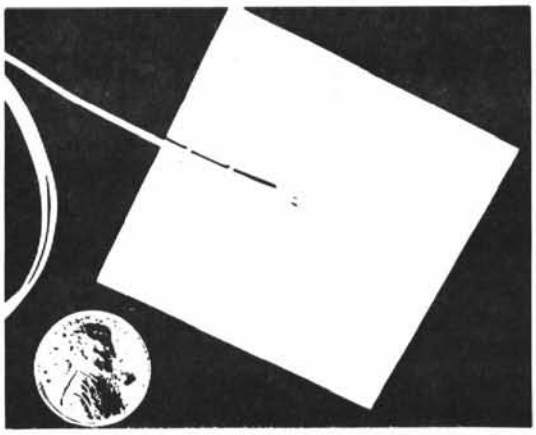

Figure 33. Typical thin-skin thermocouple installation.

Since h, ϱ, b, and c are constants, then the derivatives in Eq. (7) must also be a constant. Hence, the term

$$\ln\left[\frac{T_r - T_i}{T_r - T_w}\right] \tag{8}$$

is linear with time. This linearity assumes the validity of Eq. (7) which applies for convective heating only. Thus, if the data show a nonlinearity, effects other than convective heating are present. In most cases, the nonlinearity will be caused by conduction effects. Machine plots of data from each thermocouple provide the opportunity for quick visual examination of test data with the objective of evaluating conduction effects. Once areas and/or time frames during which significant conduction effects were present are identified, the remaining valid data are used to calculate the heat transfer coefficient via Eq. (7).

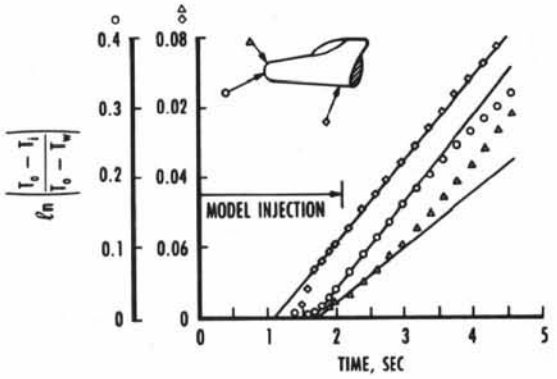

Figure 34. Representative thin-skin data.

Representative data which demonstrate the above procedure are shown in Fig. 34. Thermocouples were chosen which represent cases of no conduction, conduction away, and conduction into the thermocouple vicinity. Note that steady heating was not established until about 1.75 sec. This was caused by the process of injecting the model into the flow. The injection was actually completed at 2.10 sec. The nose thermocouple output (circles) is observed to be linear to about 3 sec, and then it begins to fall away from the initial slope. This indicates heat being lost from this area, as would be expected in a nose or leading-edge situation. Around the nose (triangles), the data are linear only up to about 2.60 sec, and then the slope begins to increase, indicating heat flow into this area. This is most likely some of the heat being lost by the nose region. Finally, a thermocouple further back on the body (diamonds) shows no conduction effects for the entire run. Obviously, longitudinal temperature gradients are small in this area, and the observed

heating is solely due to convection. The magnitude of conduction effects can be estimated directly from these plots since the change in slope with time is directly proportional to the conduction error. Once these preliminary evaluations have been made and appropriate data reduction times selected which avoid the injection transient and conduction effects, the second step of the data reduction process can proceed. Linear least-squares curve fits of the selected data are obtained, and evaluations of the heat-transfer coefficients [Eq. (7)] are made. An illustration of thin-skin data quality is presented in Fig. 35.

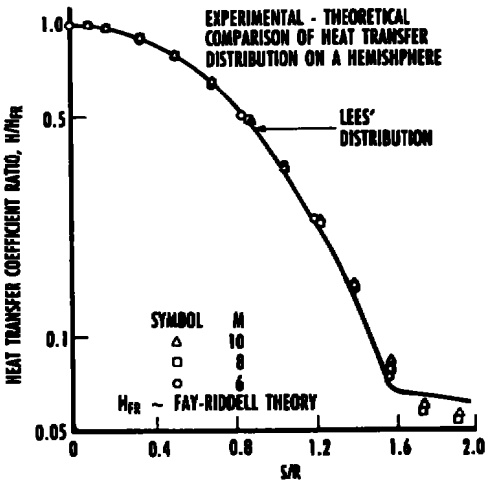

Figure 35. Illustration of thin-skin data quality.

A complete discussion of the thin skin test technique as applied to a particular test situation (including presentation and analysis of the resultant data) is contained in Ref. 5.

Coaxial Gage

For applications where surface contour is critical or where measurement at severe wall temperature conditions is required, the coaxial thermocouple gage (or coax gage) is often used. The coax gage (Fig. 36) is simply a surface thermocouple which is comprised of an insulated Chromel® wire fixed concentrically within a constantan jacket. The thermocouple junction is formed at the sensing surface by blending the two materials together with a file. This filing process is also used to contour the gage surface to exactly match the model surface. Because of its simple construction, the coax gage can be made very small; gage diameters of 0.165 cm (0.065 in.) and 0.318 cm (0.125 in.) are in common use. Also, because of its construction, this gage has a very large temperature operating range (−320 to 1,000° F and above) as compared to other measurement techniques.

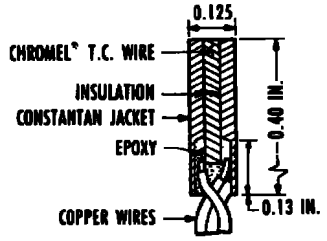

Figure 36. Coax gage construction.

The data reduction equation used to obtain the heat flux from the measured temperature of a coax gage is as follows:

$$\dot{q}(t_n) = \frac{2\,C\,(t_n)}{\sqrt{\pi}} \sum_{j=1}^{n} \frac{\sqrt{T_{w_j} - T_{w_{j-1}}}}{\sqrt{t_n - t_{j-1}} + \sqrt{t_n - t_j}} \quad (9)$$

where $\dot{q}$ = surface heat flux at time t_n

T_{w_j} = surface temperature at time t_j

The term $C\,(t_n)$ is essentially the scale factor for each coax gage with the thermal properties temperature dependence included.

The semi-infinite solid assumption used in the development of the data reduction technique described above is valid for only a limited time since the gage has a finite depth. Another factor which can limit the accuracy and/or run time is lateral conduction effects. The combined thermophysical properties of Chromel and constantan are quite similar to stainless steel. Thus, if mounted in a steel model, the conduction errors usually become negligible for run times less than about five seconds.

The extremely fast response of these gages (50 μsec to a step input) makes possible their application to continuously moving models or moving components of models.

The sketch in Fig. 37 illustrates the installation of coax gages in the body flap of the orbiter model which was used to evaluate the continuous-sweep concept. The results presented in Fig. 38 are typical of data obtained during testing of the orbiter body flap and illustrate the excellent agreement obtained

between sweep measurements and discrete (fixed angle) measurements. These data are from the same gage operated in both a discrete (fixed point) and sweep mode. Such results indicate that reliable heat-transfer data can be obtained if certain precautions are followed. In particular, the data acquisition rate, the model sweep rate, and the method of data filtering (or averaging) used to reduce data scatter must be coordinated to meet test data quality requirements. Also, care must be taken to avoid violating the assumption of a model wall thermal response identical to that of a semi-infinite solid. This implies that sweep data should be obtained only during moderate (less than 5 sec) aeroheating exposures. For further details regarding test results and analysis of the advantages and restrictions of this technique, see Ref. 6.

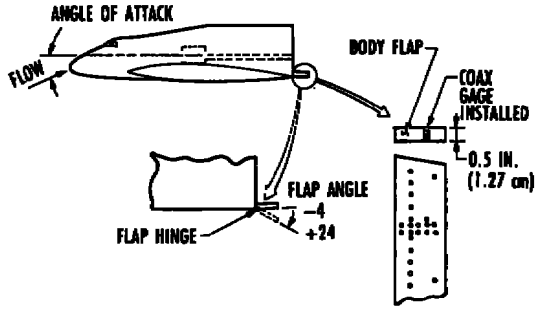

Figure 37. Illustration of flap sweep and gage installation.

Schmidt-Boelter Gage

The Schmidt-Boelter gage (Fig. 39) alleviates many disadvantages found in other gages. Schmidt-Boelter gages have seen considerably wider usage in recent years for heat-transfer measurements in continuous-flow wind tunnels and flight test applications.[7] This is primarily due to the attractive operating characteristics common to this type sensor. These include excellent durability, good sensitivity,

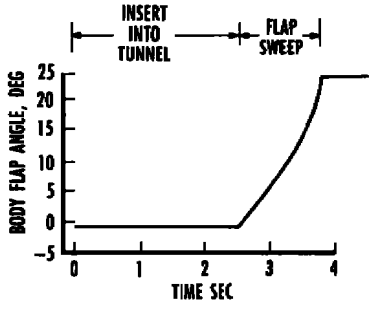

a. Body flap sweep profile

Figure 38. Continuous sweep coax-gage data.

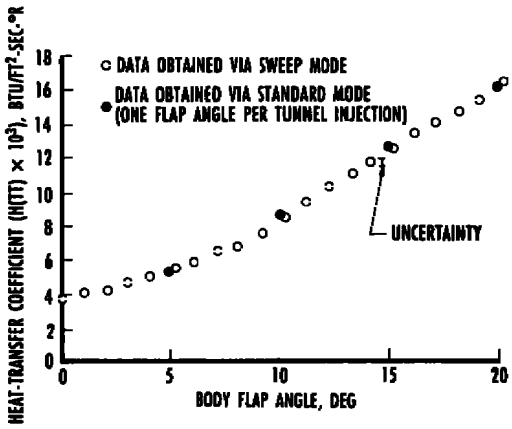

b. Comparison of data obtained in sweep and standard modes.

Figure 38. Concluded.

self-generating output signal directly proportional to incident heat flux, continuous service temperature of 700°F, and semicontourability.

The principle of operation of the Schmidt-Boelter gage is based on axial heat conduction, and involves measuring the temperature difference, ΔT, between

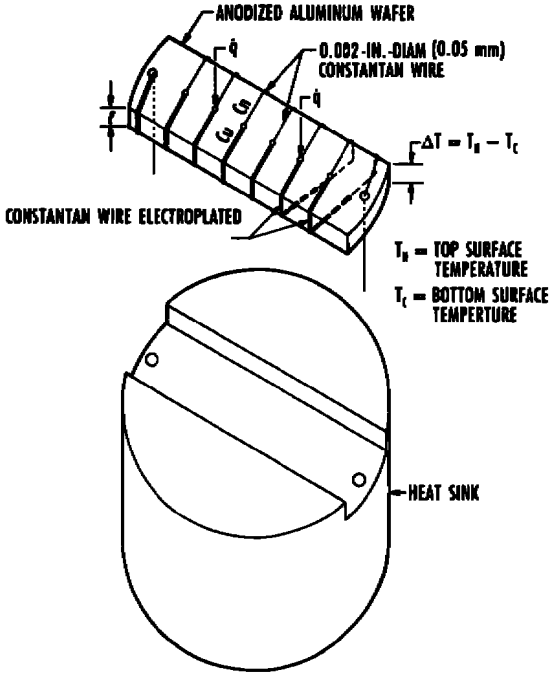

a. Schmidt-boelter gage concept

Figure 39. Construction details of Schmidt-Boelter gage.

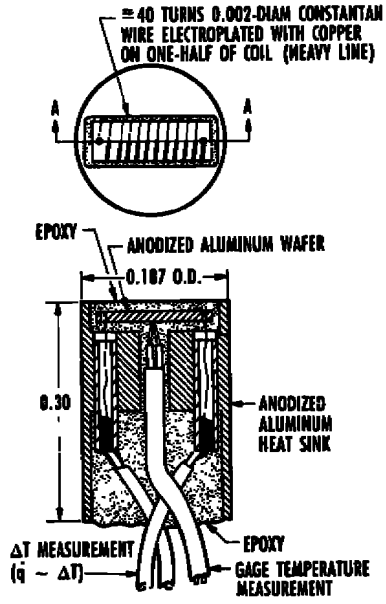

b. Section drawing of 3/16-in.-diam Schmidt-Boelter gage

Figure 39. Concluded.

two parallel planes on the top and bottom of a slab or wafer which is backed by a heat sink, as shown in Fig. 39. This temperature difference is generally measured with a differential thermocouple. The hot junction temperature, TH, is on the top surface of the slab, and the cold junction temperature, TC, is on the bottom surface. The material and thickness of the slab can vary widely; the heat sink is usually a material with a high thermal conductivity such as aluminum, copper, etc. Excellent sensitivity is achieved by using a series thermocouple (thermopile) arrangement to detect the temperature difference between the top and bottom surfaces of the slab. The thermopile is constructed by winding 20 to 40 turns of small (0.002-in.-diam) constantan thermocouple-grade wire around the anodized aluminum wafer. One-half of the constantan coil is electroplated with copper, creating a multi-element copper-constantan differential thermocouple. The steady-state output signal of the transducer is proportional to the incident heat flux at the surface ($\dot{q}$).

Experimental calibrations of Schmidt-Boelter gages are performed using a radiant heat source as described in Ref. 12. These experimental procedures enable a calibration scale factor (CSF) to be obtained for each gage and heating rates are calculated as follows:

$$\dot{q} = (CSF)\,(\Delta E) \qquad (10)$$

Representative data from Schmidt-Boelter gages installed in a flat plate model are shown in Fig. 40.

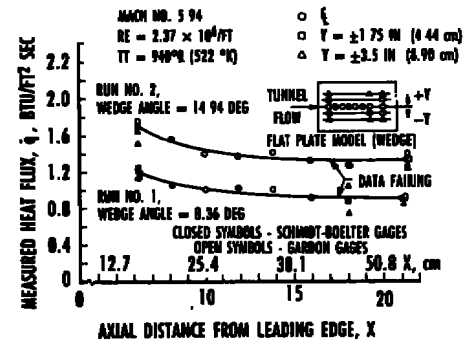

Figure 40. Axial heat flux distribution on a flat plate model.

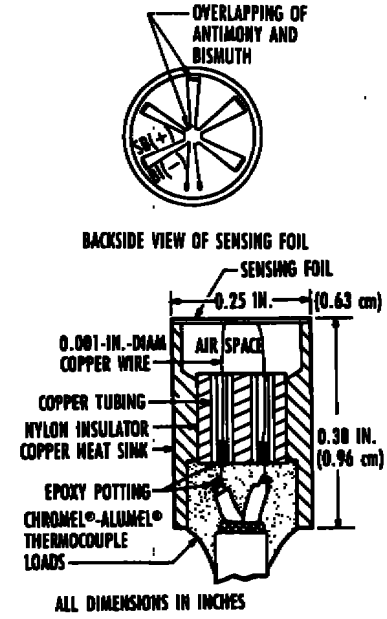

Figure 41. High-sensitivity gardon gage.

Gardon Gage

The Gardon gage differs from other types of heat gages because its principle of operation is based on lateral heat conduction.

There are two types of Gardon gages. The standard Gardon gage output is the result of a junction formed by a thin copper wire connected to the center of a thin constantan sensing disk on the gage face. The other type of heat gage (thermopile Gardon gage) derives its output from overlapping antimony and bismuth deposits, forming a thermocouple which senses the temperature gradient on the back side of the sensing foil (see Fig. 41). This arrangement greatly increases the output of these

gages as compared to the standard Gardon gage, and for this reason it is more commonly used.

With $\dot{q}$ and T_w obtained from gage measurements, the heat-transfer coefficient can be calculated as previously stated:

$$h = \frac{\dot{q}}{(T_r - T_w)} \tag{11}$$

Unfortunately, the recovery temperature is not always known and its determination can become a significant factor in utilizing test data, particularly for situations where $T_r - T_w \leq 100$ °C. However, the following technique has been developed for determination of T_r for these cases. Utilizing the continuous gage output of $\dot{q}$ and T_w and rearranging Eq. (11), we have:

$$\dot{q} = hT_r - hT_w \tag{12}$$

Equation (12) has the form of a straight line when h and T_r are assumed constant (which is valid for this application)

$$\dot{q} = A_0 + A_1 T_w \tag{13}$$

Also note that $h = -A_1$ and setting $\dot{q} = 0$ leads to the relationship for T_r,

$$T_r = -A_0/A_1 \tag{14}$$

A description of the Gardon gage technique described above as applied to a specific test situation is included in Ref. 8.

Thin Film

Standard methods for obtaining convective heating data (i.e., heat gages, thin-skin thermocouples, etc.) on wind tunnel models are restricted to model regions with relatively flat surfaces and/or small surface heating gradients. These limitations have precluded obtaining accurate heating rate measurements in the most critical areas of a vehicle, such as the wing and fin leading edges, nosetips, interference flow regions, etc. By applying small thin-film resistance thermometers to a contoured ceramic surface (Fig. 42), a technique has been developed[9] for making measurements in these regions, and a philosophy for data reduction was derived which allows application of this technique to models tested in continuous-flow wind tunnel facilities.

Heating distributions on the wing leading edge of a 0.025-scale space shuttle orbiter were measured during a recent test. Approximately 6 in. of the wing leading edge of the model was replaced by an instrumented insert as shown in Fig. 42. The insert was fabricated as illustrated in Fig. 43. MACOR® 9658 (a glass ceramic material produced by Corning) was selected as a substrate because of its machinability and good thermal insulating properties. The MACOR substrate was machined to an external contour corresponding to the wing leading edge with a channel in the back side to accommodate routing of electrical lead wires. Fifty-four small holes were drilled normal to the surface of the test article into the lead wire channel on two angular rays to provide 27 thin-film sensors 0.76 cm (0.30 in.) long with spacings of 0.25 cm (0.10 in.) between them. Chromel pins were cemented into the holes, with the tops of the pins protruding slightly from the sensing surface of the test article and the back of the pins extending well into the lead wire channel. The sensing surface of the test article was then polished smooth ($\sim 12 \times 10^{-6}$ cm roughness) so the Chromel pins were flush with the sensing surface. Thin-film resistance thermometers of Hanovia Liquid Bright® platinum were painted across the 0.76 cm (0.30 in.) space between the pins. A silver preparation was then painted over the Chromel pins and in the area immediately surrounding the pins. The entire assembly was then successively fired and cooled

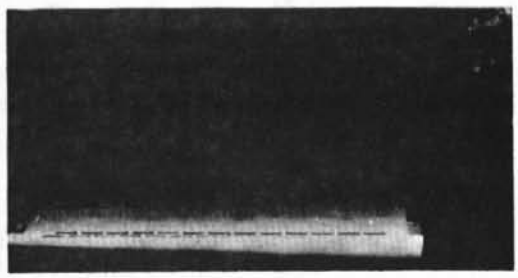

a. View of exposed surface of instrumented insert.

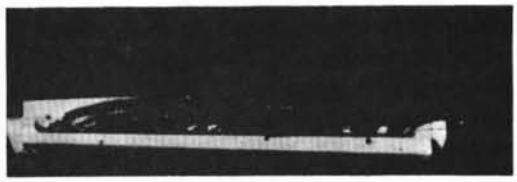

b. View of backside of instrumented insert.

Figure 42. Space shuttle orbiter instrumented wing leading edge.

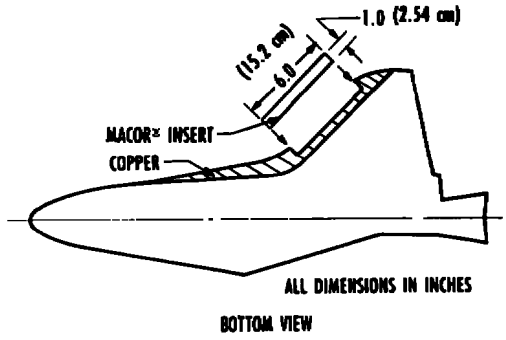

c. Sketch of instrumented insert installation in orbiter wing

Figure 42. Space shuttle orbiter instrumented wing leading edge.

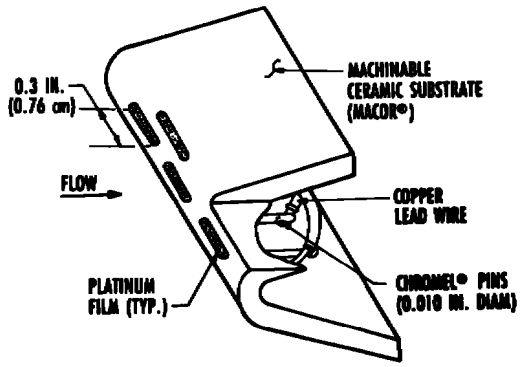

Figure 43. Typical thin-film installation.

through several cycles to put a permanent set in the resistance vs. temperature characteristics of the thin films. After the firing, the area immediately surrounding the pins was polished to a smooth finish. Copper lead wires were soldered to the pins on the back side of the test article.

Each film provides a measurement of the surface temperature response of the wing leading edge during exposure to wind tunnel conditions. A sample of the temperature transient results is presented in Fig. 44. The heat-transfer rate is calculated from the temperature transient curve via semi-infinite solid response considerations, then a correction is applied to account for the effect of the small local radius of the surface. The correction technique is based on finite-element modeling of the heat conduction in the wing leading edge and was verified by a series of experiments on cylindrical leading-edge pieces. Typical results from the space shuttle orbiter wing leading-edge tests are illustrated in Fig. 45.

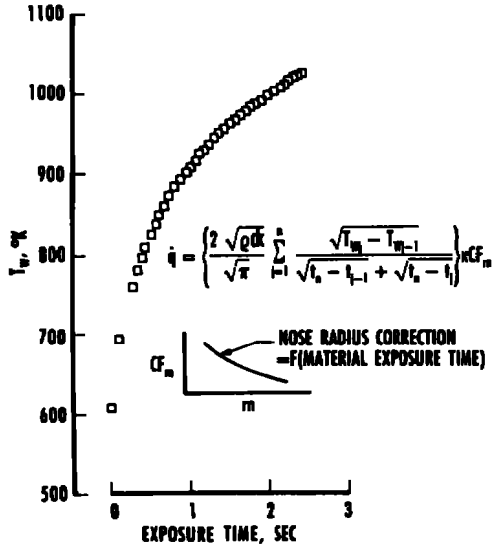

Figure 44. Representative thin-film data.

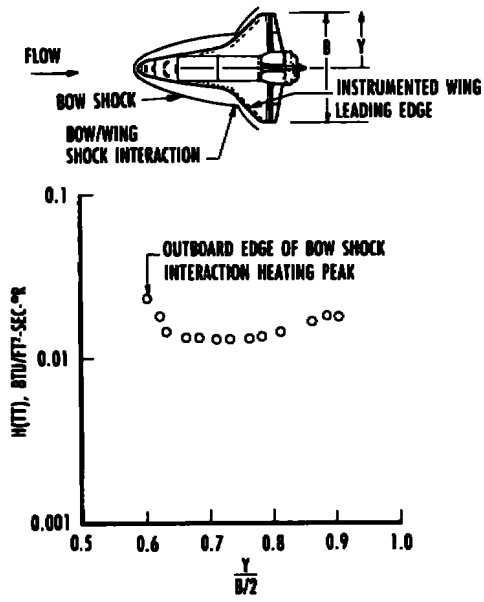

Figure 45. Typical thin-film data application.

Gage Calibration

Experimental calibrations of heat flux gages are performed using a radiant heat source. These experimental procedures enable a calibration scale factor (CSF) to be obtained for each gage, allowing heating rates to be calculated. AEDC has recently developed a high-heat flux gage calibrator (Fig. 46). Through efficient collection of the radiant energy from a high-intensity xenon arc lamp, a lab calibration apparatus (Fig. 46a) delivers up to 1,500 w/cm^2-sec. Emphasis has been placed on uniformity (Fig. 46b), and repeatability. Continued development is underway to

calibrate a gage at elevated temperatures to account for gage material property variations with temperature.

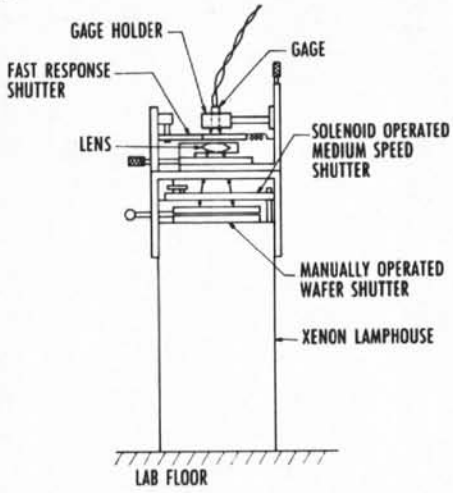

a. Apparatus

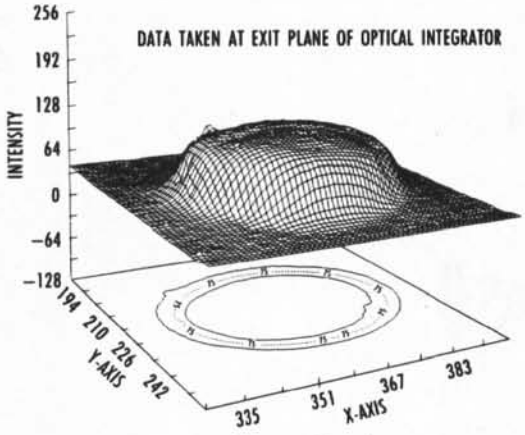

b. Heat flux uniformity

Figure 46. Capability for high heat-flux calibration.

SUMMARY

The complexities of hypersonic vehicles challenge the experimentalist to develop new facilities and innovative test techniques. This section briefly discussed the large variety of ground testing techniques that can be used in conjunction with analytical tools to develop hypersonic flight vehicles and demonstrate their survivability and performance. The variety of test techniques available to the experimentalist continues to grow, and the importance of his selection is compounded by rising test costs. There are many factors that influence the selection of a test technique, but clearly the number one consideration must be the test objective. A precisely defined test objective, coupled with comprehensive pretest planning, are essential for a successful test program. Designers and system engineers are strongly encouraged to contact test engineers at the facilities for the most recent developments and improved test capabilities.

REFERENCES

1. Bernstein L. (1975) "Force measurements in short duration hypersonic facilities." AGARDograph 214.

2. Matthews, R. K. and Gilley, G. E. "Reduction of Photographic Heat-Transfer Rate Data at AEDC." AEDC-TR-73-90 (AD-762928), June 1973.

3. Boylan, D. E., Carver, D. B., Stallings, D. W., and Trimmer, L. L. "Measurement and Mapping of Aerodynamic Heating Using a Remote Infrared Scanning Camera in Continuous Flow Wind Tunnels." AIAA 10th Aerodynamic Testing Conference, San Diego, CA, April 19-21, 1978.

4. Trimmer, L. L., Matthews, R. K., and Buchanan, T. D. "Measurement of Aerodynamic Heat Rates at the von Karman Gas Dynamics Facility." International Congress on Instrumentation in Aerospace Simulation Facilities, September 1973.

5. Carter, L. D. and Kaul, C. E. "Heat Transfer Tests on the Rockwell International Space Shuttle Orbiter With and Without Simulated Protuberances." AEDC-TR-75-20 (AD-A012876), July 1975.

6. Wannenwetsch, G. D. and Martindale, W. R. "Roughness and Wall Temperature Effects on Boundary Layer Transition on a 0.0175-Scale Space Shuttle Orbiter Model Tested at Mach Number 8." AEDC-TR-77-19 (AD-A038895), April 1977.

7. Matthews, R. K., Nutt, K. W., Wannenwetsch, G.D., Kidd, C. T., and Boudreau, A. H. "Developments in Aerothermal Test Techniques at the AEDC Supersonic/Hypersonic Wind Tunnels." Vol. 103, AIAA Progress in Astronautics and Aeronautics, 1986.

8. Matthews, R. K. "A Summary Report on Store Heating Technology." AEDC-TR-78-46 (AD-A059415), September 1978.

9. Wannenwetsch, G. D., Ticatch, L. A., Kidd, C. T., and Arterbury, R. L. "Measurement of Wing-Leading-Edge Heating Rates on Wind Tunnel Models Using the Thin-Film Technique." AIAA Paper 85-0972, June 1985.

10. Nutt, K. W. "Thermographic Phosphor Technique." von Karman Institute for Fluid Dynamics, Lecture Series 1990-05, June 1990.

11. Jones, R. A. and Hunt, J. L. "Use of Fusible Temperature Indicators for Obtaining Quantitative Aerodynamic Heat-Transfer Data." NASA TR-R-230, February 1966.

12. Kidd, C. T. "Determination of the Uncertainty of Experimental Heat-Flux Calibrations." AEDC-TR-83-13 (AD-A131918), August 1983.

MATERIALS/STRUCTURES TESTING

by
R. K. MATTHEWS
Senior Staff Engineer
Calspan Corporation/AEDC Operations
Arnold Engineering Development Center

ABSTRACT

The requirements for developing hypersonic flight vehicles place increasing demands on ground test capabilities. Of particular concern is the requirement to demonstrate that flight components such as leading edges, cowl lips, and structural panels will survive the aerothermal flight environment. Specific components can experience very high heating rates and surface temperatures from 1,100-1,950°C (2,000 to 3,500°F). In the U.S., ground test of flight components have previously been performed at test facilities like those at NASA and AEDC. This section presents an overview of the materials/structures test methodology used in the development of hypersonic vehicle components.

NOMENCLATURE

c	Specific heat
d_p	Particle diameter, microns
k	Conductivity
LDV	Laser doppler velocimeter
M	Mach number
N_d	Particle number density
p	Pressure
P_o	Total pressure
$\dot{q}$	Heating rate
T_o	Total temperature
T_w	Wall temperature
V_p	Particle velocity
ϱ	Material density
τ	Shear
μ	Microns

Subscripts

L	Local conditions

INTRODUCTION

In the development of hypersonic vehicles, structural survivability is of fundamental concern, specifically for components that comprise the external surface of the vehicle (see Fig. 1). For the purposes of these notes the term "structural components" includes the following:

* fuselage, wing, or tail panels up to 6 ft (1.8 m) long and 4 ft (1.2 m) wide
* protuberances, gaps, joints, seals, and the surrounding structure

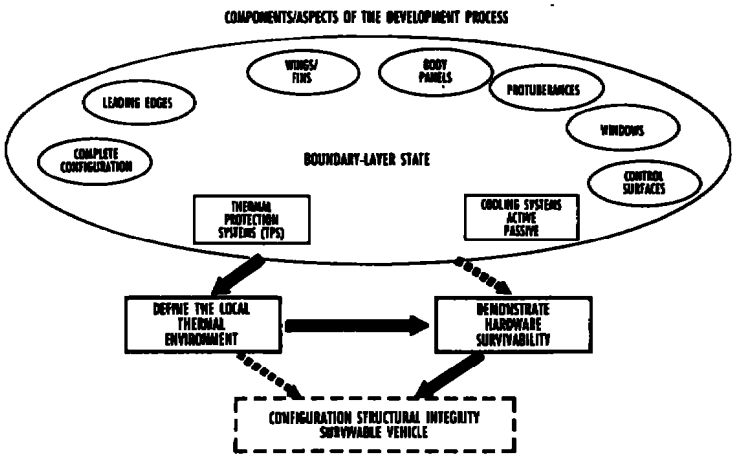

Figure 1. Development of vehicle structural integrity.

* nosecaps
* wing leading edge sections
* cowl lip sections
* control surfaces
* fins
* inlets
* radomes
* antenna windows

Structures larger than those listed above would be too big for a high-enthalpy airflow facility and typically are tested in a structures test facility using radiant heating. A structures test facility (no-flow) is also best suited to perform life-cycle testing.

In contrast, airflow facilities can provide a better simulation of flight and a more comprehensive evaluation of potential failure modes. An obvious example is the case where the hot airflow leaks into the substructure and exposes low-temperature elements to very high temperatures. In addition, an airflow facility is needed to test components for which the primary failure mode is related to aerodynamic heating, shear, acoustics, or vibration.

AEROTHERMAL METHODOLOGY

A common approach used to solve aerothermal issues is based on combining analysis with experimentation. It is imperative that analytical techniques be used to plan the test and to analyze the final data. The two fundamental phases in the development process are:

1. defining the flight thermal environment
2. demonstrating hardware survivability
   [the first phase of this process was discussed in the preceding section]

The steps and approach in accomplishing this second phase are illustrated in Fig. 2. The general approach is to use analysis tools to design "smart tests" that simulate the flight environment, and then to expose flight components to this environment in ground test facilities. Material selection is perhaps the most difficult and the most important step. Determining thermo-physical properties and

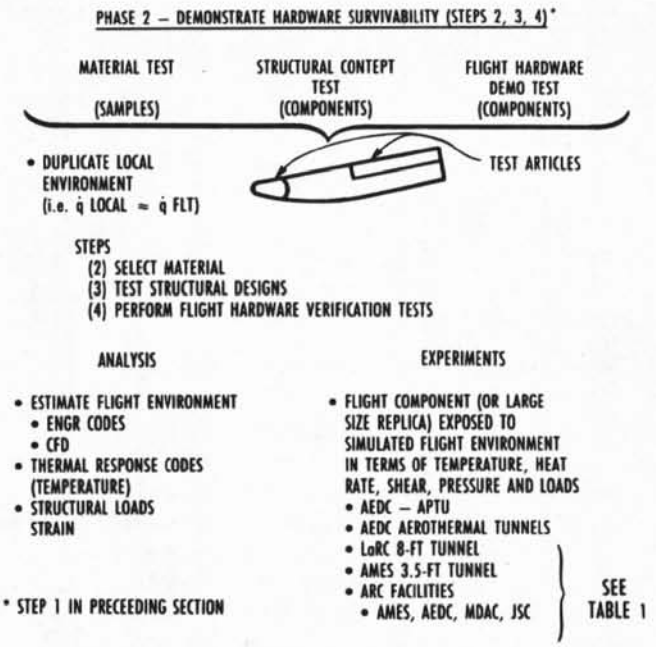

Figure 2. Methodology for aerothermal structures/materials development.

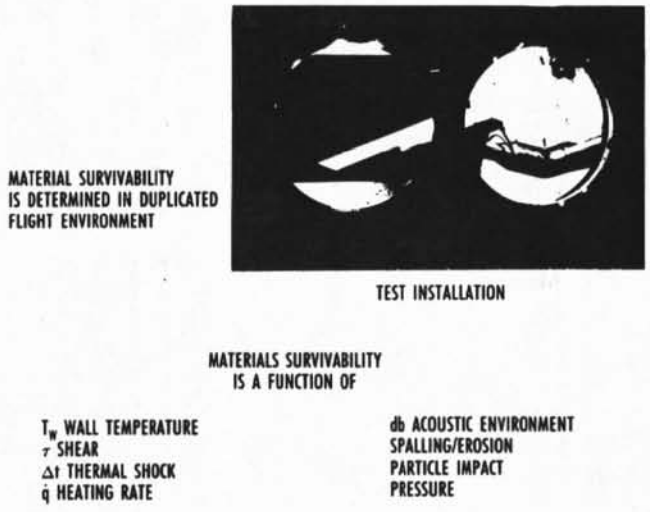

Figure 3. Materials testing in wind tunnels.

characterization of materials requires many hours of laboratory experiments. Despite these efforts, it is often difficult to predict material failure modes in a flight environment. Material survivability (Fig. 3) can be a function of many variables. Wind tunnels and arc-heated facilities often use the wedge testing techniques[1] to produce local flow environments that simulate flight. The primary test results are test article appearance after the run (i.e., survivability). An illustration of the wedge test technique is shown

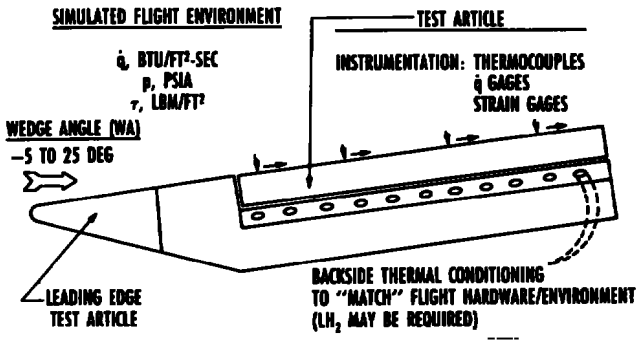

Figure 4. The wedge technique for aerothermal structures/materials testing.

in Fig. 4. The simulated flight environment may be primarily characterized by heating rate ($\dot{q}$), wall temperature (T_W), local surface pressure (p), and shear (τ). To produce this environment and to provide changes in the parameters, it may be necessary to pitch the wedge (e.g., –5 to 25 deg); of course, run time (or exposure time) is also a key test variable.

The test article may range from a simple insulated material panel to a complex structure with LH_2 cooling passages. In addition, it may be necessary to provide structural loading on the test article using hydraulic actuators mounted under the wedge. If the test article incorporates backside cooling, it is important to simulate both the aeroheating ($\dot{q}_{in}$) and the heat removed by the coolant ($\dot{q}_{out}$). Therefore, the mass flow, heat capacity, temperature, and viscosity of the coolant must be duplicated in the ground test.

In general, materials/structures testing can be grouped into the four categories listed in Fig. 5. Screening tests make relative comparisons among many candidate test articles in a constant (or repeatable) test environment. It is desirable to fabricate several identical test articles to investigate the repeatability of failure modes.

Characterization tests are the inverse of screening tests in that one test article design is exposed to a variety of test conditions. For example, the test variables may be temperature and load, and each is held constant while the other is varied over the range of interest. The data can be developed into an algorithm that characterizes the test article.

Component survivability tests basically answer the question "Will component X survive environment Y?" The disadvantage of this type test is that no quantitative data are produced for "other" flight conditions.

Component thermal response tests consist of a fully instrumented test article exposed to a wide variety of conditions so that a relatively sophisticated math model can be developed. The math model can be used to predict internal component temperatures for a variety of flight profiles. The disadvantage of this technique is that it is only valid for the specific component that is used to generate the database. If the component design changes after the test, it may be necessary to rerun the entire test for the new design. Examples of these test techniques are discussed below.

	ADVANTAGES	DISADVANTAGES
• SCREENING TEST	RELATIVELY SIMPLE, MANY TEST ARTICLES RUN IN SHORT TIME	ONLY RELATIVE RANKING BETWEEN TEST ARTICLES
• CHARACTERIZATION	ALLOWS EVALUATION AT SELECTED FLIGHT CONDITIONS	REQUIRES TESTING OVER A RANGE OF SEVERAL PARAMETERS, $\dot{q}$, T_W, SHEAR
• COMPONENT SURVIVABILITY	PROVIDES 'YES' OR 'NO' ANSWER FOR SIMULATED FLIGHT CONDITION	NO QUANTITATIVE DATA FOR 'OTHER' FLIGHT CONDITIONS
• COMPONENT THERMAL RESPONSE	CAN PROVIDE TEMPERATURES FOR A VARIETY OF SIMULATED FLIGHT CONDITION	DATA ONLY VALID FOR SPECIFIC COMPONENT TESTED

Figure 5. Types of aerothermal structures/materials test techniques.

Illustrative Examples

A materials screening test was conducted on high-temperature polymeric and Boron-Aluminum composite material specimens in AEDC Hypersonic Wind Tunnel (C), which is a continuous-flow, Mach 10 wind tunnel. Test specimens were attached to a wedge model adapted to serve as a specimen holder. The use of a large wedge as a holder for material samples creates the two test regions illustrated in Fig. 6. Region I is limited in height by the distance of the bow shock above the wedge boundary layer at the aft end of the wedge. This distance is about 10.9 cm (4.3 in.) for the 105.4 cm (41.5-in.)-long wedge used in this test. Region I provided relatively uniform flow for testing the curved surface samples that were

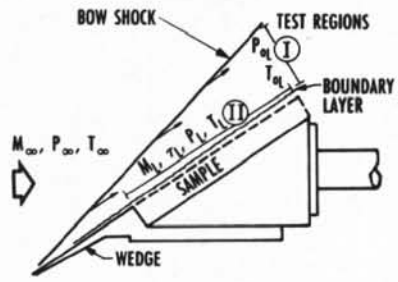

Figure 6. Sketch illustrating wedge flow-field nomenclature.

exposed to direct impact of the local flow (see Fig. 7). Much larger samples can be tested in Region II. (In fact, samples up to 63.5 cm (25 in.) long have been used.) In Region II, duplication of local shear stress, τ_L, is probably the most relevant parameter for the given total temperature level, T_o, whereas in Region I, duplication of total pressure, P_{oL}, total temperature, T_{oL}, and Mach number is of primary interest. The desired flow conditions on the material sample were produced by adjusting the wedge angle. The oblique shock wave generated by the wedge was used to reduce the local Mach number on the wedge surface to the desired supersonic level ($M \approx 4$). The tunnel stagnation conditions were adjusted to produce the desired local pressure and temperature levels. The fact that the Tunnel C clean air heater can provide temperatures up to 982°C (1,800°F) is the primary reason why this facility can be used for this type of testing. The test specimens consisted of 51 material samples: 39 curved configurations of several radii and thicknesses, and 12 flat panels. A sketch illustrating how the samples were installed on the wedge is presented in Fig. 7.

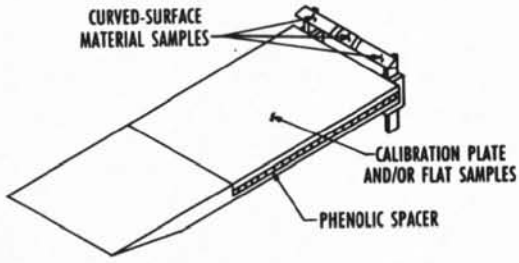

Figure 7. Sketch of material support techniques.

Typical photographs showing the effect of the simulated Mach 4 environment on the curved panels are presented in Fig. 8. All but one of the samples were glowing red-hot in the relatively short exposure times of 12 to 20 sec. This sample was the best conductor; as a result, heat was conducted away

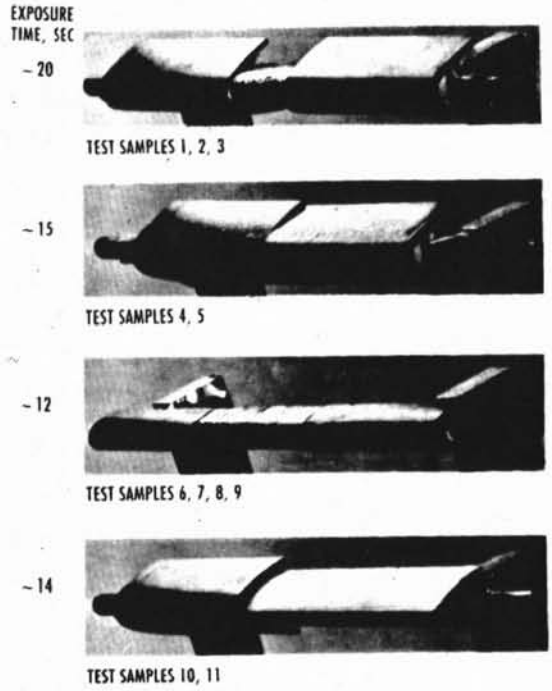

Figure 8. Photographs of curved-surface specimens during run.

from the leading edge. The other types of materials were relatively good thermal insulators; as a result, the surface temperature rise was very rapid. The data from this type test provide the necessary information to select the best material for survival in the simulated flight environment.

The second example of materials testing is the characterization of recession in a high-enthalpy facility. Thermal protection of hypervelocity flight vehicles is often accomplished by using materials that ablate during exposure to the severe environment. The outer surface ablates away while the inner surface remains relatively cool. The ideal material would allow no heat to penetrate to the inside surface, be very lightweight, and ablate very slowly. The ablation rate, or "recession rate," is a critical parameter in the selection of materials that can survive exposure to the high-enthalpy flow environment of hypersonic flight vehicles.

The Recession Rate Monitor (Fig. 9) operates on a triangulation principle (Fig. 10) where a focused laser beam is projected at a given angle onto a receding surface. When viewed from another angle, the laser spot shifts in the field of view in an amount proportional to the surface recession. The measured

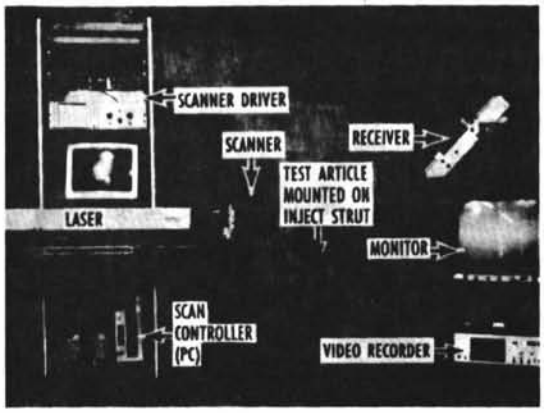

Figure 9. Recession rate monitor system.

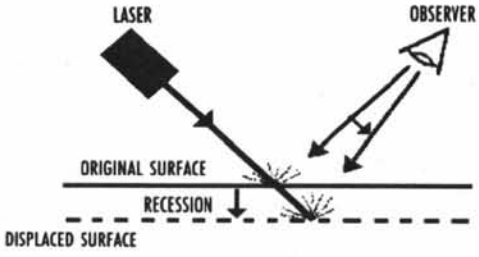

Figure 10. Recession rate monitor operating principal.

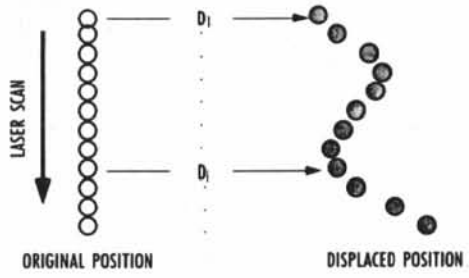

Figure 11. Profile measurement technique.

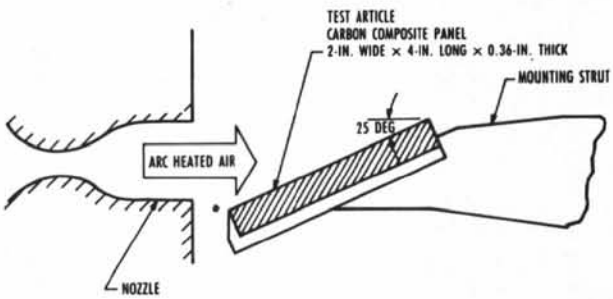

Figure 12. Test article installation.

shift, multiplied by the calibration constant, yields an accurate recession measurement at that point. To produce profiles, the laser beam is rapidly scanned across the surface, providing recession data from many points (or a continuum of points) along the scanned line (Fig. 11).

The Recession Rate Monitor has been used in AEDC's HEAT-H1 facility,[2] which uses a segmented type arc heater. High-pressure air is heated by means of an sustained arc plasma. The heated air is accelerated through a water-cooled nozzle to produce a free-jet test environment.

A representative test article installed in this facility is shown in Fig. 12. Axial centerline surface pressures ranged from 1.5 to 12 atm, and cold wall heat flux ranged from about 500 to 2,700 w/cm^2 sec or (Btu/ft^2-sec). The test articles were carbon composite panels 5 × 10 × 0.9 cm (2- × 4- × 0.36-in.) thick. For each test run, five test articles were mounted on the radial inject struts of a rotating sector. During a run, the test articles were sequentially subjected to the free-jet flow for about 3 sec each.

Recession data for one of the test articles are shown in Fig. 13. This figure can be viewed as a centerline cross-section of the test article (greatly exaggerated thickness) with the upstream end to the left and the exposed surface up. The "pretest surface" line identifies the location of the pretest material surface before ablation. The remainder of the solid line curves in the figure represent the surface profile obtained by the Recession Rate Monitor at the corresponding times. The surface profile defined by the circles was obtained from a posttest measurement of the surface made with a contact-type measurement device. The lowest of the family of solid line curves in the figure represents the profile acquired by the Recession Rate Monitor just before the test article was rotated out of the flow. Comparison of this curve with the post-test measurements indicates an agreement of within ±0.013 cm (0.005 in.). This excellent agreement demonstrates the quality of measurements obtainable with the Recession Rate Monitor[3] and demonstrates the characterization of the recession rate of an ablation test sample.

The third category of material/structure testing is "Component Survivability," and an example of this test technique is presented in Figs. 14 and 15. In the specific example the thickness of the shuttle tank insulation material was the primary area of concern. This material is a low-density Spary On Foam Insulation (SOFI) whose material properties (ρ, c, k) are known.

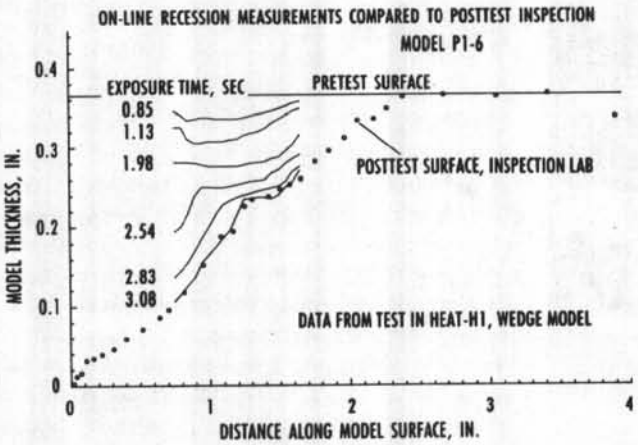

Figure 13. Characterization of material recession rate.

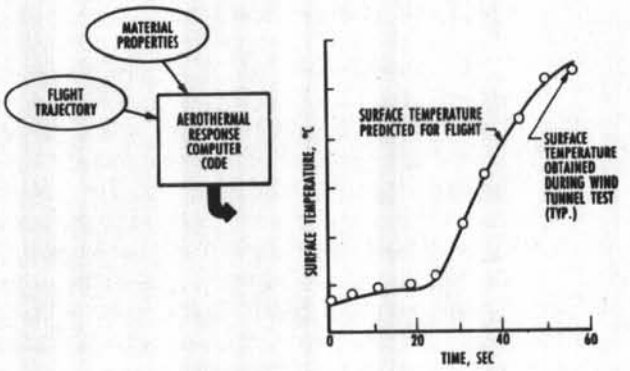

Figure 14. Flight trajectory thermal response simulation.

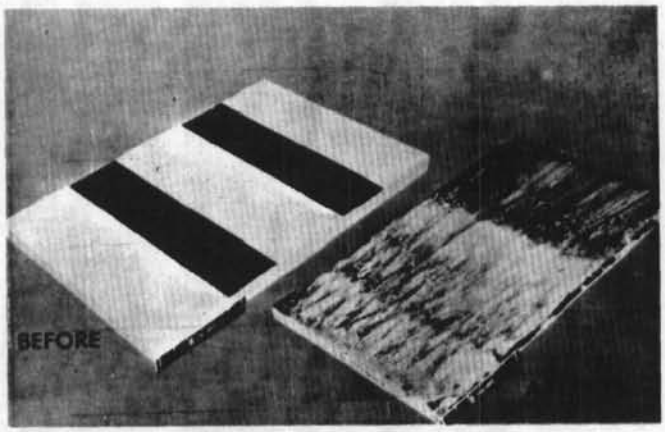

Figure 15. Shuttle external tank insulation material test.

The use of analysis tools to design a test is illustrated in Fig. 14. An "aerothermal response code" combines the material properties, the flight trajectory, and other inputs with a heat conduction model of the test article to provide a prediction of surface temperature versus time. A similar code combines the results of the wedge calibration data (i.e., $\dot{q}$ versus WA*) and the facility flow conditions to produce the test article surface temperature predictions during the wind tunnel test. In this manner, the wedge angle can be adjusted until the temperatures agree as shown in the figure. For the test article to reach the predicted temperature and temperature gradients, run times of many minutes may be required. Consequently, impulse facilities cannot be used for this type of testing.

The primary data from this type of test are the appearance of the test sample after exposure to the simulated flight environment. As shown in Fig. 15 the SOFI did survive the test; however, it did experience some recession, as was expected.

The fourth type of material/structure test technique (thermal response) is far more complex than those previously described, and only a few of this type have been conducted. Therefore, a similar discussion will not be presented, however, Ref. 4 is an excellent example of this category for those who are interested.

WEATHER/EROSION TESTING

The requirement for all-weather flight capability emphasizes the need for testing techniques that evaluate particle impact effects on vehicles operating at supersonic through hypersonic speeds in particle-laden environments. In particular, the effects of raindrops or other particles on radomes, heatshield materials, and antenna window materials need to be evaluated over a wide range of flight

* WA ~ Wedge Angle

speeds. The flight speed regimes and the corresponding test facilities are divided into the three classes listed below

Impact Velocities, ft/sec (km/sec)	Facility
1,000-3,000 (0.3-0.9)	Wind Tunnels/Sleds
3,000-6,000 (0.9-1.8)	Arc-Facilities
6,000-20,000 (1.8-0.6)	Aeroballistic Ranges

Each of these regimes is briefly discussed below.

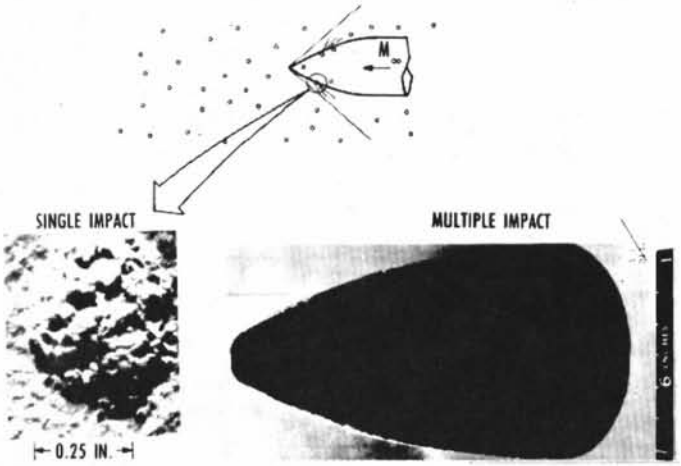

Figure 16. Missile radome in flight encountering rain/ice environment.

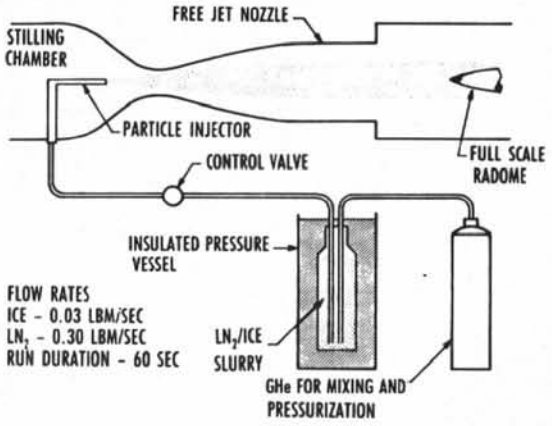

Figure 17. Aerodynamic particle erosion test technique.

Impact Velocity 1,000-3000 ft/sec (0.3-0.9 m/sec)

The erosion caused by a single water drop impacting a radome is shown on the left side of Fig. 16. The right side of the figure shows the erosion that can result from multiple impacts. It is clear that flight through weather can cause significant damage; however, it must be emphasized that the damage is a strong function of the radome material, vehicle speed, number of impacts, and the particle mass. Historically, weather erosion tests of material samples (coupons) and of full-size radomes have been conducted at sled tracks equipped with rain simulation apparatus. In the U.S. the Holloman sled track[5] is perhaps the best known of these facilities. In recent years, a new long-duration, multiple impact capability has been developed[6] utilizing Tunnel C at AEDC. The basic principles of this new capability are illustrated in Fig. 17. The initial development of a precipitation environment simulation in a wind tunnel considered the injection of ice particles or water droplets into the tunnel airflow. Analytical studies indicated this approach to be impractical for water droplets, since high shear forces would cause disintegration of the droplets. The technique to inject ice particles was derived from an injection method proposed by Allen.[7] The ice particles are suspended in a liquid-nitrogen carrier and injected into the tunnel flow upstream of the supersonic nozzle. As the flow field expands through the nozzle, the carrier flashes to a gaseous state, which causes very little effect on the flow constituents. During laboratory checkout of the injection system, 500-μ ice particles were discharged at rates of up to 5×10^5 particles per sec for durations up to 60 sec.

The Mach 4 Aerothermal Wind Tunnel (C) used in the development of the precipitation environment is a closed-circuit, high-temperature, supersonic free-jet wind tunnel with an axisymmetric contoured nozzle and a 0.63 m (25-in.)-diam exit. The tunnel operates continuously over a range of pressures from 15 psia to a maximum of 180 psia (1-12 bar) and at maximum stagnation temperatures up to 1,900°R (1,050°K). The test unit utilizes a model injection system which allows the test article to be withdrawn from the test section while the free-jet tunnel remains in operation. The test specimen is mounted on a sting support mechanism in an installation tank directly underneath the tunnel test section and is then injected into the particulate flow. Data are obtained with a pulsed holography system, the LDV, and the photographic systems (Fig. 18) in addition to the standard tunnel system during the exposure process. At a selected time, the test article is retracted into the tank, the particle injection system control valve is closed,

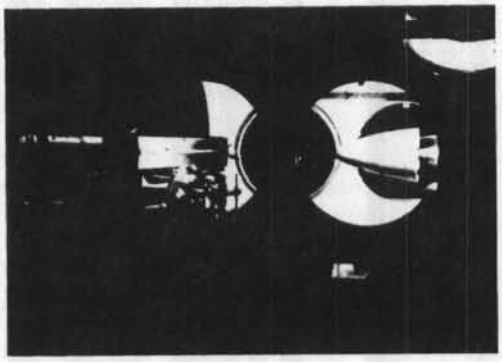

Figure 18. Wind tunnel test section area.

and the system depressurized in preparation for the next exposure. The laser diagnostic systems provide particulate cloud characteristics during the run. Ice particles of a size and concentration representative of a precipitation environment are injected into the airstream and accelerated by aerodynamic drag to supersonic velocities. Characteristics of a particulate cloud before its impact with the test article are determined with laser diagnostic systems. A vehicle operating in a flight regime below 50,000 ft (15 km) may encounter a precipitation environment of 100- to 3,000-μ (0.1- to 3.0-mm) ice particles or water droplets falling at rates up to 2.6 in./hr (66 mm/hr).

Figure 19 illustrates a typical hologram obtained during an exposure run showing the two images of a particle from the double-exposure technique. These photographs quantify both the size and geometry of the particles, as well as the particle velocity. The velocity data from these holograms agree to within 10 percent of pretest predictions obtained from a one-dimensional particle acceleration code. Figure 20 shows a demonstration test radome located on flow centerline approximately 6 in. downstream of the laser diagnostics systems during a precipitation environment exposure. This full-scale flight hardware was exposed to the precipitation environment for 20 sec and, as can be seen approximately half of the RTV material was eroded away while the other side (candidate material) survived the multiple impact environment. A point that should be noted is the use of ice particles to represent water droplets in the precipitation environment. Although ice particles make up a major portion of the flight environment of interest, a portion of the environment exists where a simulation of rain droplet impacts would be required. AEDC has conducted a brief study to determine the correlation between ice and water impacts at about 762 m/sec (2,500 ft/sec). For the limited data obtained, there was negligible difference between the ice and water impact craters; however, this conclusion cannot be generalized for all materials of interest, and each situation needs to be evaluated.

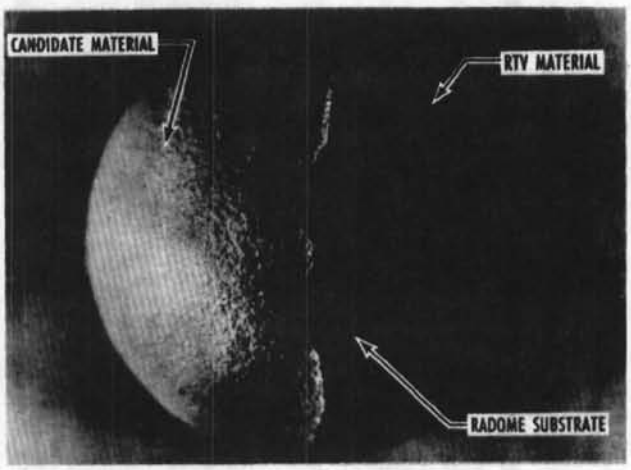

Figure 20. Radome following 20-sec exposure to multiple impacts.

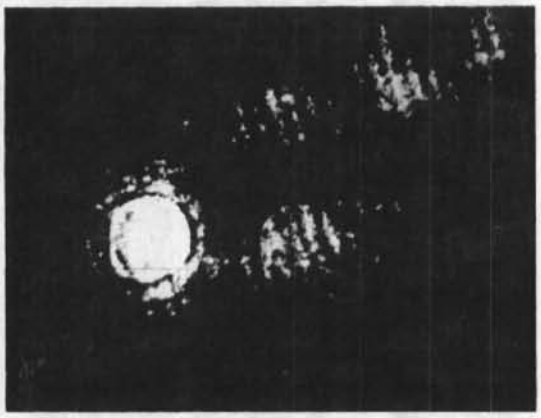

Figure 19. Double-pulsed hologram of 500μ particle.

Impact Velocity 3,000-6,000 ft/sec

The AEDC HEAT-H1 Test Unit has the capability of graphite particle injection and acceleration for combined ablation/erosion testing. This capability is achieved by injecting various size graphite particles (60-400 μm) into a chamber just upstream of the nozzle and allowing them to drag-accelerate to velocities between 3,000 and 6,000 ft/sec (0.9-1.8 km/sec). A schematic of the erosion testing technique used in HEAT-H1 is given in Fig. 21. Dust particle flow rates from 5 to 60 gm/sec can be provided, and development work is underway to reduce flow rates below the 5 gm/sec rate. The cylindrical nozzle

extensions shown in Fig. 21 are added to the HEAT-H1 contoured nozzles to provide a longer transit time for the particles to accelerate. A Mach number 3.5 nozzle has been used extensively for dust erosion tests, and a Mach number 2.2 nozzle is also available. Calculated velocities for a range of particle diameters of interest are shown in Fig. 21 with the 30-in.-long dust accelerator installed. Laser diagnostic systems similar to those previously mentioned are available to characterize the particle cloud. Representative sample sizes are 1.9 cm (0.75 in.) wide, 5.1 cm (2 in.) long, and dovetail fitted into a surrounding silica phenolic heatshield material, which in turn was dovetailed into the stainless steel holder. Wedge model/holder hardware and a typical test installation photo is shown in Fig. 22. The primary "data" from this type test are obtained by close inspection of the sample before and after exposure to the erosion environment (see Fig. 22).

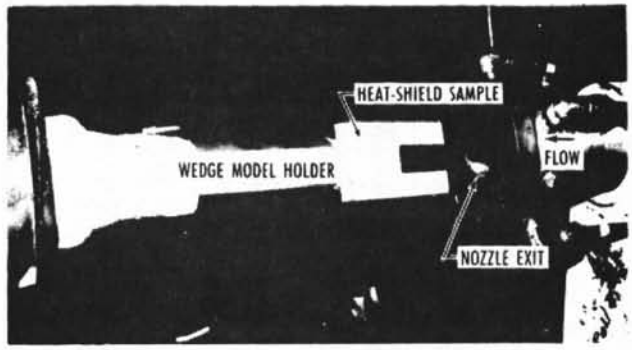

a. Pre-test photograph.

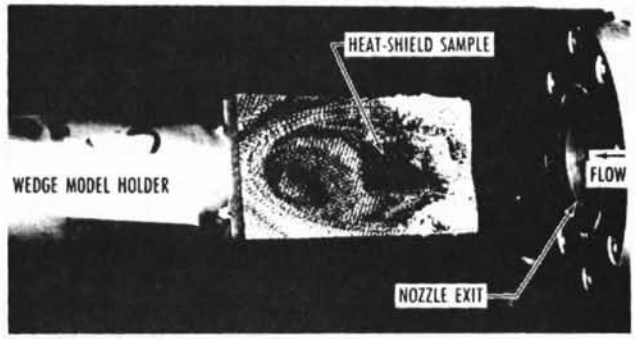

b. Posttest photograph.

Figure 22. Arc heater erosion test mounted on twenty-five-deg wedge sample.

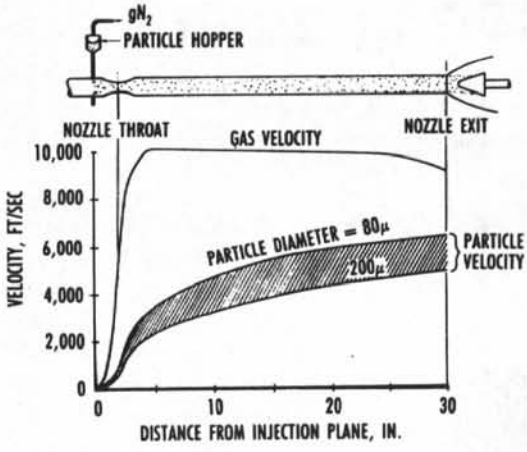

Figure 21. Dust erosion testing in the arc-heated facilities.

Impact velocities 6,000-20,000 ft/sec

For these extremely high velocities, the primary facility with this capability is the AEDC Hypervelocity Range/Track G. This ballistic range has the capability to test in the normal free flight ballistic range mode or to utilizes a track system to guide a model through the test environment.

The basic ablation/erosion test technique in Track G is to launch the nosetip or heat shield material samples through a specified erosive environment at a given range pressure and model velocity. The erosive environment is specified in terms of particle type, particle size, and field concentration. Glass spheres (simulating dustfield environments), cirrus ice particles and dendritic snow flakes have been routinely used. The range pressure and model velocity are independently controlled to duplicate a point of interest on a reentry trajectory.

The typical snowfield generator installation for the free-flight mode of testing is shown in Fig. 23. These snowfield generators are typically mounted 0.61 m (2 ft) above the centerline at selected intervals along the range axis. The plates are vertical, but oriented at 45 deg to the longitudinal axis of the range to accommodate side-mounted cameras which photograph the falling snow. The snowflakes are dislodged from the copper plate by a mechanical shock device (solenoid plunger) at the desired time, and produce a free-falling erosion field which can be varied in field length and concentration. A similar approach for generating the snow particles is used in the track mode of testing.

The generated snowflakes that are formed when the crystals are dislodged are shown in Fig. 24.

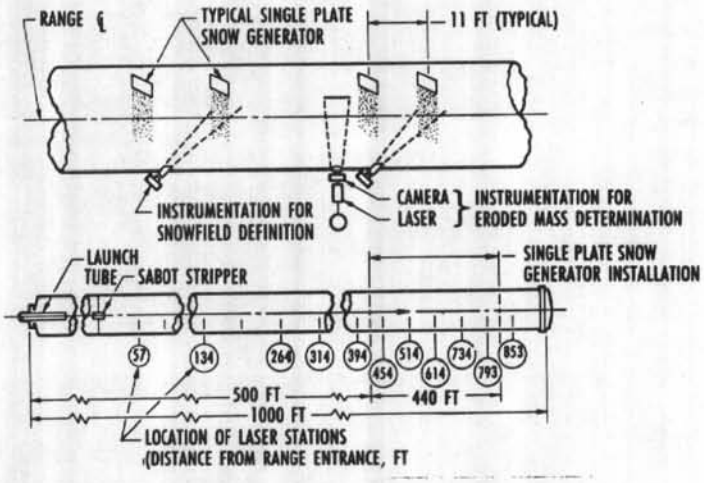

Figure 23. Snowfield generator installation in AEDC Range G.

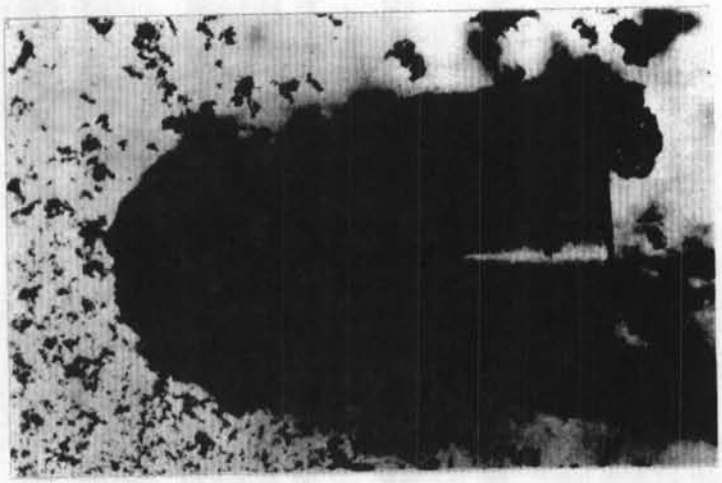

Figure 24. Model-snowfield encounter at 12,000 ft/sec.

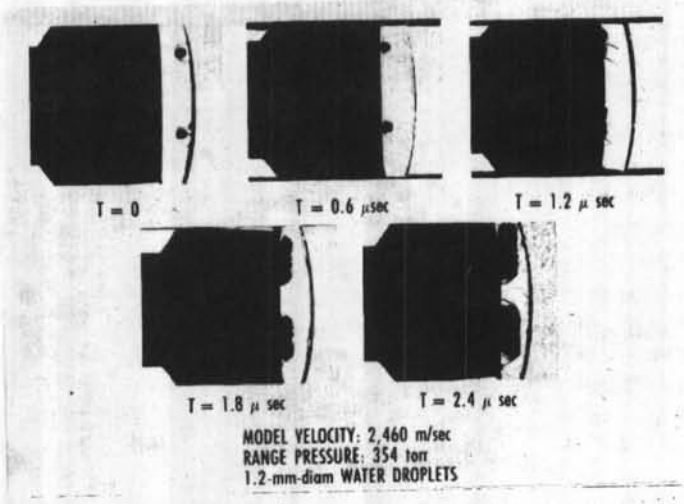

Figure 25. Model/water two droplet impact sequence.

Snowfield concentration is controlled by regulating crystal growth time and filtering the falling snowflakes through perforated plates. Since the falling snow stratifies with larger flakes near the head of the fall and smaller ones near the tail, the impacted flake size can be controlled within the limits of model dispersion by appropriate timing of model arrival. This model-snowfield encounter at 12,000 ft/sec was obtained by utilizing a high speed multi-frame camera with a framing rate on the order of a million frames per second.

A water droplet impact sequence onto a track guided model shows (Fig. 25) that the water droplet remains intact in passing through the bow shock. But it is also important to recognize the extremely short time-frame of this event (i.e., $\approx 0.6\ \mu$sec). It is interesting to note the quantity of debris and additional shock waves being placed into the flow field by the impact debris plume.

SUMMARY

A summary of the systems, test articles, and type of test needed for the development of structural/material components for hypersonic vehicles is presented in Fig. 26. It is important to point out that this summary is limited to the topics briefly discussed in this section, and that this subject is much broader in that only "flow facilities" were discussed. There are, of course, numerous non-flow facility tests that are an essential aspect of structure/material development.

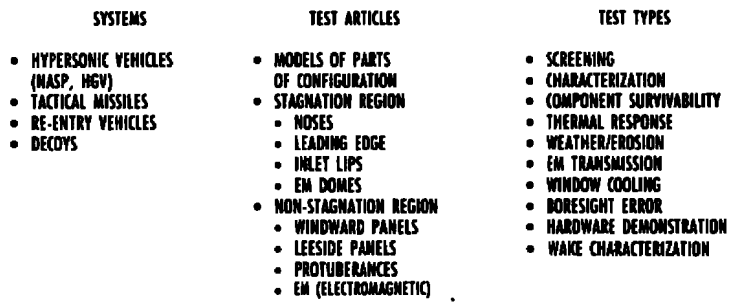

Figure 26. Summary of hypersonic aerothermal tests for the development of structural/material components.

Table 1. Aerothermal test facilities.

OWNER	FACILITY NAME	NOZZLE MACH NUMBER	SIZE, IN. (2.54 cm/in.)	STAGNATION PRESSURE, ATM	STAGNATION ENTHALPY, BTU/LBM	FLOW RATE, LBM/SEC	POWER, MW
NASA-JOHNSON SPACE CENTER HOUSTON TX 77058	ARMSEAP TP-1	3-12	10 to 40 DIAM				10
	ARMSEP TP-2	3-6	5		26,000		5
NASA-LANGLEY RESEARCH CENTER, HAMPTON VA 23365	5 MW TUNNEL	3.0, 3.2	6, 9 DIAM	0.02-0.4	200-3,000		5
	COMBUSTION-HEATED SCRAMJET TEST FACILITY	3.5	13.26 × 13.26	3-12	300-550	16-60	N/A
	20 MW TUNNEL	4.2, 4.5, 5.0, 5.7	9, 12, 16, 22 DIAM	0.04-1 36	600-5,500		20
	ARC-HEATED SCRAMJET TEST FACILITY	4.7, 6.0	11 high, 11 long	40	1,500	14	20
	8 FT HIGH TEMPERATURE TUNNEL	5.8-7.3	8.0 DIAM	163	750		N/A
ARNOLD ENGINEERING DEVELOPMENT CENTER, ARNOLD AFB, TN 37389-5000	HYPERSONIC WIND TUNNEL TUNNEL, C	4, 10, 8	25 AND 50 DIAM	136	450	50	50
	HEAT-H2	4.0-8.3	9 TO 42	UP TO 100	1,200-3,010	2-10	42
	HIGH ENTHALPY ABLATION TEST UNIT (HEAT) HR	1 8-3.1	11-4.0 IN. DIAM	100	2,000	2-10	42
	HIGH ENTHALPY ABLATION TEST UNIT (HEAT) H1	1 8 to 3.5	75 to 3 IN. DIAM	120	500-1,000	0.5-8	30
	AERODYNAMICS AND PROPULSION TEST UNIT (APTU)	2.0, 2.2, 2.55, 2.72, 3.5, 4.1	32-38 DIAM	20			N/A
	RANGE/TRACK G	1-22 (MODEL)	2.5 DIAM	0-500	8,000	N/A	N/A

Table 1. Concluded.

OWNER	FACILITY NAME	NOZZLE MACH NUMBER	NOZZLE SIZE, IN.	STAGNATION PRESSURE, PSIA	STAGNATION ENTHALPY, BTU/LBM	FLOW RATE, LBM/SEC	POWER, MW
MARTIN MARIETTA CORP P. O. BOX 5837 ORLANDO FL 32855	CONTROLLED FLOW (CONFLOW) COMBUSTION FACILITY	1.5, 2 4, 3.2	3 5-26 DIAM	30-200		200-220	N/A
MCDONNELL DOUGLAS CORP P. O. BOX 516 ST LOUIS MO 63166	LARGE CORE ARC TUNNEL (LCAT) FACILITY		0.9-24.0 DIAM	0.1-100	1,000-20,000		10
	HIGH IMPACT PRESSURE (HIP)	1.7-3 0	0.45-2.0 DIAM	10-250	1,000-8,500	0 07-3 3	12
NASA-AMES RESEARCH CENTER MOFFETT FIELD CA 94035	HIGH ENTHALPY ENTRY FACILITY	1.7	4 DIAM		100,000		120
	2 × 9-IN. TURBULENT FLOW FACILITY	3.5	2 × 9	20	4,000		20
	GIANT PLANET FACILITY	1.7	2.75 DIAM	10	40,000-100,000	0.1-0.5	75
	20 MW PANEL TEST FACILITY	5.5	4 × 18 SEMIELLIPTIC	10	4,000-15,000	0.1-2.0	20
	60 MW INTERACTION HEATING FACILITY	5.5, 7.5	8 × 32 & 36 DIAM		3,000-20,000		60
	TRANSITIONAL FLOW FACILITY	1.7 AND 2.8	2.3-7.0 DIAM	10	3,000	20-40	100
	AERODYNAMIC HEATING FACILITY	2.5-12	3-42 DIAM	10	500-14,000	5	20
	3.5 FT HYPERSONIC	5, 7, 10	3.5 DIAM	133			N/A

REFERENCES

1. Matthews, R. K. and Stallings, D. W. "Materials Testing in the VKF Continuous Flow Wind Tunnels." AIAA 9th Aerodynamic Testing Conference, Arlington, TX, June 7-9, 1976.

2. Horn, D. D. and Smith, R. T. "AEDC High-Enthalpy Ablation Test (HEAT) Facility Description, Development, and Calibration." AEDC-TR-81-10, July 1981.

3. Sherrouse, Peter and Carver, Dwayne. "Demonstrated Real-Time Recession Measurements of Flat Materials During Testing in High-Enthalpy Flows." AIAA-92-0765, 30th Aerospace Sciences Meeting & Exhibit, Reno, NV, January 6-9, 1992.

4. Wannenwetsch, G. D., Matthews, R. K. and Howanick, J. "Test Results and Prediction Techniques Used in the M505A3E2 Fuze Auto-Ignition Investigation." AIAA-81-1041, AIAA 16th Thermophysics Conference, Palo Alto, CA, June 23-25, 1991.

5. Staff, Holloman Air Force Base, "The High Speed Test Track Facilities and Capabilities." 6585th Test Group Test Track Division, Holloman Air Force Base, NM, April 1989.

6. Beitel, G. R. and Matthews, R. K. "A New Rain/Ice Test Capability to Simulate Flight." AIAA-86-9824, 3rd Flight Testing Conference, Las Vegas, NV, April 2-4, 1986.

7. Allen, R. M. "A Method of Accelerating Ice Particles to Hypersonic Velocities in the Laboratory." Boeing Report Number D180-18691-1, March 1975, Addendum October 1975.

BOUNDARY-LAYER TRANSITION

by
R. K. MATTHEWS
Senior Staff Engineer
Calspan Corporation/AEDC Operations
Arnold Engineering Development Center

ABSTRACT

In the design of hypersonic vehicles it is extremely important to predict the boundary-layer transition Reynolds number. The boundary-layer state (laminar or turbulent) that approaches the vehicle control surfaces can significantly affect the control surface effectiveness. In addition, the heating rates ($\dot{q}_w$) associated with turbulent boundary layers are often ten times higher than those of laminar boundary layers. Unfortunately, the methodology to predict transition has eluded the aerodynamicist for over three decades, and there are still many unanswered questions. This section briefly touches on the many parameters that affect transition and provides numerous references for those who are interested in specializing in this topic. It should be emphasized that during wind tunnel testing it is very important to know the boundary-layer state. Typically, heat-transfer distributions can provide this information; however, it is often necessary to artificially trip the flow to induce a turbulent boundary layer. The methodology of using trip spheres is discussed, and illustrative data are presented.

NOMENCLATURE

h	Heat-transfer coefficient
h_{ref}	Reference heat-transfer coefficient
k	Roughness (or trip) height
L	Length of model or vehicle
M	Mach number
p	Pressure
$\dot{q}_w$	Wall heating rate
Re	Reynolds number
$Re_{k,\,tr}$	Transition Reynolds number based on roughness height k
$Re_{x,\,t}$	Transition Reynolds number based on axial distance x
Re_{CF}	Cross flow Reynolds number
T	Local temperature
U	Velocity
v	Cross flow velocity component
x	Axial distance
$x_{t_{beg}}$	Axial distance to beginning of transition
$x_{t_{end}}$	Axial distance to end of transition
δ	Boundary-layer thickness
μ	Viscosity
ϱ	Density
τ_w	Wall shear stress

Subscripts

∞	Free stream
e	Edge condition

Superscript

~	Unsteady.

FUNDAMENTALS

Boundary-layer transition is a very complex and specialized subject, and to be truly knowledgeable in this speciality requires many, many years of dedicated work. In the U.S. two individuals who have done this are Morkovin[1-4] and K. F. Stetson[5-14]. Much of the material is this section has been taken directly from their work.

Figure 1 introduces the usual concept of boundary-layer transition as consisting of a region beginning at the termination of pure laminar flow ("transition onset" at $x_{t,\,beg}$) and ending at the beginning of turbulent flow ("transition completion" at $x_{t,end}$). The sketches below the figure show the qualitative variation of heat flux or surface shear in the laminar, transitional, and turbulent flow regions. The relatively sharp change in value of either of these parameters at the beginning of transition offers a method of detecting transition onset. The most common method in use today for detecting transition onset in either ground or flight testing is some form of heat flux or temperature measurement.

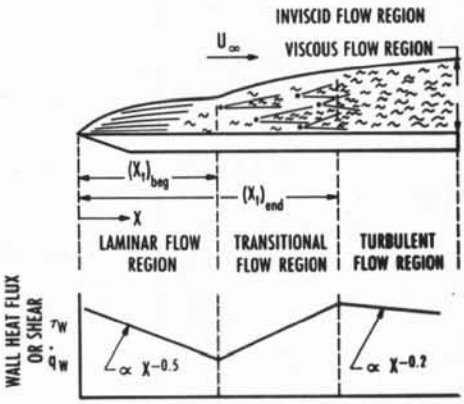

Figure 1. Boundary layer concepts, terminology, and measurement.

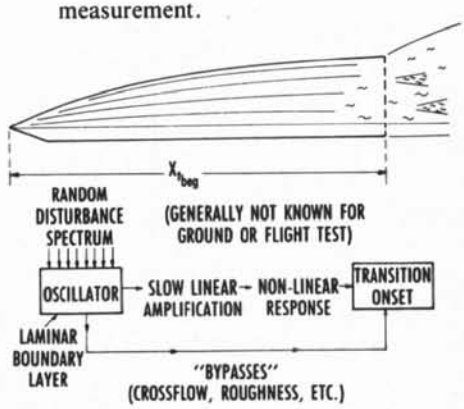

Figure 2. Current understanding of boundary layer transition.

Figure 2 is a simplified schematic representation of Reshotko's[15] concept of transition of the laminar boundary layer to a turbulent state as the "non-linear response of a very complicated oscillator (the laminar boundary layer) to a random forcing function whose spectrum is assumed to be of infinitesimal amplitude compared to the appropriate laminar flow quantities." Also shown are the "bypasses" discussed by Morkovin,[3] such as roughness, free-stream

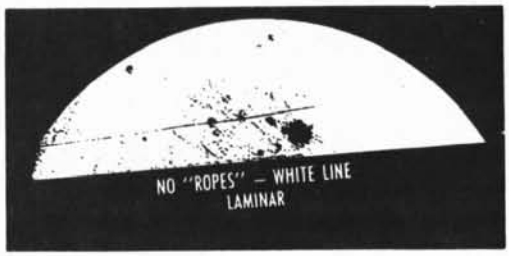

a. Laminar

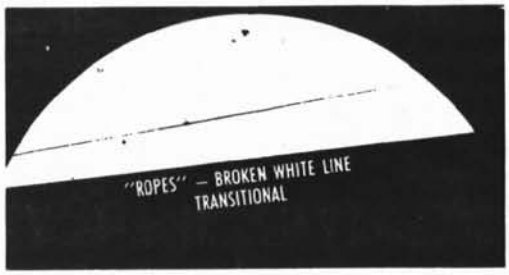

b. Transitional

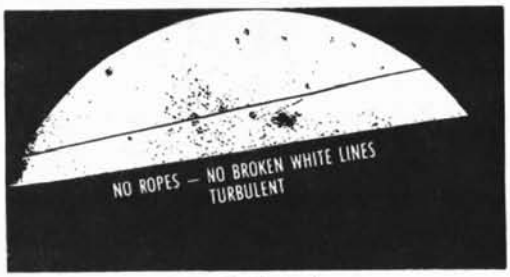

c. Turbulent

Figure 3. Photograhs obtained on a sharp 9 deg cone at M_∞ = 8 in AEDC tunnel B.

turbulence, etc., that cause transition to bypass the linear processes. The photographs of Fig. 3 show laminar (3a), transitional (3b), and turbulent (3c), boundary layers on a sharp 9-deg cone at Mach 8 in AEDC's Tunnel B. The laminar boundary layer is characterized by a white line which has a "roping" appearance in the transitional regime and eventually completely disappears in the fully turbulent regime.

A Specialist's View of Boundary-Layer Transition, presented in Fig. 4, represents Morkovin's 1984[4] update of an earlier chart which describes the laminar boundary layer as either a linear or nonlinear operator in its response to a random disturbance spectrum. It depicts a summary of the transition process based on several decades of research in theoretical and experimental studies of transition phenomena. A careful review of this figure and the 1969 treatise by Morkovin should help the transition student to develop an appreciation for the complexity of the transition process with its many competing "operation modifiers" and the race between instability modes.

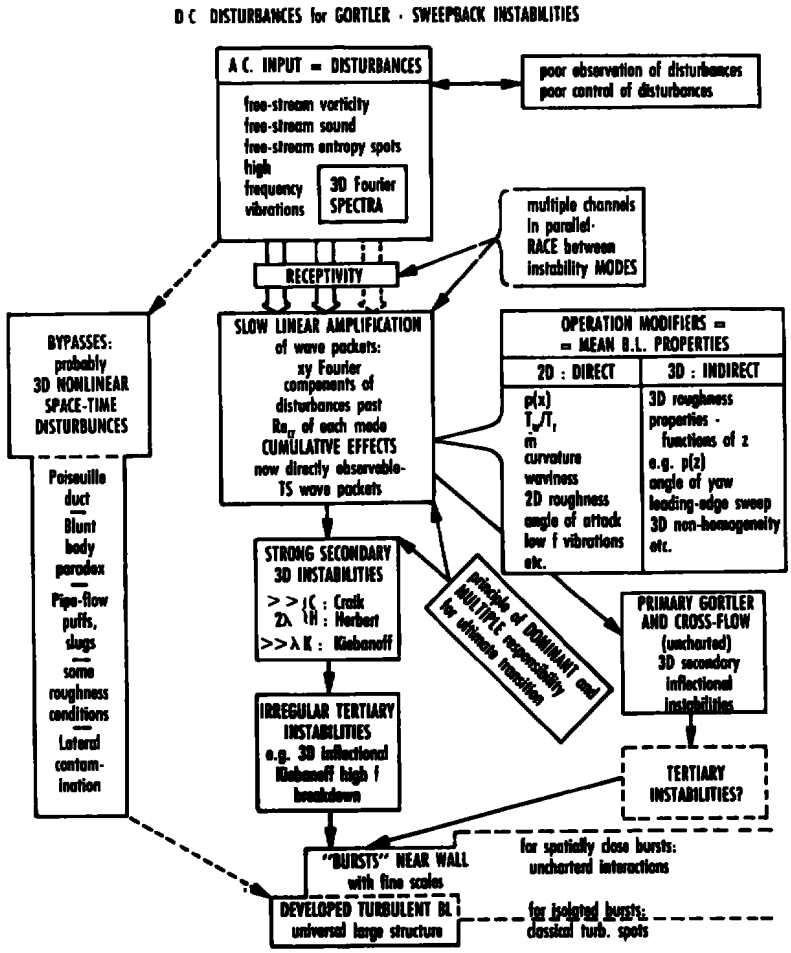

Figure 4. A specialist's view of boundary-layer transition.

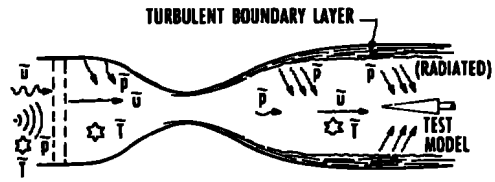

MACH NUMBER RANGE	TYPE DISTURBANCE	EFFECT ON TRANSITION
M_∞ = 1.5 TO 3	VORTICITY ($\tilde{u}$) (TURBULENCE)	– USUALLY DOMINANT
	NOISE ($\tilde{p}$)	– MAY BE DOMINANT
	ENTROPY ($\tilde{T}$) (TEMP. SPOTS)	– NEGLIGIBLE
M_∞ = 3 TO 15 (COLD FLOW)	RADIATED NOISE ($\tilde{p}$)	– USUALLY DOMINANT
M_∞ > 10 ARC TUNNELS SHOCK TUNNELS MHD TUNNELS	ENTROPY • ($\tilde{T}$)	– ?
	RADIATED NOISE ($\tilde{p}$)	– MAY BE DOMINANT

Figure 5. Flow disturbances in supersonic and hypersonic tunnels.

Figure 5 illustrates the disturbance sources present in wind tunnels, as identified by Kovasznay.[16] These disturbance modes were discussed by Morkovin,[1,2] who speculated on their origins in a supersonic wind tunnel. The vorticity and entropy fluctuations were traceable to conditions in the settling chamber, while sound disturbances could originate in the stilling chamber and from the test section boundaries. The turbulent boundary layer on the tunnel wall was identified by Morkovin as a potential source for radiated noise. Later research by Pate[17] has shown this to be the dominant factor in transition on wind tunnel models.

The comparison of a large collection of wind tunnel and flight transition data[18] on sharp cones over a wide range of Mach number and Reynolds number is presented in Fig. 6. The flight data are generally higher than the wind tunnel data correlation line, presumably due to large disturbance levels in the wind tunnels. It is noteworthy that the flight data exhibit a unit Reynolds number dependence.

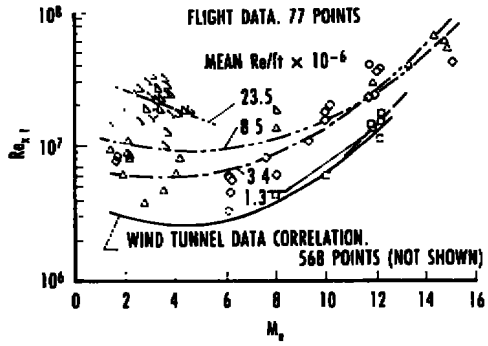

Figure 6. Comparison of wind tunnel and flight transition data on sharp cones.

As previously mentioned, boundary-layer transition is often detected from heat flux or temperature measurements, and a typical example is presented in Fig. 7. This figure shows shuttle temperature measurements during reentry of flight STS-2. Just after 1,000 sec, there was a significant rise in the flight temperature data which is typically presumed to be caused by the increased heating associated with turbulent flow. Note, that the predicted time of transition was at about 800 sec which corresponds to a significantly lower value of transition Reynolds number. This is just another example of the inability to predict the correct flight transition Reynolds number.

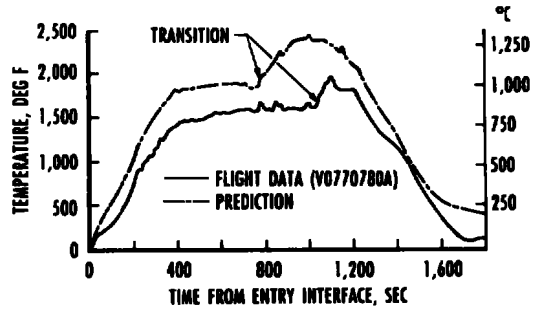

Figure 7. Control surface temperature comparison, STS-2.

Another comparison of wind tunnel and flight transition data from the shuttle is presented in Fig. 8. These transition data obtained during reentry (increasing Reynold number) were significantly influenced by disturbances caused by "surface roughness" in the form of the shuttle tiles. Transition Reynolds number based on tile height, $Re_{K,tr}$ shows that once transition occurred, it progressed quickly toward the shuttle nose for a relatively small change in Reynolds number. On the other hand the wind tunnel results (shaded area) predicted a more gradual forward progress of transition. This example is interpreted as an example of "effective tripping" by the roughness with high amplification rates that diminish differences in ground and flight results.

COMMENTS ON TRANSITION PREDICTION METHODOLOGY

It would be "nice" to be able to put forth a good, reliable method for predicting transition such that those people who have to make estimates of transition Reynolds numbers would know exactly how to proceed. Unfortunately, the problem is not that simple. The best that can be done is to provide some general guidelines and encouragement to make the most of the data that are currently available. Thus, the following are some comments on the methodology for hypersonic transition predictions (see Fig. 9).

STEP 1:	OBTAIN BACKGROUND INFORMATION
STEP 2	OBTAIN FLOW FIELD DATA
STEP 3	CONSIDER DOMINANT MECHANISMS
STEP 4	OBTAIN A BASE-LINE TRANSITION REYNOLDS NUMBER
STEP 5	BIAS THE TRANSITION RESULTS
STEP 6.	ESTIMATE UPPER AND LOWER BOUNDS
STEP 7:	A MIRACLE OCCURS AND YOU KNOW WHAT THE TRANSITION REYNOLDS NUMBER SHOULD BE

Figure 9. Transition prediction methodology.[19]

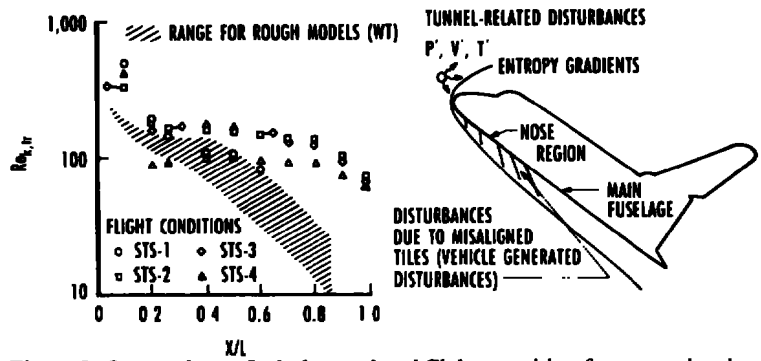

Figure 8. Comparison of wind tunnel and flight transition for space shuttle.

STEP 1: OBTAIN BACKGROUND INFORMATION

WATCH OUT FOR BYPASSES: Sometimes unexpected phenomena such as freestream turbulence or wall cooling effects can greatly reduce the expected transition Reynolds numbers.[15]

CONFIGURATION DIFFERENCES: Be aware of the influence of configuration differences on transition. The cone versus flat plate issue illustrates the problem. It had generally been assumed that one should obtain higher transition Reynolds numbers on cones than on flat plates, at least between Mach numbers 3 and 8. Experiments were performed in the NASA/Langley Research Center Mach 3.5 quiet tunnel to investigate this issue.[20,21] The ratios of cone-to-flat-plate transition Reynolds numbers were found to vary from about 0.8 for low-noise free-stream conditions to about 1.2 for higher noise conditions.

PROBLEMS OF WIND TUNNEL DATA: Conventional wind tunnels have large disturbances in their free-stream environments; thus, wind tunnel transition Reynolds numbers are generally lower than corresponding flight transition Reynolds numbers.

LENGTH OF THE TRANSITION REGION: It has been customary to assume that the length of the transition region is the same as the length of the laminar region.[22]

STEP 2: OBTAIN FLOW-FIELD DATA

Uncertainty in flow-field calculations directly influences the uncertainty in the transition estimates. Calculations of the boundary-layer properties are a very important part of the transition problem.[23] Close attention should be given to the flow-field properties.

STEP 3: CONSIDER DOMINANT MECHANISMS

NOSETIP: Because nosetip transition Reynolds numbers can be influenced by roughness they can be two orders of magnitude less than frustum transition length Reynolds numbers, it is necessary to consider nosetip transition independently from the rest of the configuration.[24]

EARLY FRUSTUM: Early frustum is defined as the region just downstream of the nosetip, extending for several nose radii. The transition experiments reported in Ref. 11 clearly identified the early cone frustum as a region with its own transition criteria.

CROSSFLOWS: The laminar boundary-layer profile in a three-dimensional, viscous flow has a twisted profile that can be resolved into tangential (u) and crossflow (v) velocity components. The crossflow component of the velocity is used for the computation of crossflow Reynolds number. If the boundary-layer thickness is used as the length dimension, for a value of $Re_{CF} = 200$ it could be expected that crossflow instabilities would dominate and cause transition.[25,26]

$$Re_{CF} = \frac{\varrho v_{max} \delta}{\mu}$$

LEADING EDGE CONTAMINATION: If the beginning of the leading edge of a swept wing is in contact with a solid surface (e.g., a fuselage or a wind tunnel wall), the turbulence which is present in the boundary layer of the adjoining surface will contaminate the leading edge boundary of the swept wing. Such turbulence contamination has a significant effect on the state of the leading edge boundary layer and can dominate the transition process on the wing.[27]

GORTLER INSTABILITIES/ADVERSE PRESSURE GRADIENTS: There is insufficient data available to establish a general criterion to determine when adverse pressure gradient effects and Gortler instabilities will dominate and produce an early transition.

Linear stability theory (the e^N method Refs. 28 and 29) has been used to predict the effects of Gortler instabilities on transition of boundary layers on wind tunnel nozzle walls.

STEP 4: OBTAIN A BASELINE TRANSITION REYNOLDS NUMBER

Baseline transition Reynolds number can be obtained from a collection of transition data (such as Fig. 6) or by correlation techniques. Remember that flight data such as contained in Fig. 6 already contains effects such as small nosetip bluntness, small angles-of-attack, and some wall temperature variations.

STEP 5: BIAS THE TRANSITION RESULTS

If there are several parameters which are expected to have a significant effect on transition, but no single effect is clearly dominant, then some accounting for the individual effects should be made. If a baseline transition Reynolds number is obtained, make adjustments to this number to account for the other parameter effects which are expected to be significant. Most of the parametric trends come from wind tunnel data since wind tunnel experiments can be better controlled than flight experiments.

STEP 6: ESTIMATE UPPER AND LOWER BOUNDS

All transition estimates will have an uncertainty associated with them, and obviously it is important to consider this uncertainty when predicting transition location.

STEP 7: A MIRACLE OCCURS AND YOU KNOW WHAT THE TRANSITION REYNOLDS NUMBER SHOULD BE

BOUNDARY-LAYER TRIPS (An Engineering Approach, Fig. 10)

The preceding discussion showed that wind tunnel transition data could not be depended upon to predict transition in flight. However, a typical vehicle will experience either a laminar or turbulent boundary layer for a significant part of its mission profile, and wind tunnel tests can be designed to produce data on models with predominantly laminar or turbulent boundary layers. It is very important to **know** the boundary-layer state and surface heat transfer measurements are routinely used for this purpose (e.g., Ref. 26).

- CAN'T DEPEND ON GROUND TEST FACILITIES FOR PREDICTING FLIGHT TRANSITION REYNOLDS NUMBER
- BUT WE CAN OBTAIN MODEL DATA WITH LAMINAR, TRANSITIONAL OR TURBULENT BOUNDARY-LAYER STATE
- VERY IMPORTANT TO KNOW BOUNDAY-LAYER STATE OF TEST
- TYPICALLY WE WANT LAMINAR OR TURBULENT NOT TRANSITIONAL
- BUT WIND TUNNEL Re_L IS TOO LOW TO PRODUCE A TURBULENT BOUNDARY LAYER

∴ MUST USE BOUNDARY-LAYER TRIPPING TECHNIQUES

Figure 10. An engineering approach to transition.

Laminar flow over a model can usually be obtained by running at the low end of the operating stagnation pressure range of the facility. On the other hand, in many wind tunnels operation at the high end of the operating envelope may not provide a Reynolds number high enough to produce turbulent

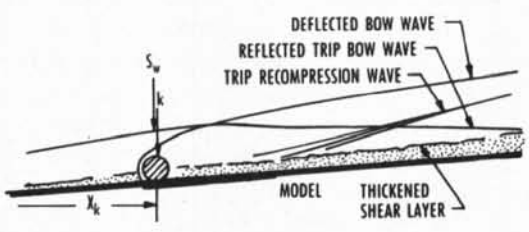

a. Oversized trip

Figure 11. Fundamentals of trip sizing.

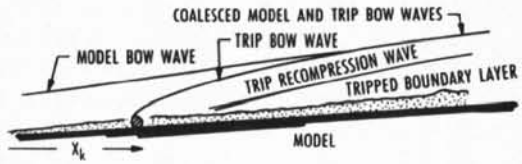

b. Correctly sized trip

Figure 11. Concluded.

flow over a model. In this case artificial tripping of the boundary layer is required. The fundamental principles of boundary-layer tripping are illustrated in Fig. 11. Experience (e.g.,Refs. 30 and 31) has shown that a spherical trip with a height on the order of the boundary-layer thickness, δ will produce a turbulent boundary layer, yet will not cause excessive downstream flow disturbances. A phase-change paint photograph of the turbulent flow produced on the nose of a shuttle model by a single trip sphere is shown in Fig. 12a.

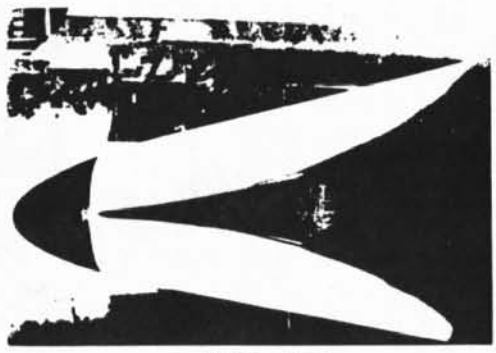

a. Single sphere

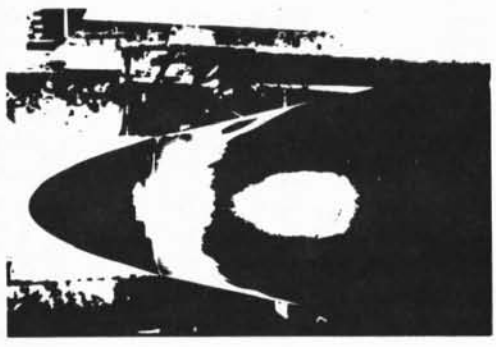

b. Multiple spheres, single row

Figure 12. Illustration of boundary layer trip effectiveness on nose of an orbitor model.

Fig. 12b is a similar photograph, but with a single row of trips spaced about three diameters apart. In general, three rows of staggered trip spheres, as illustrated in Fig. 13, is the most desirable trip configuration. Note that the spheres are welded on to a thin

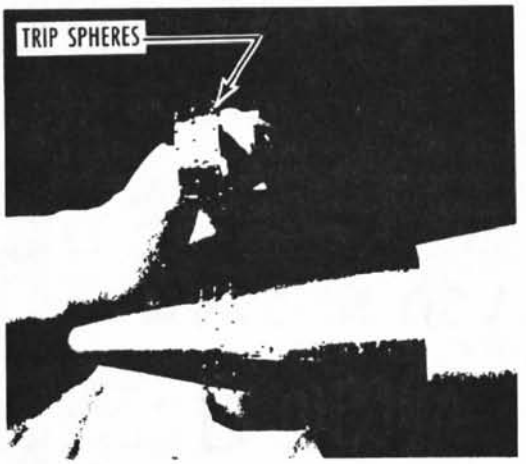

Figure 13. Photograph of trip ring with three rows of staggered spheres.

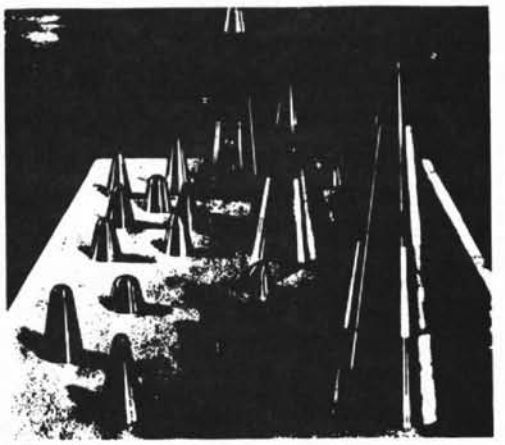

Figure 14. Photograph of numerous noses requiring trip rings for typical force test.

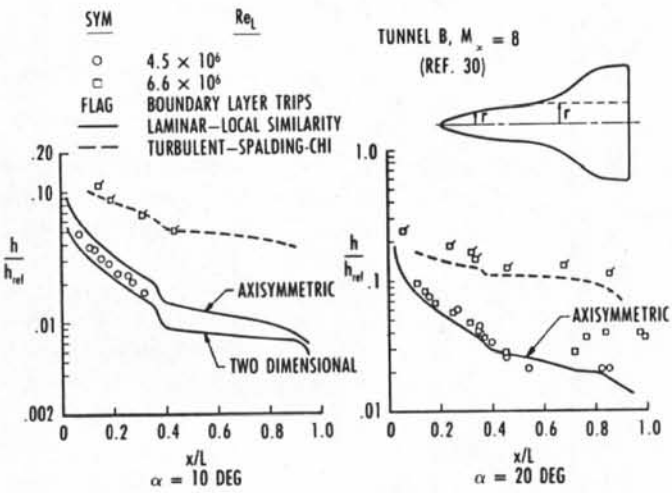

Figure 15. Illustration of boundary layer trip application.

detachable ring which is easy to install and remove from a large number of similar configurations (see Fig. 14). A common procedure is to select a trip sphere size (diam) and to build three detachable rings, one with the nominal trip diameter and the other two with a smaller and larger size, respectively.

Typical data illustrating the use of boundary-layer trips on a space shuttle model are shown in Fig. 15. Note that the flagged symbols correspond to the "tripped data" and, in general, agree with the turbulent boundary layer predictions. The unflagged high Reynolds number data at α = 20 deg are representative of a transitional boundary layer while the tripped data moved transition all the way to the model nose.

Just as predicting flight transition is a complex art, so is the proper sizing of boundary-layer trips. Figure 16 is an outline of a computer code used to size trips.

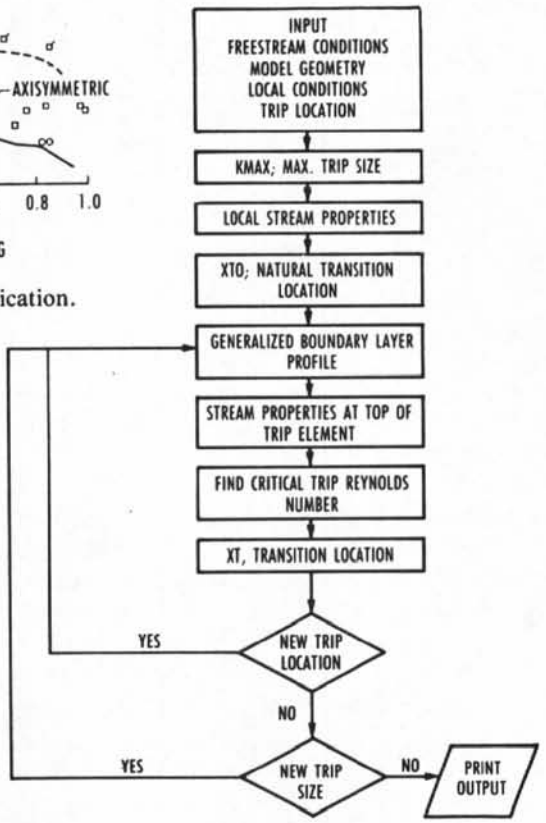

Figure 16. Trip sizing computer code.

SUMMARY

The primary conclusions of this section are:

- Boundary-layer transition prediction for flight has been studied by specialists for many years but it remains elusive
- Boundary-layer transition observed in wind tunnels is often upstream of that observed in flight because of "noise" in the tunnel
- Boundary-layer trips have been used for many years to produce turbulent flow in wind tunnel testing (three rows of staggered spheres most effective)

REFERENCES

1. Morkovin, M. V., "On Transition Experiments at Moderate Supersonic Speeds." *Journal of the Aeronautical Sciences*, Vol. 24, No. 7, July 1957, pp. 480-486.

2. Morkovin, M. V. "On Supersonic Wind Tunnels with Low Free-Stream Disturbances." *Journal of Applied Mechanics*, Tran. ASME, Vol. 26, Series E, June 1959, pp. 319-324.

3. Morkovin, M. V. "Critical Evaluation of Transition From Laminar to Turbulent Shear Layers with Emphasis on Hypersonically Traveling Bodies." AFFDL TR-68-149, March 1969.

4. Morkovin, M. V., AIAA Lecture Series on Boundary Layer Transition, 1984.

5. Stetson, K. F. and Kimmel, R. L. "On Hypersonic Boundary-Layer Stability," AIAA Paper No. 92-0737, January 1992.

6. Stetson, K. F., Thompson, E. R., Donaldson, J. C., and Siler, L. G. "Laminar Boundary Layer Stability Experiments on a Cone at Mach 8, Part 1: Sharp Cone." AIAA Paper No. 83-1761, July 1983.

7. Stetson, K. F., Thompson, E. R., Donaldson, J. C., and Siler, L. G. "Laminar Boundary Layer Stability Experiments on a Cone at Mach 8, Part 2: Blunt Cone." AIAA Paper No. 84-0006, January 1984.

8. Stetson, K. F., Thompson, E. R., Donaldson, J. C., and Siler, L. G. "Laminar Boundary Layer Stability Experiments on a Cone at Mach 8, Part 3: Sharp Cone at Angle of Attack." AIAA Paper No. 85-0492, January 1985.

9. Stetson, K. F., Thompson, E. R., Donaldson, J. C., and Siler, L. G. "Laminar Boundary Layer Stability Experiments on a Cone at Mach 8, Part 4: On Unit Reynolds Number and Environmental Effects." AIAA Paper No. 86-1087, May 1986.

10. Stetson, K. F., Thompson, E. R., Donaldson, J. C., and Siler, L. G. "On Hypersonic Transition Testing and Prediction." AIAA Paper No. 88-2007, May 1988.

11. Stetson, K. F. "Nosetip Bluntness Effects on Cone Frustum Boundary Layer Transition in Hypersonic Flow." AIAA Paper No. 83-1763, July 1983.

12. Stetson, K. F. "On Nonlinear Aspects of Hypersonic Boundary-Layer Stability." AIAA Journal, Vol. 26, No. 7, pp. 883-885, July 1988.

13. Stetson, K. F. "Boundary Layer Transition on Blunt Bodies with Highly Cooled Boundary Layers." J. A. S., Vol. 27, pp. 81-91, February 1960. (Also, IAS Report No. 59-36, January 1959).

14. Stetson, K. F. "Mach 6 Experiments of Transition on a Cone at Angle of Attack." Journal of Spacecraft and Rockets, Vol. 19, No. 5, pp. 397-403, Sept-Oct 1982.

15. Reshotko, Eli. "Stability and Transition, How Much Do We Know?" Paper presented at Tenth U. S. National Congress of Applied Mechanics, The University of Texas at Austin, Austin, Texas, June 1986.

16. Kovasznay, Leslie, S. G. "Turbulence in Supersonic Flow." *Journal of the Aeronautical Sciences*, Vol. 20, No. 10, October 1953, pp. 657-674.

17. Pate, S. M. "Effects of Wind Tunnel Disturbances on Boundary-Layer Transition with Emphasis on Radiated Noise: A Review." AIAA Paper No. 80-0431, March 1980.

18. Goodrich, W. D., Derry, S. M., and Bertin, J. J. "Shuttle Orbiter Boundary-Layer Transition: A Comparison of Flight and Wind Tunnel Data." AIAA Paper No. 83-0485, January 1983.

19. Stetson, K. F. "Hypersonic Boundary-Layer Transition." The Second Joint Europe/US Short Course in Hypersonics, GAMNI-SMAI, January 1989.

20. Beckwith, I. E. "Development of a High Reynolds Number Quiet Tunnel for Transition Research." AIAA Journal, Vol. 13, No. 3, pp. 300-306, March 1975.

21. Chen, F.-J., Malik, M. R., and Beckwith, I. E. "Comparison of Boundary Layer Transition on a Cone and Flat Plate at Mach 3.5." AIAA Paper No. 88-0411, January 1988.

22. Pate, S. R. "Dominance of Radiated Aerodynamic Noise on Boundary Layer Transition in Supersonic-Hypersonic Wind Tunnels, Theory and Application." AEDC-TR-77-107 (AD-A052-621), March 1978.

23. Neumann, R. D., and Patterson, J. L. "Results of an Industry Representative Study of Code to Code Validation of Axisymmetric Configurations at Hypervelocity Flight Conditions." AIAA Paper No. 88-2691, June 1988.

24. Batt, R. G., and Legner, H. H. "A Review of Roughness Induced Nosetip Transition." AIAA Paper No. 81-1223, June 1981.

25. Pate, S. R. and Adams, J. C. "Hypersonic Simulation for Lifting Body Transition Studies." Proceedings of the Boundary Layer Transition Workshop, November 1971, Aerospace Report No. TOR-0172(S2816-16)-5, December 1971.

26. Matthews, R. K. "An Experimental Investigation of the Effects of Geometry and Attitude on the Windward Heating of Conical Models at Mach 8." AEDC-TR-73-69 (AD-909-655L), April 1973.

27. Creel, T. R., Jr., Beckwith, I. E., and Chen, F. J. "Transition on Swept Leading Edges at Mach 3.5." Journal Aircraft, Vol. 24, No. 10, December 1987.

28. Chen, F. J., Malik, M. R., and Beckwith, I. E. "Instabilities and Transition in the Wall Boundary Layers of Low Disturbance Supersonic Nozzles." AIAA Paper No. 85-1573, 1985.

29. Beckwith, I. E., Chen, F. J., and Malik, M. R., "Design and Fabrication Requirements for Low-Noise Supersonic/Hypersonic Wind Tunnels." AIAA Paper No. 88-0143, January 1988.

30. Matthews, R. K., Buchanan,.T. D., Martindale, W. R., ARO, Inc. and Warmbrod, J. D. MSFC. "Experimental and Theoretical Aerodynamic Heating and Flow Field Analysis of a Space Shuttle Orbiter." NASA TM X-2508, February 1972.

31. Ievalts, J. O., and Matthews, R. K. "Aerothermal Evaluation of High Temperature Structural Materials for Use in High-Performance Missile Design." AEDC-TR-79-38 (AD-A080-023), January 1980.

ELECTROMAGNETIC WAVE TEST

by
R. K. MATTHEWS
Senior Staff Engineer

and

S. A. Stepanek
Principal Engineer
Calspan Corporation/AEDC Operations
Arnold Engineering Development Center

ABSTRACT

Electromagnetic wave testing represents a relatively new test technique that involves the union of several disciplines: aerothermodynamics, electromagnetics, materials/structures, and advanced diagnostics. The essence of this new technique deals with the transmission and possible distortion of electromagnetic waves (RF or IR) as they pass through the bow shock, flow field, and electromagnetic (EM) window of a missile flying at hypersonic speeds. Variations in gas density along the optical path can cause significant distortion of the electromagnetic waves and, therefore the missile seeker system may not effectively track the target. Two specific test techniques are described. The first example deals with the combining of a wind tunnel and an RF range while the second example discusses the complexities of evaluating IR seeker system performance.

INTRODUCTION

Tactical missiles currently being designed or developed will fly much faster than existing systems. The radomes on these missiles will experience high aerodynamic heating during flight resulting in elevated radome temperatures which, in turn produce changes in the dielectric properties of the radome and contribute to changes in boresight error (BSE) (illustrated in Fig. 1). BSE is a function of the radome material, thickness, temperature, and receiver operating frequency. Therefore, characterization of radome EM transmission performance in terms of boresight error over the range of possible seeker-antenna gimbal angles is essential in the development of a radome.

Because of the complex manner in which the various radome and seeker-system design parameters interact, it is very difficult to use predictive methods to evaluate the boresight error characteristics of a system. For that reason, radome electrical performance is determined experimentally. Until recently, standard experimental methods provided measurements only for radomes at ambient temperature. As missile velocities increase causing aeroheating to be important, it is increasingly important that BSE measurements be made on radomes under realistic flight conditions, especially in terms of radome temperature levels and distributions. In one such effort, Weckesser et al.,[1] investigated the effect of temperature on BSE for several ceramic radomes using a solar furnace as a radiant heat source for the radomes. Other investigators have used various nonaerodynamic heat sources, including electric blankets and radiation lamps. One of the drawbacks with these methods is that the aerothermodynamic environment is not closely simulated so that, although elevated radome temperatures are achieved, correct distributions and levels are not. In addition, the lack of simulation of flight pressures and aerodynamic shear, which contribute to the ablation/recession process, makes these techniques even less desirable for evaluating ablative type radomes.

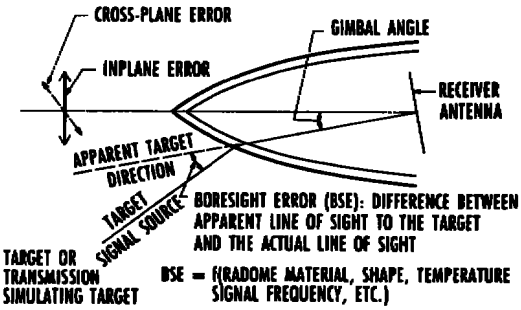

Figure 1. Radome cross-section sketch showing boresight error.

RF TEST TECHNIQUE

The AEDC, working jointly with General Dynamics/Electronics (GD/E), has developed a unique test technique which permits boresight error mea-

surements to be made on radomes exposed to conditions closely approximating flight. The technique was developed by using the Aerothermal Wind Tunnel (C) in combination with a radar range facility designed specifically for this purpose. This concept takes advantage of existing wind tunnel capabilities and data systems and provides extensive coverage of the radome temperature and surface recession.

The test program as described below provided an example of the application of the boresight error test technique which consisted of two distinct test phases.

Phase I: Experimental Determination of the Radome Thermal Response to the Wind Tunnel Environment.

Phase II: Validation of the Radome Range and Boresight Error Measurements on Aerodynamically Heated Radomes.

The Aerothermal Wind Tunnel (C) used for these tests is a continuous flow, 0.64 m (25-in.)-diam variable density, Mach 4 free-jet wind tunnel. This unique tunnel (Fig. 2a) was developed specifically for materials testing and provides "clean" aerodynamic flow at temperatures, pressures, and shear loads similar to those experienced in actual flight. "Clean" refers to both the repeatable quality and uniformity of the flow as well as the fact that air is used as the test gas, and only clean air constituents are present (i.e., no water vapor, dirt, dust or products of combustion). The tunnel is equipped with a model injection system which translates the test article "into" and "out of" the flow field in a few seconds. However, since the airflow is continuous, the test article can remain in the flow for a time period required for the measurement (e.g., 10 to 140 sec during the current test). A complete description of Tunnel C can be found in Ref. 2.

In order to provide a facility with a boresight error measurement capability, a radar range was installed directly below the tunnel nozzle as shown in Fig. 2b. The range consisted of an existing cylindrical pressure vessel which was matched to the installation tank door opening of the wind tunnel. A photograph of the inside of the range, taken from the transmitter looking towards the radome and receiver, is shown in Fig. 3.

External surface temperatures of the radome were monitored with an infrared data system.[3] With this

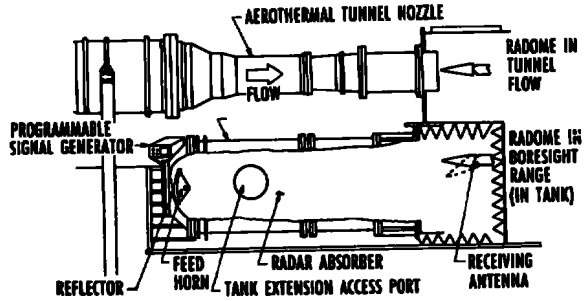

a. Facility sketch

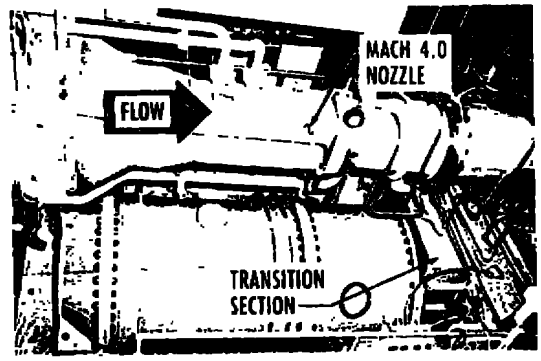

b. Tunnel after BSE test modification

Figure 2. Radome range/aeroheating facility at AEDC.

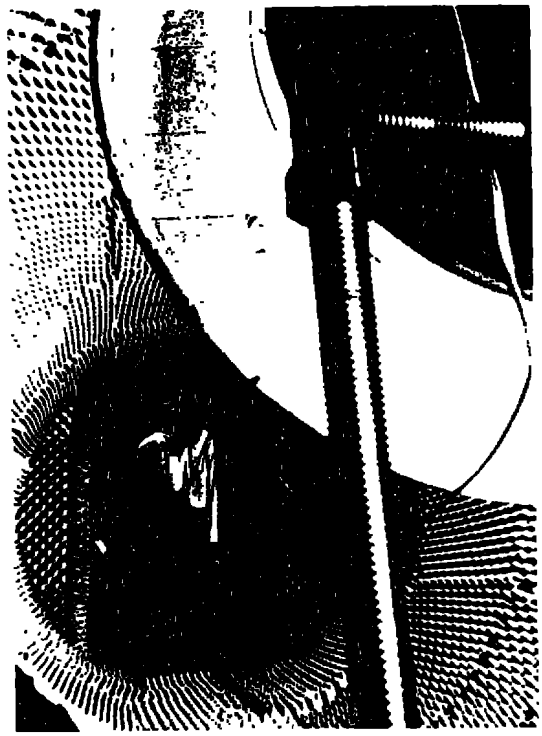

Figure 3. View of AEDC boresight error range looking toward radome from transmitter location.

system, the surface temperature of the entire radome was mapped at various times during wind tunnel exposure and during the BSE measurement process. Figure 4 shows a sample surface temperature map produced from the IR system output. Surface temperatures determined from IR measurements were also plotted with interface and backwall thermocouple data as shown in Fig. 4c to aid in determining radome wall temperature gradients.

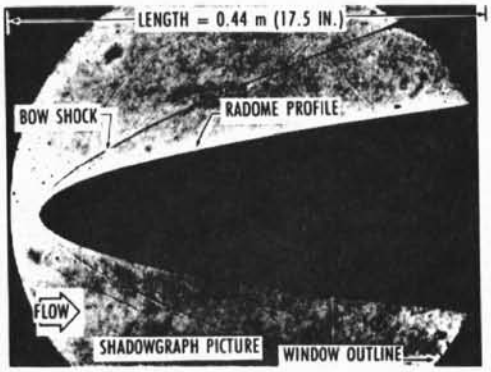

a. Shadowgraph flow field

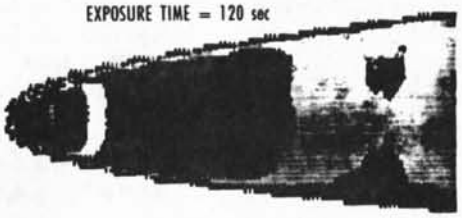

b. IR system mapping of surface temperature response (top view)

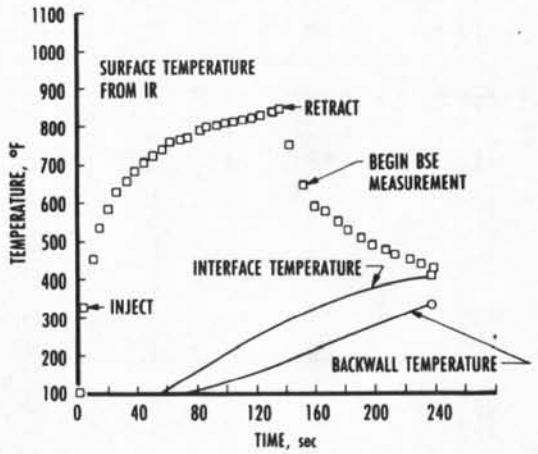

c. IR and thermocouple temperature history.

Figure 4. Sample data obtained from thermal phase.

In Fig. 5, results obtained for one of the radomes tested during the BSE phase are shown to examine the difference between BSE data for the ambient (before injection into tunnel flow) and elevated (first sweep after retraction from tunnel flow) radome temperatures. Notice that the peak values of BSE are different for the ambient and heated data and that the gimbal angle at which the peak occurs is also different. Therefore, these data indicate that the elevated temperature and/or recession which occurs during exposure to the tunnel flow produced significant changes in the BSE characteristics of this radome.

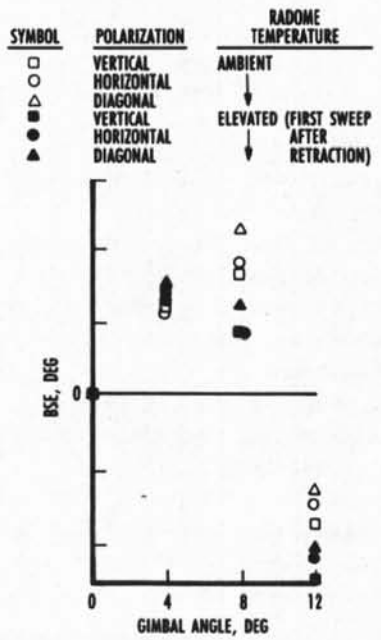

Figure 5. Comparision of ambient and heated radome boresight error data.

AERO-OPTICS TEST TECHNIQUE

Understanding the interaction between optical waves and aerodynamic flow fields is also critical in the development of optical guidance and tracking systems. Accurately discerning the location of radiating targets is difficult from images that are blurred, jittered, and attenuated by an unsteady aerodynamic flow field. Refraction of optical waves propagating through shock waves and density gradients must be known for in-flight compensation. The distortion of target radiation due to hypersonic aerodynamics for a cooled-window flight scenario is depicted in Fig. 6. Fluctuating effects due to turbulence, shock/boundary layer interactions, flow separations, mixing/shear layer flows, etc. must also be evaluated.

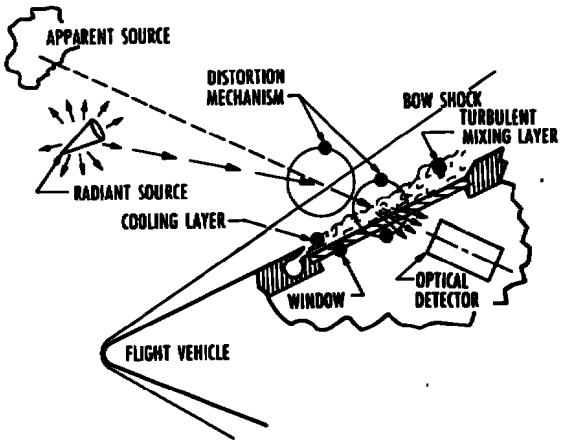

Figure 6. Aero-optical distortion scenario.

Additionally, flight system effects, such as mechanical vibrations and thermal-mechanical window stress, can render guidance and tracking sensors useless. Lensing effects from stress-induced window distortions (exacerbated by aerodynamic heating and pressure loads), and radiation from heated windows and hot external gases can preclude target discrimination. Realistic issues such as these complicate the specification, design and testing of optical systems.

In evaluating aero-optic effects, designers struggle with theoretical predictions and experimental methodologies because both are unvalidated and currently unreliable. Furthermore, existing ground test facilities only simulate parts of the severe conditions encountered in high-speed flight. Therefore, the approach required for modern aero-optic investigations is one where code-validation experiments must be carefully performed in available test facilities, and then validated codes must be used to predict the aero-optic effects at flight conditions. As shown in Fig. 7, the application of aero-optics technology includes validating complex CFD and optical wave propagation models using both aerodynamic and optical measurements from carefully designed code validation experiments. This approach is particularly difficult given the current state-of-the-art of turbulence models and flow diagnostics where few validated techniques exist.

The basic approach developed to obtain experimental optical measurements in a large-scale ground test facility at AEDC is illustrated in Fig. 8. The objective of this technique is to isolate and characterize the flow-induced (aero-optic) distortion. An IR beam (representing the target radiation) originating outside the tunnel is introduced through a flat plate and directed toward the test article. After passing through the test article flow, the then-distorted beam is directed out of the tunnel to the receiving optics. The primary test requirement is to provide an undistorted beam to the test article, such that as the beam passes through the local test article flow, thus the only

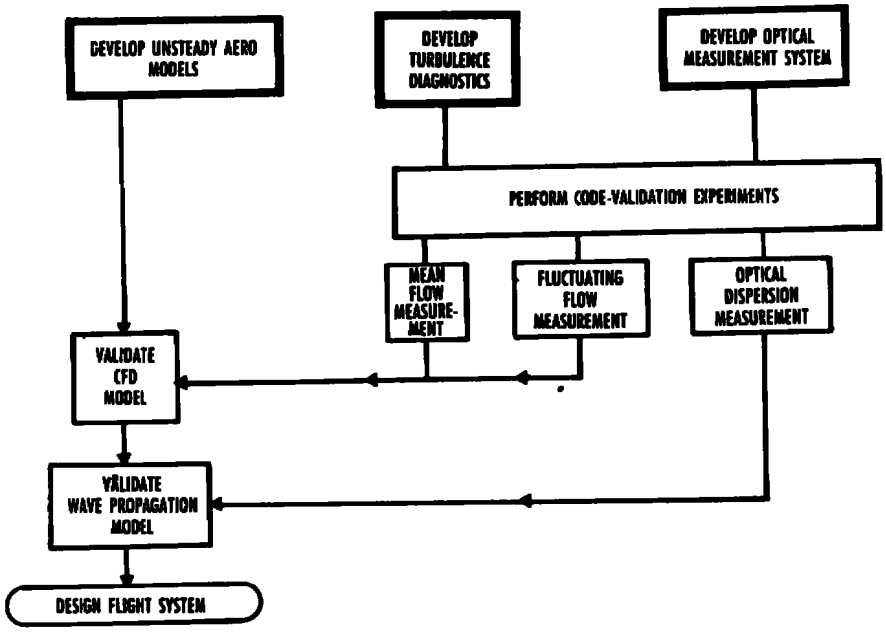

Figure 7. Applying aero-optics methodology to flight system design.

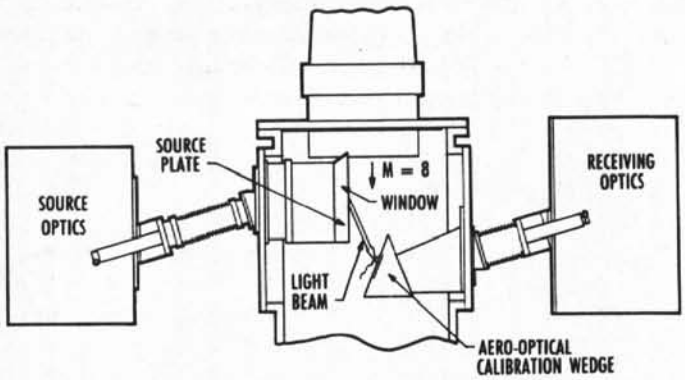

Figure 8. AEDC aero-optics measurement system basic scheme.

optical distortion measured is caused by the test article flow. Only in this manner can the optical distorton be directly related to the flow for code validation.

Careful attention must be placed on minimizing the effects of facility vibration on the optical measurements by using isolation damped optical tables and an evacuated, rubber-bellows-mounted beam path.

An overhead view of the physical installation of the aero-optical measurement system is shown in Fig. 9. AEDC's system is a fully integrated optical measurement system providing imaging, image jitter, and holographic measurements. Diffraction-limited performance of the beam delivery system required the use of highest-quality optics. Custom built electronics controlled and varied the duration of the beam pulse so that the effects of camera-integration time could be determined.

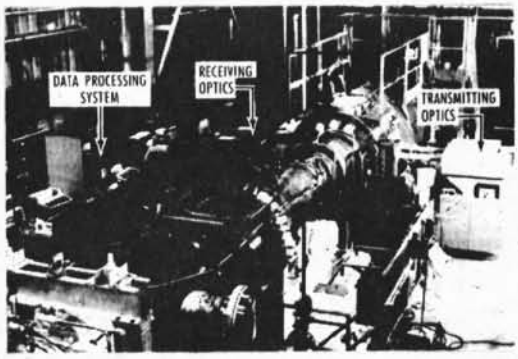

Figure 9. Aero-optics equipment installed for test in AEDC tunnel C, M = 8.

Figure 10 shows the physical installation inside the wind tunnel, looking downstream. Optical distortion measured in this technique-validation configuration represents the combined facility effects (including a second flat plate and optical system imperfections) and serves as an end to-end evaluation of the ability of the facility to successfully provide an undistorted beam for fundamental aero-optics measurements.

The beam passes through the local flat plate boundary layer and bow shock. The plate is pitched windward slightly to ensure a well established but weak attached shock. Flat plate surface pressure and heat transfer measurements are required to ensure that the flow over the source window is not disturbed by leading edge effects or wraparound flow from under the plate. Heat transfer measurements are also used to locate boundary layer transition, which ideally should occur well downstream of the window to allow passing the beam through a benign laminar boundary layer.

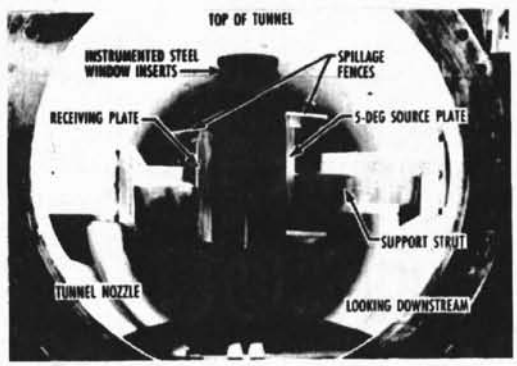

Figure 10. View looking downstream at aero-optic wedges and supporting equipment.

The types of optical test measurements are depicted in Fig. 11. Image spot data, used primarily to quantify geometric degradation of the optical waves, are obtainable from intensity measurements of a focused image spot. From imaging measurements, four parameters are commonly determined: boresight error, image blur, image jitter and Strehl ratio. (These same parameters are determined theoretically by passing a plane wave, representing the target radiation, through the calculated aerodynamic field.) Boresight error refers to the difference between the position inferred from the detected image and the

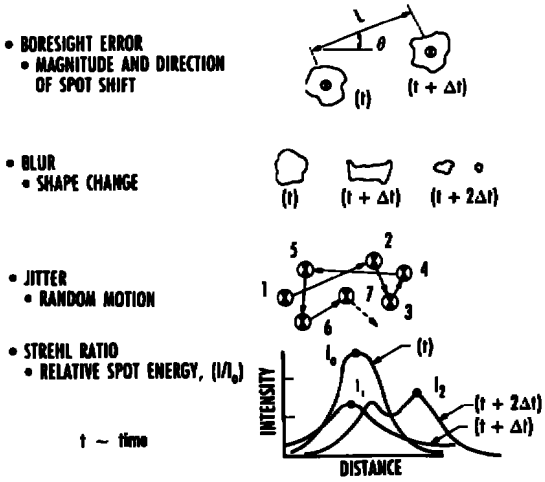

Figure 11. Aero-optical image-spot characteristics.

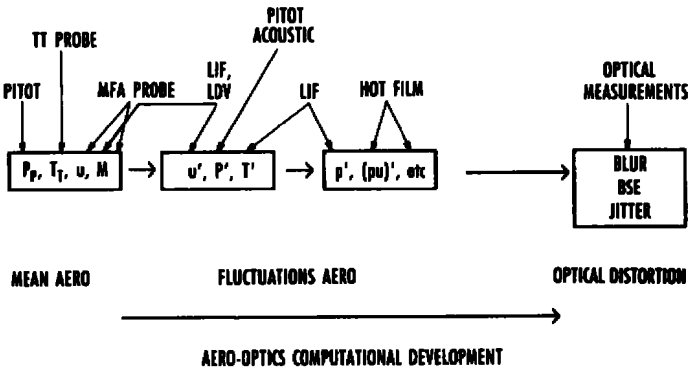

Figure 12. Use of aero measurement techniques for code validation.

actual beam (target) location. Image blur is the spreading of an imaged spot relative to its original shape, which results from variations in the refractive media, and its effect is seen as a degradation in image clarity. Image jitter is the random unsteady motion of the image about a reference point, which results in the appearance of the image to flicker or blur, depending on the frequency of the randomness and the sampling of the detection system. The Strehl ratio refers to the diminished total energy of the beam after it passes through the aerodynamic field.

The validation of aero-optic prediction codes requires experimental measurement of both the aerodynamic flow field and the resulting optical distortion. Optical measurements alone are not sufficient to validate the fundamental aspects of the code that relate the optical wave distortion to the aerodynamic flow. Given the complexity of the aerodynamic environment, as many theoretical steps in the code as possible should be independently validated experimentally: from the calculation of local mean flow conditions, and the application of assumed turbulence models to define the fluctuating flow properties, to the calculations of the optical beam distortion. An example of the utility of numerous and complimentary measurement techniques to verify various theoretical calculation steps is depicted in Fig. 12.

The use of advanced, non-intrusive flow diagnostic techniques is considered an enabling and necessary feature of aero-optic testing in that experimental characterization of the key fluctuating state properties (e. g., density) is the critical link between the aerodynamics and the optical effects. The promise of advanced techniques to provide simultaneous measurement of more than one flow property may be invaluable to successful modeling of turbulent mixing of dissimilar, reacting gases.

To illustrate window/frame-induced distortion experiments in ground test facilities, Fig. 13 includes some imaging results from AEDC's Tunnel C facility validation test. On the left side, without installation of the windows in the flat plate test articles, the imaging data show a diffraction-limited spot, illustrating the successful development of a near-perfect optical beam delivery system. However, when the windows were installed, serious degradation of the beam resulted (center image). This was determined to be caused by mounting stresses in the window frame assembly. Finally, with the wind tunnel on and the windows at nearly 900°F, the resulting image shows a different pattern of distortion. Unforeseen difficulties are common in performing aero-optic tests, and later modifications to the window frame were designed and validated in lab experiments.

SUMMARY

In summary, performing aero-optic investigations is a relatively new technology in applied aerodynamics, and from the experiences at AEDC, several key observations can be made.

1. In performing code validation experiments, both aerodynamic and optical measurements are required — and most important is the characterization of the turbulence, since the weakest part of existing codes is the turbulence model.

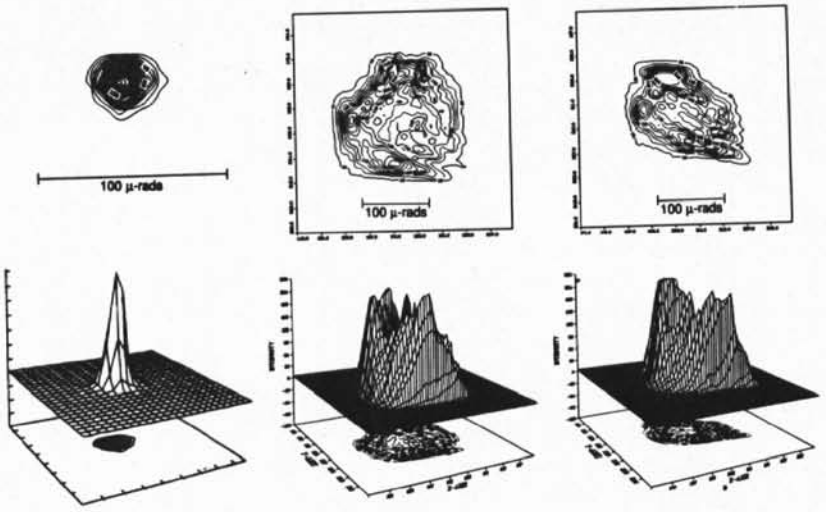

a. No windows

b. Windows, no flow (mechanical stress)

c. Windows and flow (thermal and mechanical stress)

Figure 13. Image spots showing window-stress effects.

2. Meticulous attention must be given to the facility-induced error sources, which can invalidate measurements made with even the most perfect optics

3. Any system designed and constructed must be painstakingly tested and validated prior to its use. The analysis of measurement uncertainty of aero-optic testing is an essentially-untouched frontier.

4. Investigating fundamental wave-flow interactions requires a diversity of interrelated disciplines, including aerodynamics, electro-optics, spectroscopic physics, material/structures, ground testing and CFD.

5. Planning and preparing for aero-optics testing requires careful consideration of test simulation issues, measurement requirements, facility and instrumentation error sources, etc.

6. Additional information regarding Aero-Optics Wave Testing can be found in References 4 through 6.

REFERENCES

1. Weckesser, L. B. et al. "Radome Aerodynamic Heating Effects on Boresight Error." Proceedings of the Fifteenth Symposium on Electromagnetic Windows, Georgia Institute of Technology, June 18-20, 1980.

2. Strike, W. T. "Calibration and Performance of the AEDC/VKF Tunnel C, Mach Number 4, Aerothermal Wind Tunnel." AEDC-TR-82-6 (AD-A116279), June 1982.

3. Boylan, D. W., Carver, D. B., Stallings, D. W., and Trimmer, L. L. "Measurement and Mapping of Aerodynamic Heating Using a Remote Infrared Scanning Camera in Continuous Wind Tunnels." AIAA Paper No. 78-779, April 1978.

4. Crosswy, F. L. and Havener, A. G. "Aero-Optics Measurement System for the AEDC Aero-optics Test Facility." AEDC-TR-90-20, Arnold Engineering Development Center, February 1991.

5. Havener, A. G. and Stepanek, S. A. "Aero-optics Testing Capabilities & AEDC." AIAA Paper 92-0760, 30th Aerospace Science Meeting, Reno, NV, January 6-9, 1992.

6. Dixon, P. W., "Image Degradation Caused by Thermal Gradients in Windows." AIAA Paper 92-075, 30th Aerospace Science Meeting, Reno, NV, January 6-9, 1992.